CIRCADIAN RHYTHM OF INTRAOCULAR PRESSURE AND OPTICAL COHERENCE TOMOGRAPHY IMAGING IN THE RAT EYE

By

Diana C. Lozano, B.S.

DISSERTATION

In partial satisfaction of the requirements for the degree of

DOCTOR OF PHILOSOPHY

in

PHYSIOLOGICAL OPTICS

Presented to the Graduate Faculty of the

College of Optometry
University of Houston

December 2014

Approved:

Michael Twa, O.D., Ph.D.

Laura Frishman, Ph.D.

Jason Porter, Ph.D.

Andrew Hartwick, O.D., Ph.D.

Committee in Charge

Dedication

Para mi familia

Acknowledgements

This dissertation is a product of many years of hard work. I could not have finished this work without the love and support from my family. I would like to thank my parents, Jesus and Carmen Lozano, for their unwavering confidence in me and for the many sacrifices they made to provide a better life for my sibling and me. They taught me the meaning of hard work and the importance of getting an education. Muchas gracias por el apoyo; los quiero mucho. I am grateful to my brother, Jesus Jr., my sister, Monica, and my brother-in-law, Diego, for cheering me on when I needed it the most and for being outstanding role models. I am also grateful for the life of my beautiful niece, Marlenne; her smile lifts my spirit and she makes me want to be a better person.

I could not have finished this dissertation without the help and guidance of many outstanding and supportive mentors that have left an everlasting print in my academic and professional life. I first have to thank my advisor, Dr. Michael D. Twa, for his endless words of encouragement, his support, patience, and collegiality. I am grateful for the freedom he gave me to explore and acquire many skills that will be invaluable in my career. I am extremely grateful for the many insightful discussions we had and for the time and attention he dedicated to me in and out of the laboratory setting. He has truly fulfilled the role of a mentor and I hope that some of his passion for science and teaching has rubbed off on me to make me a better scientist.

I would also like to thank my dissertation committee for their invaluable input and insightful discussions throughout my PhD training. I want to thank Dr. Laura J. Frishman for her patience in teaching retinal physiology, for her guidance and for everything she does for the graduate program. She works tirelessly to ensure that all graduate students have a place to learn. Next, I want to thank Dr. Jason Porter for sharing his passion for optics and vision science with me. I met Jason eleven years ago when I participated in a

summer undergraduate research program at the University of Rochester. I am indebted to him for the many research skills I learned that summer and want to thank him for being a constant source of encouragement all these years. I want to thank Dr. Andrew Hartwick for the time he dedicated to answering my questions about circadian rhythms and for his genuine interest in my research. I am indebted to all my committee members for their guidance and for everything they taught me over the years.

I am also grateful to the faculty, staff, and fellow graduate students from the University Of Houston College Of Optometry, including, Dr. Don Fox, Dr. Alan Burns, Dr. Shawntay Gibson, Elda Rueda, Evelyn Brown and Margaret Gondo for their willingness to teach me various histological methodologies. I would also like to thank my fellow lab mate (Srilatha) and summer research students (Nicolas Rodriguez, Jessica Lee, Haris Vakil, Betty Zhang, and Kevin Soon) for their help with my work. Michele Stafford and Diana Davis helped me with various topics like class enrollment. I would like to thank Kevin Ivers, Joseph Manarang, Elda Rueda, Aurora I. Ramos, and Judith Nuñez Romero for their kind friendship.

Lastly, I want to thank the many undergraduate mentors that helped me fulfill my goal of obtaining my PhD. I am grateful to Michelle Lopez and Thelma Chavez for their encouragement to pursue various summer research programs and for accepting me into the Minority Biomedical Research Support program that sponsored several years' worth of research during my undergraduate training. I am especially thankful to Dr. David R. Williams, Dr. Brian Barsky, Dr. Steven Schallhorn, and Dr. Corina Van de Pol for introducing me to vision science research and for the many research skills they taught me while working in their labs.

The work presented in this dissertation was supported by: NIH P30 EY007551, University of Houston College of Optometry Student Vision Research Support Grants, and Fight for Sight Summer Student Fellowship.

CIRCADIAN RHYTHM OF INTRAOCULAR PRESSURE AND OPTICAL COHERENCE TOMOGRAPHY IMAGING IN THE RAT EYE

By

Diana C. Lozano, B.S.

An Abstract of a Dissertation

Presented to the

Faculty of the College of Optometry

University of Houston

In Partial Satisfaction of the Requirements for the Degree of

Doctor of Philosophy

in

Physiological Optics

December 2014

Abstract

Purpose: Ocular hypertension is a risk factor for developing glaucoma, which is an optic neuropathy characterized by progressive degeneration of retinal ganglion cells and subsequent irreversible vision loss. The goal of this dissertation was to address several challenges needed to interpret the relationship between pressure and *in vivo* changes to retinal thickness and the optic nerve head in a rat model of glaucoma.

Methods: Pressure dynamics were evaluated in three experiments: **(1)** First, the reliability of two TonoLab rebound tonometers was measured in 18 Brown Norway Rats. **(2)** The calibrated tonometers were then used to measure the circadian rhythm of intraocular pressure (IOP) in standard light-dark conditions (LD) and in continuous dim light (LL). Specifically, the existence of an IOP rhythm in LL was investigated and whether the IOP rhythm was centrally driven by the suprachiasmatic nucleus. **(3)** The circadian rhythm of IOP and mean arterial pressure (MAP) were measured in 8 adult Brown Norway rats housed in LD. Structural assessment of disease in a rat model of glaucoma was evaluated in three experiments **(4)** First, the ability to scan the same retinal location with a clinical spectral domain optical coherence tomography (SD-OCT) system was evaluated by acquiring retinal images from 16 rats. **(5)** A schematic model eye was developed to compensate for lateral magnification in SD-OCT images of the normal rat eye. Mean total retinal thickness was measured 500 µm away from the optic nerve head (ONH) and ONH diameter was measured from SD-OCT images. These images were scaled using the schematic model eye and the SD-OCT system's *Built-in* scaling. **(6)** IOP was surgically elevated by injecting hypertonic saline into an episcleral vein of the rat eye. Circumpapillary scans were computationally generated to calculate global (mean of circumpapillary scan) and regional (superior, inferior, nasal, and

temporal) mean nerve fiber layer/retinal ganglion cell layer (NFL/RGLC), NFL/RGCL plus inner plexiform layer (NFL/RGCL+IPL), and total retinal thicknesses.

Results: (1) The 95% limits of agreement (95% LoA) were smaller and better for *TonoLab #1* (± 4 mm Hg) than for *TonoLab #2* (± 6 mm Hg). **(2)** IOP in the LD conditions was lowest during the light-phase (16 ± 2 mm Hg), highest during the dark-phase (30 ± 7 mm Hg), and peaked near the middle of the dark phase (16.6 ± 1.2 Zeitgeber Time). The maximum range of IOP measurements was 14 ± 3 mm Hg under LD, and this maximum range dampened to 8 ± 1 mm Hg after 1 week, 8 ± 2 mm Hg after 4 weeks and 6 ± 1 mm Hg after 7 weeks of exposure to LL. **(3)** MAP during the light phase was 101 ± 3 mm Hg and 94 ± 3 mm Hg during the dark phase. IOP peaked 4.6 hours after the lights turned off and MAP peaked 4 hours before the lights turned off. **(4)** Thickness differences between imaging sessions for NFL/RGCL was 1 µm (95% LoA: –4 to 3 µm; ICC=0.82; CV=4.7%), for NFL/RGCL+IPL was 0 µm (95% LoA: –4 to 4 µm; ICC=0.88; CV=1.4%), and for total retinal thickness was 1 µm (95% LoA: –3 to 4 µm; ICC=0.97; CV=0.7%). **(5)** Mean total retinal thickness increased by 21 µm and the standard deviation doubled when images were scaled with the *Built-in* scaling (222 ± 13µm) compared to scaling images with individual biometric parameters (201 ± 6 µm). ONH diameter was three times larger when images were scaled with the *Built-in* scaling (925 ± 97 µm) than the individual biometric parameters (300 ± 27 µm). **(6)** In normal rats, mean temporal NFL/RGCL thickness (39 ± 6 µm) was significantly thicker than inferior (33 ± 5 µm) and superior (31 ± 5 µm) NFL/RGCL thickness. NFL/RGCL thickness in the nasal quadrant (36 ± 8 µm) was not significantly different from all other quadrants. In the rat model of glaucoma, IOP after 5 to 10 weeks after disease induction was significantly higher (95% CI: 21 – 43 mm Hg) than before disease induction IOP measurements (95% CI: 17 – 20 mm Hg; P = .02). Mean global NFL/RGCL+IPL thickness significantly

decreased from 83 ± 11 µm to 73 ± 15 µm (*P* = .003) and mean global total retinal thickness decreased from 201 ± 13 µm to 170 ± 31 µm (*P* = .001).

Conclusions: The persistent circadian rhythm of IOP in continuous dim light and the phase relationship between MAP and IOP may further contribute to morphological changes in the ONH and retinal thickness measurements in rats with experimental glaucoma. The *in vivo* retinal thickness changes measured in rats with experimental glaucoma correlated well with histological assessment of optic nerve damage (e.g., gliosis and collapsed myelin sheaths).

Table of Contents

List of Figures

Chapter Two

Chapter Three

Chapter Four

Chapter Five

Chapter Six

Chapter Seven

List of Tables

Chapter Two

Chapter Three

Chapter Four

Chapter Five

Chapter One

General Introduction

Glaucoma is the second leading cause of blindness worldwide. High intraocular pressure (IOP) is a risk factor for glaucoma and several studies have shown the benefit of lowering IOP in slowing the progression of glaucomatous optic neuropathy.[1-3] For example, the Ocular Hypertension Treatment Study showed that topical medications to lower elevated IOP reduced the incidence of glaucomatous visual field loss and damage to the optic nerve.[2] Mechanical and vascular theories have emerged to explain the pathophysiology of the disease.[4-8] The mechanical theory of glaucoma suggests that elevated IOP leads to deformation of the lamina cribrosa.[9] The lamina cribrosa is composed of layers of collagen, capillaries, and astrocytes through which retinal ganglion cell axons pass through as they exit the retina and enter the brain.[10, 11] High IOP imparts stress and strain at the optic nerve head that can in turn alter blood flow, disrupt both anterograde and retrograde axonal flow, and it can lead to retinal ganglion cell death. The vascular theory states that elevated IOP compromises the blood supply to the optic nerve leading to ischemia. It is likely that these theories are not independent, but, instead, that aspects from both theories lead to the pathogenesis of glaucoma. Specifically, since high IOP cannot explain the pathogenesis of glaucoma in all cases, it is likely that the interbalance between IOP, blood pressure, and intracranial pressure plays a significant role in the pathophysiology of the disease.

The first goal of this dissertation was to study the relationship between IOP and mean arterial pressure in Brown Norway rats. We specifically investigated if the circadian rhythm of IOP persisted when animals were housed in continuous dim light and the relationship between IOP and mean arterial pressure when animals were housed in standard light-dark conditions (12 hours of light / 12 hours of darkness). The results from these experiments show that the Brown Norway rat can be used as an experimental model to investigate the role of various compartmental pressures on the progression of structural and functional damage in experimental glaucoma.

Histological studies have shown that retinal ganglion cells with axons projecting to the superior and inferior retinal quadrants of the optic nerve head are primarily damaged in human glaucoma and experimental non-human primate models of glaucoma.[12] *In vivo* ocular imaging has advanced exponentially in the last decade to where it is now possible to non-invasively visualize various retinal layers and pore structures within the lamina cribrosa (the primary site of glaucomatous damage).[13] Spectral domain optical coherence tomography (SD-OCT) is one of the most widely used imaging techniques capable of resolving structures as small as 4 – 7 µm.[14, 15] Consequently, there is interest in using this high resolution *in vivo* imaging system to determine its usability for quantifying early and progressive changes in glaucoma. Knowledge about the early structural changes in glaucoma could improve clinical interventions and help preserve visual function.

The second specific aim of this dissertation was to use spectral domain optical coherence tomography (SD-OCT) to quantify spatial retinal structural changes in rats with experimental glaucoma. There are several challenges to consider when interpreting thickness measurements from SD-OCT images, including: scan placement/centration, axial length of the eye (i.e. correction of image lateral magnification), image quality, contribution of non-neuronal components (blood vessels and glial tissue), and instrument and examiner factors among others. As part of this dissertation, the experimental goals were to address the following challenges: (1) to quantify the effects of ocular–instrument realignment and image quality on measurements of retinal thickness from SD-OCT imaging in the rat eye; and (2) to develop a schematic model of the rat eye from *in vivo* axial biometric measurements to compensate for image lateral magnification. Addressing these challenges will enable in vivo quantification of the retinal and optic nerve head structural changes in a rat model of experimental glaucoma.

1.1 Glaucoma

Glaucoma is an optic neuropathy characterized by progressive degeneration of retinal ganglion cells that ultimately leads to irreversible vision loss. Well known risk factors include elevated IOP, age, race, and family history.[16-19] It was estimated that 60.5 million people worldwide had glaucoma in 2010, with the number expected to increase to 79.6 million by 2020.[20, 21] Vision loss in glaucoma results from dropout of retinal ganglion cells and their axons.

The events leading to the death of retinal ganglion cells is a topic of wide research. Much has been learned from animal models of glaucoma that mimic many of the features that occur in human glaucoma, such as thinning of the neural retinal rim tissue and remodeling of the optic nerve head.[22-28] One theory for the development of glaucoma is that high IOP imparts stress on the lamina cribrosa that activates the glia within the optic nerve head. Axons in the optic nerve head region are likely damaged when glia become activated, leading to a blockade of anterograde and retrograde axonal transport that eventually initiates a self-destruct program within the axons. There are two classical patterns of degeneration; one pattern is associated with fast anterograde degeneration of the axons and the second pattern is associated with slow retrograde degeneration of the axons. In retrograde degeneration, axonal damage generally begins at the synaptic end and progresses to the cell soma. While the exact pattern of degeneration in glaucoma has not been conclusively identified, there are studies in rodents and non-human primate models of glaucoma that support the idea that retinal ganglion cells undergo retrograde degeneration and that the lamina cribrosa is the initial site where retinal ganglion cell axons are damaged. For example, in a non-human primate model of glaucoma, the amount of visual function deficit did not correlate well with the number of ganglion cell somas lost when functional deficits were mild.[29] Furthermore, it has been reported that for glaucoma patients, about 40% of the retinal

nerve fiber layer, which is largely made up of the retinal ganglion cell axons, is lost before visual deficits can be reliably detected clinically by perimetry.[30] Consequently, objective methods of evaluating the integrity of the retinal nerve fiber layer are crucial for early identification of glaucoma.

As previously stated, the relationship between high IOP and structural damage to the optic nerve is supported by research in animal models of glaucoma that develop many of the characteristics of human glaucoma when they are exposed to high IOP for a long duration of time.[22-28] For example, elongated and larger pores in the lamina cribrosa were measured in a non-human primate model of experimental glaucoma using a high resolution *in vivo* imaging system (adaptive optics scanning laser ophthalmoscope).[31, 32] This structural remodeling within the optic nerve head is also associated with progressive loss of visual function, similar to what occurs in human glaucoma.[27, 33] While the mechanical and vascular theories are often thought of as being independent and competing theories to explain the pathogenesis of glaucoma, it is now becoming more evident that there is some relation between these theories. In particular, the interbalance between IOP, systemic blood pressure, and intracranial pressure is likely a contributing factor for glaucoma since high IOP alone cannot explain the pathogenesis of all types of glaucoma. Not only is blood flow within the optic nerve head important, but several studies have shown the detrimental effects of having high IOP and low systemic blood pressure.[34, 35] For example, functional vision was worse (e.g. dampened b-wave and dampened scotopic threshold response measured from electroretinograms) in rats with high IOP and low systemic mean arterial pressure than in rats with high IOP and high systemic mean arterial pressure.[34] Overall, clinical diagnosis of glaucoma is a difficult task because of the complex interaction between several risk factors that contribute to retinal ganglion cell damage and culminate in vision loss.

1.2 Clinical Measures of Glaucoma

Robust clinical methods are essential for the detection of early glaucomatous damage. A wide range of tests are performed in the clinic to determine the presence of glaucoma. For example, tonometry is routinely performed to measure IOP. However, a limitation with clinical measurements of IOP is that they are typically acquired once during the day and between clinic visits that are often months apart. These discrete measurements give only a partial view of the dynamic pressure load inside the eye that is insufficient to fully characterize pressure variations due to disease. Furthermore, it is important to have an accurate account of the pressure load inside the eye because it can have a direct impact on a patient's treatment plan. For example, surgical interventions may be indicated when pressure cannot be lowered with topical treatments. Therefore, reliable IOP measurements are essential to understand the pathophysiology of glaucoma. In this dissertation we evaluated the reliability of a rebound tonometer to acquire IOP measurements in the un-anesthetized rat. This was an important challenge to address because anesthesia is known to decrease IOP.[36]

While IOP plays a significant role in the diagnosis and treatment of glaucoma, it is equally important to identify early structural changes to the optic disc. Clinically, glaucoma is recognized by morphological remodeling of the optic nerve head and loss of vision. The ophthalmoscope was developed in the late 1850s and is still commonly used in the clinic to qualitatively assess the optic nerve head and fundus.[37] However, structural assessment by ophthalmoscopy is subjective, qualitative, has large interobserver and intraobserver variability, and has limited usability for identifying early glaucomatous damage and progression.[38-41] In-vivo monitoring of changes within the optic nerve head in combination with changes in retinal thickness assessed by optical coherence tomography (OCT) could improve our understanding of the pathogenesis of glaucomatous damage. Specifically, nerve fiber layer thickness measurements are

typically acquired around the optic nerve head and show that, in normal healthy human subjects, the peripapillary nerve fiber layer is thicker in the superior and inferior retinal quadrants and that these quadrants are more susceptible to damage in patients with glaucoma.[30, 42-44] Whether these quadrant specific thickness variations exist in rodents is still a matter of debate, with some histological studies showing that the highest density of retinal ganglion cells in rats is located between the superior and temporal retinal quadrants,[45-51] while others have not.[52] It is also unclear if the location of highest retinal ganglion cell density in the rat retina correlates with the retinal location where the nerve fiber layer/retinal ganglion cell layer is the thickest. A goal of this dissertation was to develop the analytical techniques needed to interpret the information contained in these OCT images and determine the value of measuring retinal thickness as an estimate of damage in a rat model of glaucoma.

1.3 Rodent Models of Glaucoma

There are several rodent models of glaucoma that mimic features of human glaucoma including genetic mouse models[53] and surgical disease induction in the rat.[54-57] In 1997, Morrison and colleagues described an episcleral venous injection of hypertonic saline that scleroses the aqueous outflow pathway and leads to chronic elevation in IOP.[56] This rodent model of glaucoma is appropriate for studying the correlation between IOP and disease progression because the hypertonic saline injection leads to structural changes at the optic nerve and loss of retinal ganglion cell density that correlates well with the induced elevated IOP.[58] Also, the damage to nerve fibers in this model of glaucoma can be mitigated through medications that lower IOP.[59]

It is important to point out that rodents may not be a particularly good model for structural changes in the optic nerve head, as they have a glial lamina and not a rigid collagenous lamina like humans or other primates.[60, 61] An advantage of using rats as a

model of glaucoma is that the size of their eye makes in-vivo imaging with OCT more feasible than the mouse eye. Also, while possible in mice, the surgical manipulations to elevate IOP are easier in the larger eye of the rat. An additional advantage of utilizing rodent models of glaucoma is that the time course of the disease is much faster, requiring only a few weeks to develop, as opposed years (as in humans) or months (as in non-human primate models of glaucoma), expediting the process of extracting valuable information about the pathophysiology of the disease.

1.4 Pressure Dynamics in Glaucoma

Why glaucoma occurs with normal tension glaucoma or does not occur in some patients with ocular hypertension has been debated for decades. The interplay between IOP, systemic mean arterial pressure and intracranial pressure may contribute to the pathogenesis of glaucomatous optic neuropathy.[62-64] For example, ocular perfusion pressure (difference between IOP and mean arterial pressure) likely contributes to glaucomatous damage when the eye's ability to regulate blood flow is no longer meeting metabolic demand.[65-70] He and colleagues showed that visual function was worse when high IOP coincided with low systemic blood pressure than with high blood pressure.[34] Also, optic nerve head cupping was more prominent with low intracranial pressure and normal IOP.[71] These studies suggest that increasing the traslaminar pressure difference by either elevating IOP or reducing intracranial pressure alters the homeostatic pressure balance and imparts stress at the lamina cribrosa that can result in glaucoma. Also, fluctuations in IOP, mean arterial pressure, and intracranial pressure may be associated with structural or vascular stress that could become critical enough to develop into glaucoma or contribute to its progression. Despite this knowledge, reduction of high IOP is the only treatable risk factor in glaucoma so far. Therefore, it would be beneficial to have an experimental animal model to investigate the role of these various

compartmental pressures and their role in the progression of structural and functional damage in experimental glaucoma. There are several fundamental questions that need to be asked before using animals for this purpose. For example, knowing the normal circadian rhythm of IOP and mean arterial pressure can shed light on the normal fluctuations in these animals. A goal of this dissertation was to establish the normal circadian rhythm of IOP and mean arterial pressure in rats housed in standard light-dark conditions.

1.5 Circadian Rhythms

Circadian rhythms refer to physiological, behavioral, and hormonal functions that display cyclical variations that can be synchronized to external cues, or Zietgeber, like the day-night cycle. Retinal light input is transferred to the suprachiasmatic nucleus (SCN) to regulate many of these circadian rhythms.[72-78] Also, certain peripheral organs have a built-in mechanism that also helps maintain their circadian rhythm.[79, 80] The idea of an organ regulating its own rhythm was supported by studies from a transgenic rat line in which luciferase is rhythmically expressed and controlled by the mouse Per1 promoter. [81, 82] The Per1 gene is part of the Period family of genes that are expressed in a cyclical pattern in the SCN.[83] These studies showed that the lung, liver, and muscle maintained their bioluminescent rhythm in-vitro and in the absence of the SCN.[81, 82]

A circadian rhythm of IOP is known to exist in human eyes,[84-87] rodents,[88-91] rabbits,[92] cats,[93] and dogs.[94] If these diurnal fluctuations in IOP are large enough, then they might be associated with disease progression among glaucoma patients.[95, 96] Quantifying the circadian rhythm of IOP may therefore help identify which aspect of IOP (e.g. between-visit fluctuations, peak IOP, diurnal fluctuations, etc.) is most significantly correlated with disease progression and this could ultimately lead to more effective glaucoma treatment strategies. The circadian rhythm of IOP was observed to be non-

existent when animals are housed in constant light.[58, 92, 94] The reduction in diurnal IOP variations is thought to be an advantage because it minimizes the number of times that IOP needs to be measured throughout the day and because it is easier to relate structural damage at the optic nerve head with measured IOP. However, previous studies have shown that the circadian rhythm of other biological function (e.g. activity, temperature) are maintained for weeks or months after animals are exposed to constant dark or light conditions.[97-100]

The first specific aim of this dissertation was to determine the circadian rhythm of IOP and mean arterial pressure in Brown Norway rats. Specifically, we evaluated if the circadian rhythm of IOP persisted in constant dim light conditions and investigate if IOP is regulated by the same mechanism that regulates circadian rhythm of core body temperature. These experiments are impactful because we characterized the correspondence between circadian rhythm of IOP and a reliable marker of the animal's individual circadian phase using telemetric data (body temperature) in Brown Norway rats. Lastly, we also measured the phase relationship between IOP and systemic mean arterial pressure in rats housed in standard light/dark conditions to determine the usability of the rat as a model to study the role of compartmental pressures and physiological rhythms in experimental models of glaucoma.

1.6 Ocular Imaging in Glaucoma

Axonal damage in glaucoma is presumed to start at the lamina cribrosa with secondary retrograde degeneration of the retinal ganglion cell somata.[101, 102] High IOP leads to bowing of the lamina cribrosa, which in turn leads to mechanical damage of axonal bundles and their blood supply.[5, 8] In-vivo quantification of the pattern of glaucomatous structural changes may give additional insight about the process of degeneration in glaucoma and enhance our understanding of how these structural

changes relate to functional vision loss. An understanding of the pattern of retinal ganglion cell degeneration is also important for diagnosing and monitoring the effectiveness of treatments in glaucoma. Numerous histological studies have evaluated the structural and cellular events of axonal degeneration in glaucoma ex vivo.[103, 104] For example, Chidlow and colleagues showed that one of the earliest indications of optic nerve damage in rats with experimental glaucoma was an accumulation of β-Amyloid precursor protein in the optic nerve head that resulted from disrupted axonal transport and that this event occurred within 8 hours of disease induction.[103] Spectral-domain optical coherence tomography (SD-OCT) is a non-invasive imaging system that can be used to evaluate changes in the optic nerve head and thickness changes to the nerve fiber layer in glaucoma. A goal of this dissertation was to assess the structural events of axonal degeneration with glaucoma in vivo using SD-OCT and the corresponding cellular degeneration associated with glaucomatous progression by histology. While imaging the rat eye with a clinical SD-OCT system is feasible, several challenges must be addressed before these images can be used to quantify the structural changes brought upon by an elevation in IOP.

Reproducibility of scanning the same retinal location between imaging session was a challenge that was addressed in this dissertation. The precision of retinal thickness measurements from SD-OCT data is influenced by factors that vary both within and between imaging sessions including factors related to the examiner (alignment, stability, focus, etc.), the subject (motion, optical clarity, etc.), image hardware (e.g. acquisition speed, resolution), and post-acquisition image processing routines (e.g. registration, segmentation, etc.). Despite these potential limitations, excellent repeatability of OCT thickness measurements has been reported in humans.[105-115] There are a number of additional unique considerations for achieving repeatable scan-path alignment with non-fixating anesthetized animal subjects that can

further influence reproducibility studies in the rodent eye.[116] Therefore, an alignment procedure was developed in this dissertation to scan the same retinal location between imaging sessions. We quantified the repeatability and reproducibility of thickness measurements and the effects of realignment and image quality on measurements of retinal thickness using SD-OCT imaging in the rat eye.

Also, in this dissertation, analytical tools were developed to compensate for lateral magnification in SD-OCT images caused by the high optical power and small axial length of the rat eye were developed.[117-119] Compensation for lateral magnification is an important consideration with SD-OCT imaging as this influences scan location and, in turn, correct interpretation of measurements that depend on precise positioning. It is important to point out that the axial dimension of an SD-OCT image is independent of the optical power of the eye and does not change after scaling for lateral magnification. In other words, correction of lateral magnification will not change thickness measurements, but will change retinal scan location and, if not controlled or compensated, will appear to influence thickness. These two challenges are important contributions because they enabled the analysis and quantification of the spatial and temporal structural changes (thickness changes and optic nerve head size) in a rat model of glaucoma.

1.7 Scope of Dissertation

The dissertation is organized as follows. In Chapter Two, the utility of a rebound tonometer to measure IOP in conscious rats was evaluated. This calibrated rebound tonometer was then used to quantify the circadian rhythm of IOP summarized in Chapter Three. Furthermore, in Chapter Three, we discuss the methods used to determine circadian phase from telemetric core body temperature measurements. The circadian phase relationship between IOP and mean arterial pressure are then discussed in

Chapter Four. The remaining chapters in this dissertation addressed the second specific aim and include the results from our *in vivo* imaging experiments in normal Brown Norway rats and rats with experimental glaucoma. Specifically, in Chapter Five we report factors (e.g. image alignment and image quality) that impact the repeatability and reproducibility of retinal thickness measurements by SD-OCT imaging in the rat eye. In Chapter Six, we investigated the use of a schematic model eye to compensate for lateral magnification in OCT images of the normal rat eye. In Chapter Seven, we implemented the analytical tools developed in Chapters Five and Six to quantify the spatial and temporal structural changes in a rat model of glaucoma. Finally, in the last chapter, Chapter Eight, the results from all experiments are summarized and possible future research directions are discussed.

Chapter Two

Reliability of Rebound Tonometry and Noninvasive Measurement of Intraocular Pressure in the Rat

Contributing Authors:

Diana C. Lozano, Nicolas Rodriguez, Nimesh Patel, Michael D. Twa

2.1 Preface

The objectives of these experiments were to validate and calibrate intraocular pressure (IOP) measurements taken with two different TonoLab rebound tonometers in cannulated rat eyes. The calibrated tonometers were then used to establish valid *in vivo* measurements of IOP in the Brown Norway rat. These experiments were an essential part of this dissertation because they enabled: (1) quantification of the circadian rhythm of IOP in rats (discussed in Chapter Three) and (2) the ability to measure IOP in a rat model of glaucoma (discussed in Chapter Seven). These IOP measurements were essential to relate structural changes (a decrease in retinal thickness and enlargement of the optic nerve head) to the measured IOP in this rat model of glaucoma.

2.2 Abstract:

Purpose: To evaluate the reliability of two TonoLab rebound tonometers for measurements of cannulated intraocular pressure (IOP) in the Brown Norway rat. These calibrated tonometers were then used to establish valid *in vivo* measurements of IOP in rats.

Methods: One eye from 18 male Brown Norway rats (average weight = 288 g) was cannulated with a 30 gauge needle that was connected in-line to a pressure transducer. One examiner raised or lowered IOP in predetermined randomized steps of 5 or 10 mm Hg (range 10 to 50 mm Hg) by adjusting a fluid-filled syringe. An examiner masked to the set pressure then measured IOP with two different rebound tonometers (TonoLab, Icare, Vantaa, Finland). Linear regression analyses were performed to determine the best calibration functions for each tonometer. The bias and 95% limits of agreement of IOP measurements were calculated to compare transducer pressures with rebound tonometer measurements. The two calibrated rebound tonometers were then used to measure IOP every two hours over the course of 24-hours in ten normal Brown Norway rats housed in standard light-dark conditions (LD) and in continuous dim light for 30 days (LL).

Results: The best-fitting calibration function for IOP was linear (all $r^2 > 0.92$). The mean difference between the pressure transducer and *TonoLab #1* was less than 1 mm Hg and for *TonoLab #2* was less than 3 mm Hg. The average 95% limits of agreement were smaller for *TonoLab #1* (± 4 mm Hg) than for *TonoLab #2* (± 6 mm Hg). Maximum IOP in LD was 32 ± 3 mm Hg and in LL was 31 ± 6 mm Hg. Minimum IOP in LD was 10 ± 1 mm Hg and in LL was 13 ± 1 mm Hg.

Conclusion: The TonoLab rebound tonometer is a reliable method of measuring IOP in the Brown Norway rat.

2.3 Introduction

Ocular hypertension is an important risk factor for primary open glaucoma, but it is not clear how the circadian rhythm of intraocular pressure (IOP), inter-visit fluctuations, or peaks in IOP impact glaucoma progression.[120-124] Animal models of glaucoma provide important information about the etiology and pathophysiology of the disease. Having a reliable method of measuring IOP in these animals would improve our understanding of the role of IOP dynamics on the pathogenesis of glaucoma. Currently, there are several models of glaucoma, including models utilizing non-human primates,[125-127] mice,[53, 128] and rats.[56, 57, 129-131] Rat models of glaucoma are advantageous because it is possible to measure IOP in un-anesthetized animals and the size of the rat eye makes it possible to surgically elevate IOP. One such model entails injecting hypertonic saline solution into the episcleral veins in adult Brown Norway rats to chronically elevate IOP.[56] IOP in this rat model of glaucoma has been measured with the TonoPen XL applanation tonometer. However, this tonometer is reported to be technically difficult to use and 10 – 15 measurements are needed to obtain an accurate measurement.[132-135] The rebound tonometer was developed to measure IOP in rodents. During rebound tonometry a small, magnetic, plastic-tipped pin is propelled towards the corneal apex, and IOP is proportional to the pin's rebound speed.

There are several factors that can add variability to IOP measurements, including anesthesia, the anxiety level of the animal, normal circadian rhythm , the tonometer, tonometer alignment with the corneal apex, and the experience of the investigator in handling animals and the tonometer. For example, Jia and colleagues report that IOP drops by approximately 10 mm Hg within 5 minutes of the animal being anesthetized.[36] The purpose of this study was to evaluate the reliability of two different rebound tonometers in measuring IOP in Brown Norway rats while controlling many other factors that contribute to *in vivo* measurement variability. These two rebound tonometers were

then used to evaluate the circadian rhythm of IOP in normal rats. Reliable tonometry measurements are essential for quantifying the circadian rhythm of IOP and relating the pressure level to structural changes in the retina and optic nerve head in a rat model of glaucoma.

2.4 Methods

2.4.1 TonoLab Rebound Tonometer Calibration

Two rebound tonometers of the same model (*TonoLab #1* and *TonoLab #2*) were used to measure IOP in cannulated eyes. Animals were anesthetized with an intraperitoneal injection of Ketamine (Vedco, St. Joseph, MO; 50 mg/kg) and Xylazine (Vedco, St. Joseph, MO; 5 mg/kg). Then, an eye from each animal was cannulated with a 30-gauge needle that was connected in-line to a pressure transducer (Keller, Series 41X). One examiner raised or lowered IOP by adjusting a fluid-filled precise micro-liter screw-top syringe (Hamilton Model 1001 LT Threaded Plunger). IOP was then randomly set to range between 10 to 50 mm Hg (in steps of 5 or 10 mm Hg). A second examiner, masked to the set pressure, measured IOP with each TonoLab rebound tonometer (Icare Rebound Tonometer, Vantaa, Finland). During rebound tonometry a small, magnetic, plastic-tipped pin is propelled towards the corneal apex. IOP is proportional to the pin's rebound speed. Ten pressure measurements were acquired at each pressure level, where each measurement is the mean of 6 readings (e.g. a total of 60 measurements were made at each pressure level). The relationship between TonoLab rebound tonometry and the pressure transducer was analyzed using linear regression analysis. The reliability of each TonoLab rebound tonometer was quantified by measuring the bias and 95% limits of agreement between the tonometer and the pressure transducer.

The reliability of each rebound tonometer was evaluated in three different experiments. The first two experimental set-ups entailed leaving the connection between the fluid-filled screw-top syringe and cannulated eye opened (Groups: *TonoLab #1 + Open* [n = 11 eyes] or *TonoLab #2 + Open* [n = 13 eyes]) or closed (Groups: *TonoLab #1 + Closed* [n = 6 eyes] or *TonoLab #2 + Closed* [n = 10 eyes]). In the last experiment, the micro-liter screw top syringe needle was removed and replaced with a syringe pump that was connected to a software controlled pressure transducer. This software was designed so that the user could enter the desired IOP level. Then, the pressure transducer would measure the pressure inside the eye and would send a signal to the computer to either push or pull fluid in the anterior chamber. The fluid was adjusted to maintain the IOP at the desired level in a closed-loop control system. This last experimental set-up was used with both rebound tonometers (Groups: *TonoLab #1 + Pump* [n = 4 eyes] or *TonoLab #2 + Pump* [n = 4 eyes]).

2.4.2 Noninvasive Intraocular Pressure Measurement in Rats

Noninvasive IOP measurements were acquired in Brown Norway rats (n = 10 rats) using the two calibrated rebound tonometers. Animals were behaviorally entrained and manually restrained during IOP measurements by gently placing the index finger at the base of their skull. This behavioral training lasted approximately one week and at the end of the training animals would hold still during IOP measurements. Circadian rhythm of IOP was evaluated by measuring IOP every two hours over a 24-hour period. A deep-red headlight was used to measure IOP when the lights were off. Ten IOP measurements were acquired at each time point. These experiments were carried out while the animals were housed in standard light-dark environmental conditions (lights on at 7 AM and lights off at 7 PM) and after the animals were exposed to continuous dim light (40 – 90 lux) for 30 days. The mean, maximum, and minimum IOP measurements

acquired during these 24-hour experiments were compared between lighting conditions. Lastly, the persistence of these diurnal IOP variations was evaluated by measuring IOP twice (at 8 AM and 8 PM) during the day for three consecutive days when the animals were housed in standard light-dark conditions.

2.5 Results

2.5.1 TonoLab Rebound Tonometer Calibration

Figure 2.1 shows the transducer pressure recordings while IOP was being measured with the rebound tonometer. These recordings show that IOP was set to 20 mm Hg and that this pressure was maintained for 40 to 80 seconds to acquire all IOP measurements. The transducer was sensitive enough to record transient changes in IOP due to heart rate and reflexive contraction of extraocular muscles response after instilling a drop of PBS in the cannulated eye. . **Tables 2.1** and **2.2** summarize the results of the cannulation calibration study. Briefly, the relationship between the pressure transducer and TonoLab rebound tonometer over the full range (10 to 50 mm Hg) was highly linear, with correlations all higher than 0.92 (**Table 2.1** and **Figure 2.2**). The biases (mean difference between pressure transducer and tonometer) were smaller than 1 mm Hg for *TonoLab #1* (**Table 2.2** and **Figure 2.3**) and smaller than 3 mm Hg for *TonoLab #2* (**Table 2.2** and **Figure 2.3**). The 95% limits of agreement between the pressure transducer and rebound tonometer were better for *TonoLab #1* (± 4 mm Hg) than for *TonoLab #2* (± 6 mm Hg; **Figure 2.3**). The calibration functions for both TonoLab tonometers were linear and the 95% prediction intervals were also smaller for *TonoLab #1* than *TonoLab #2* (**Figure 2.4**).

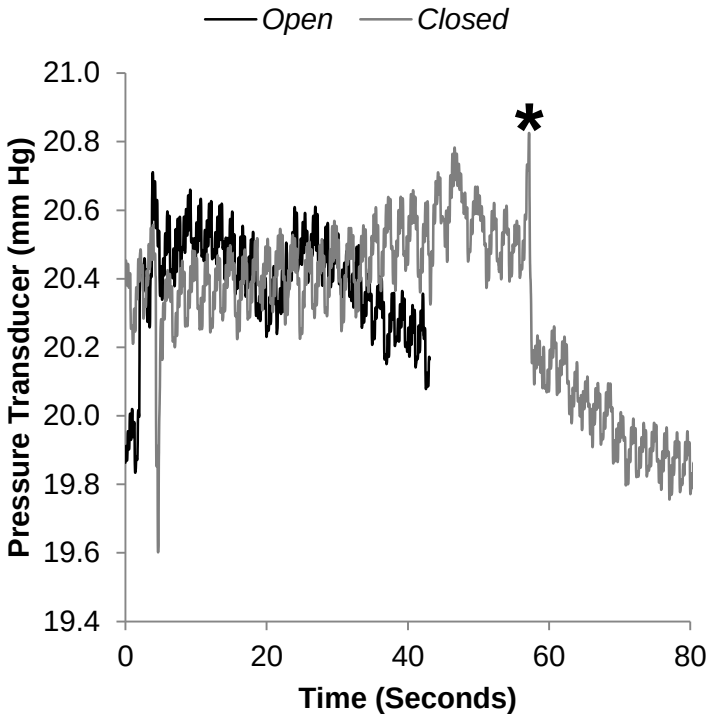

Figure 2.1: Pressure transducer recordings acquired while measuring IOP with the rebound tonometer in a cannulated rat eye and for two experimental conditions (Open and Closed).

Open (black line) means that the connection between the cannulated eye and syringe controlling IOP was left opened; Closed (gray line) means that this connection was closed off. These recordings show that IOP was set to 20 mm Hg and that this pressure was maintained for the 40 to 80 seconds needed to measure IOP with the rebound tonometer. Also, it shows that the transducer was sensitive enough to record heart rate (high frequency component) and reflexive contraction of extraocular muscles response (asterisk) after instilling a drop of PBS in the cannulated eye.

Table 2.1: Reliability and Prediction Equations for *TonoLab #1*

	Open	**Closed**	**Pump**
Linear Regression	y = 0.96x - 0.46; r^2 = 0.96	y = 1.0x - 0.45; r^2 = 0.98	y = 1.0x - 0.1; r^2 = 0.96
Transducer - Tonometer; (95% Limits of Agreement)	1 mm Hg; (–3 to 6 mm Hg)	0 mm Hg; (–4 to 4 mm Hg)	1 mm Hg; (–4 to 6 mm Hg)
Prediction Equation	y = 1.0x + 1.5; r^2 = 0.96	y = 1.0x + 1.1; r^2 = 0.98	y = 1.0x + 1.1; r^2 = 0.96
95% Prediction Interval	± 4.8 mm Hg	± 3.9 mm Hg	± 5.8 mm Hg

Open means that the connection between the cannulated eye and syringe controlling IOP was left opened; *Closed* means that this connection was closed off; *Pump* refers to using a software controlled syringe pump to regulate IOP.

Table 2.2: Reliability and Prediction Equations for *TonoLab #2*

	Open	**Closed**	**Pump**
Linear Regression	y = 0.9x - 0.3; r^2= 0.92	y = 0.9x + 0.5; r^2= 0.93	y = 1.0x - 1.1; r^2= 0.95
Transducer - Tonometer (95% Limits of Agreement)	3 mm Hg; (–4 to 9 mm Hg)	1 mm Hg; (–5 to 8 mm Hg)	0 mm Hg; (–7 to 8 mm Hg)
Prediction Equation	y = 1.0x + 2.5; r^2 = 0.92	y = 1.0x + 1.5; r^2 = 0.93	y = 0.9x + 2.6; r^2 = 0.95
95% Prediction Interval	± 7 mm Hg	± 6.5 mm Hg	± 7.2 mm Hg

Open means that the connection between the cannulated eye and syringe controlling IOP was left opened; *Closed* means that this connection was closed off; *Pump* refers to using a software controlled syringe pump to regulate IOP.

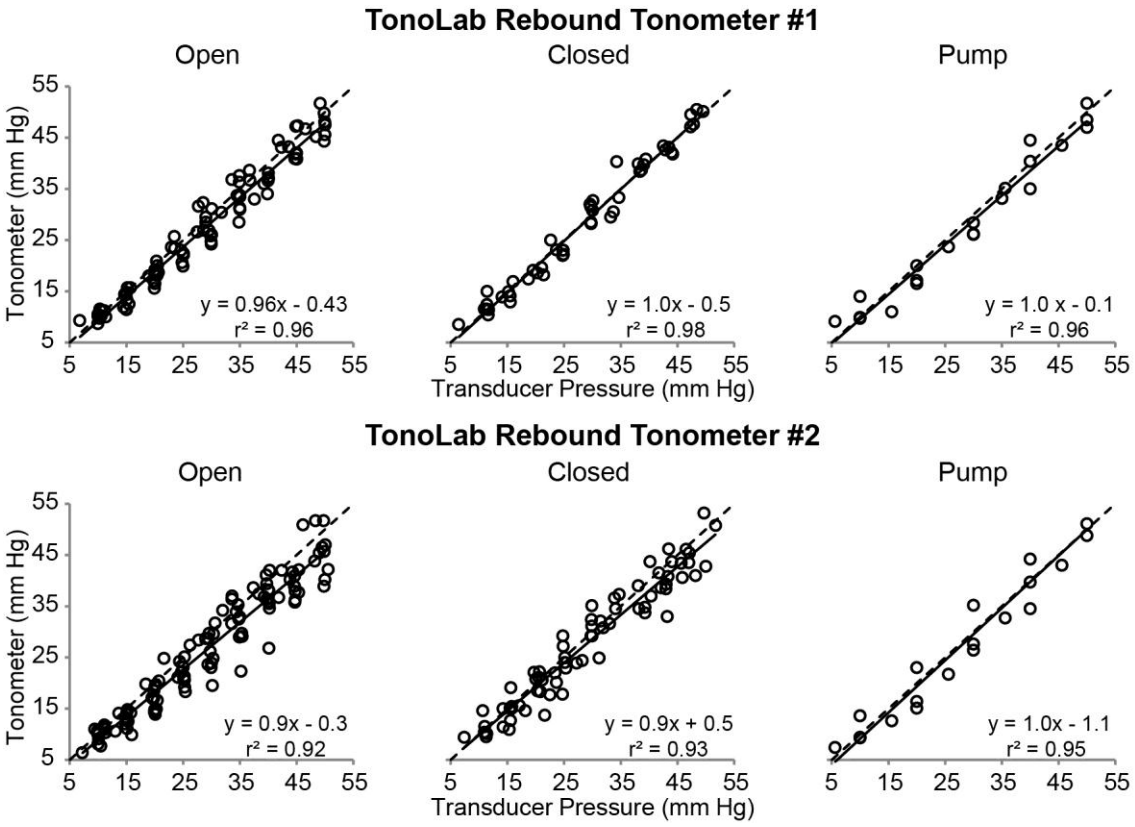

Figure 2.2: Relationship between pressure transducer and rebound tonometer by experimental set-ups (Open, Closed, Pump).

Open means that the connection between the cannulated eye and syringe controlling IOP was left opened; *Closed* means that this connection was closed off; *Pump* refers to using a software controlled syringe pump to regulate IOP. The relationship between transducer and both tonometers was linear for all experimental conditions (solid black line). For example, the top three graphs show that the relationship between *TonoLab #1* and the pressure transducer was highly linear, with correlations higher than 0.96 regardless of experimental set-up. The bottom three graphs show that the relationship between *TonoLab #2* and the pressure transducer was also highly linear, with correlations higher than 0.92 regardless of experimental set-up. Dashed lines represent the 1:1 relationship between transducer and tonometer.

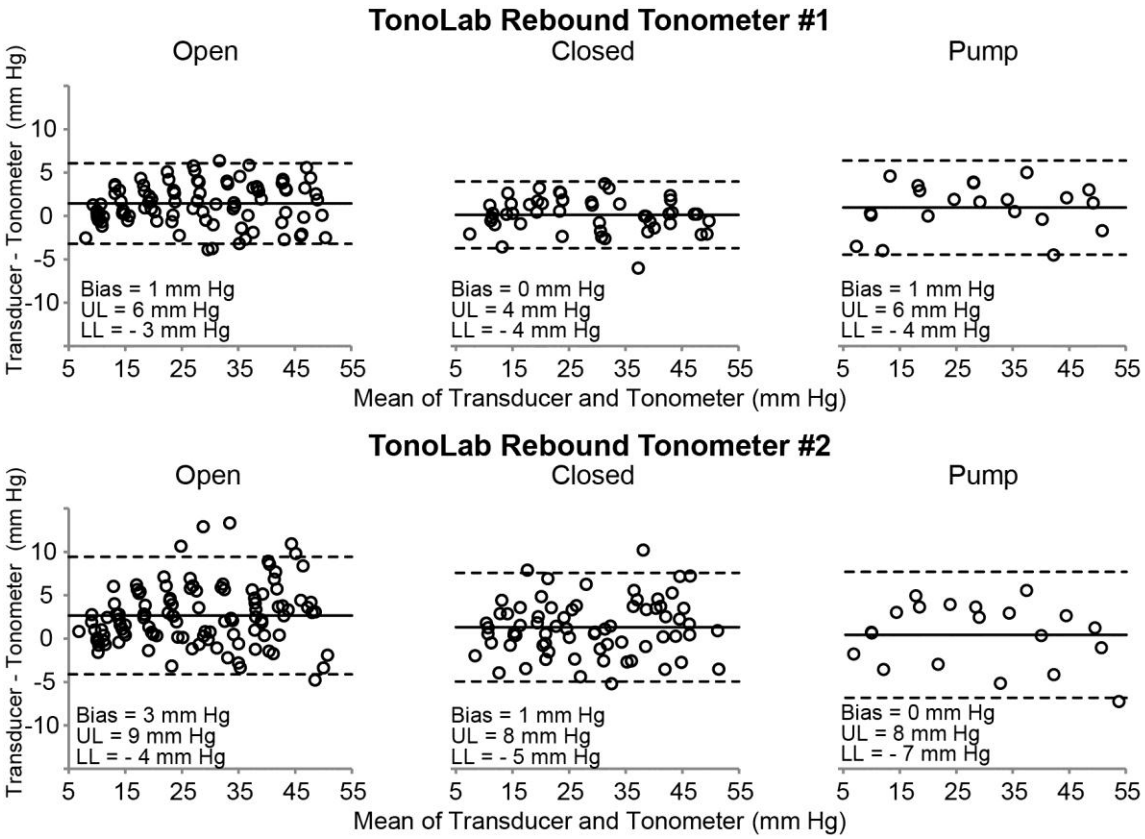

Figure 2.3: Measuring the agreement between the TonoLab rebound tonometers and pressure transducer for all three experimental set-ups (Open, Closed, and Pump).

Open means that the connection between the cannulated eye and syringe controlling IOP was left opened; *Closed* means that this connection was closed off; *Pump* refers to using a software controlled syringe pump to regulate IOP. The biases (averaged difference between transducer and tonometer; Solid line) were all smaller than 3 mm Hg. The 95% limits of agreement (dashed lines) were smaller for *TonoLab #1* than for *TonoLab #2* under all experimental set-ups. For example, the 95% limits of agreement with the *Closed* experimental set-up were ± 3.8 mm Hg for *TonoLab #1* and ± 6.3 mm Hg for *TonoLab #2*.

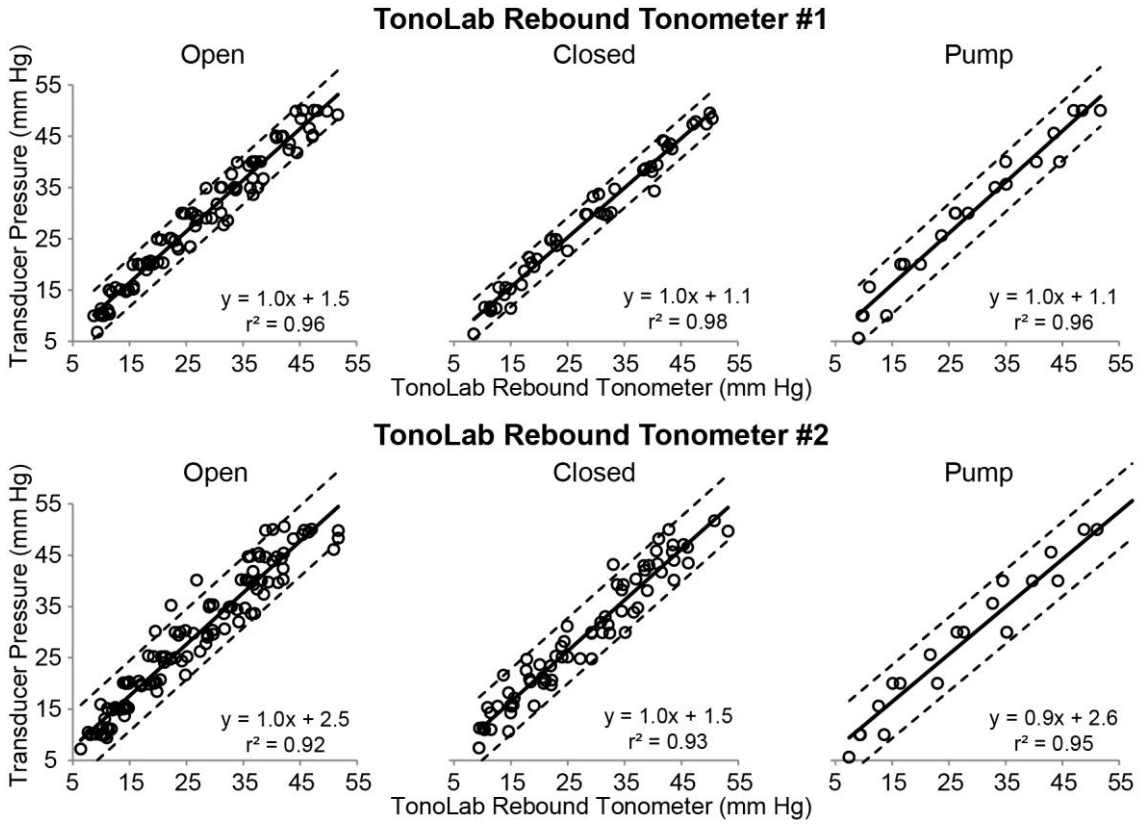

Figure 2.4: Predicting transducer measured intraocular pressure (IOP) from TonoLab rebound tonometer measurements for all experimental conditions (Open, Closed, and Pump).

Open means that the connection between the cannulated eye and syringe controlling IOP was left opened; *Closed* means that this connection was closed off; *Pump* refers to using a software controlled syringe pump to regulate IOP. The 95% prediction intervals were smaller for *TonoLab #1* than *TonoLab # 2* for all experimental set-ups. For example, with the *Closed* experimental set-up, the 95% prediction intervals were ± 3.9 mm Hg for *TonoLab #1* and ± 6.5 mm Hg for *TonoLab #2*.

2.5.2 Noninvasive Intraocular Pressure Measurement in Conscious Rats

The circadian rhythm of IOP was detected in conscious animals housed in standard light-dark environmental conditions and after 30-days of continuous exposure to dim light. IOP varied over the course of the day under both experimental lighting conditions (**Figure 2.5**). Mean diurnal IOP measured in standard light-dark environmental conditions (18 ± 2 mm Hg; 95% CI: 17 – 20 mm Hg) was not different than that measured when the animals were housed in continuous dim light (19 ± 3 mm Hg; 95% CI: 17 – 21 mm Hg; $P = .38$). Maximum IOP was also similar when measured in light-dark environmental conditions (32 ± 3 mm Hg; 95% CI: 29 – 34 mm Hg) and continuous dim light (31 ± 6 mm Hg; 95% CI: 27 – 36 mm Hg; $P = .77$). However, minimum IOP was significantly lower when measured in light-dark environmental conditions (10 ± 1 mm Hg; 95% CI: 10 – 11 mm Hg) than in continuous dim light (13 ± 1 mm Hg; 95% CI: 12 – 14 mm Hg; $P = .0001$). Lastly, in standard light-dark environmental condition, the 8 PM IOP measurement was 28 ± 2 mm Hg and this was 10 mm Hg higher than the 8 AM measurements (18 ± 1 mm Hg; $P < .001$; **Figure 2.6**).

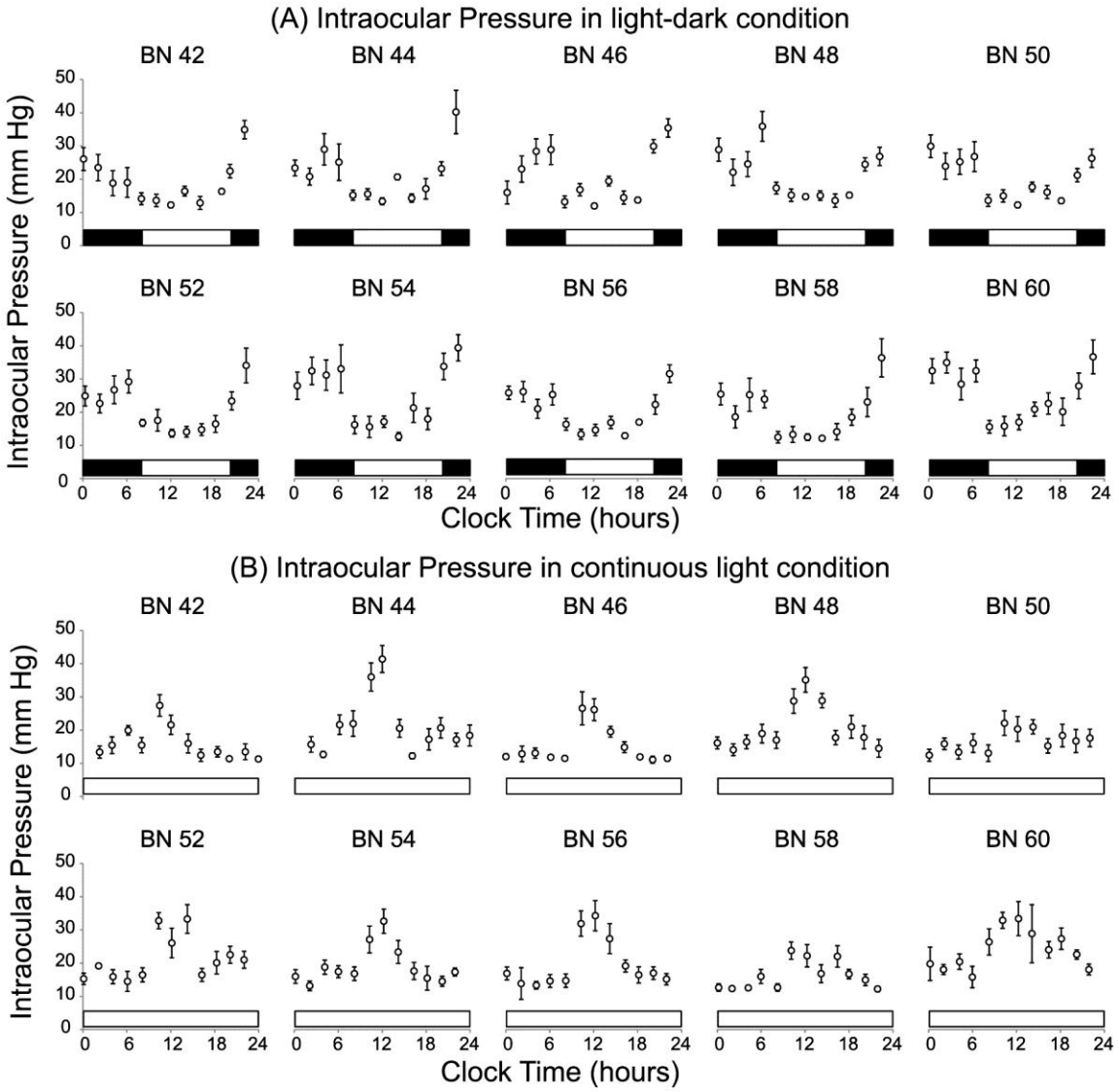

Figure 2.5: The circadian rhythm of intraocular pressure (IOP) in ten Brown Norway rats housed in (A) standard light-dark conditions and (B) after 30 days exposure to continuous dim light.

The open circles are the raw (mean ± standard deviation) IOP measurements. The bars above the x-axis in (A) indicate the times during the day that the lights were off (black bars) or on (white bar). The white bar above the x-axis in (B) indicates that the lights were on all day. IOP was measured in **(A)** light-dark conditions and then measured again after **(B)** 30-days of exposure to continuous dim light.

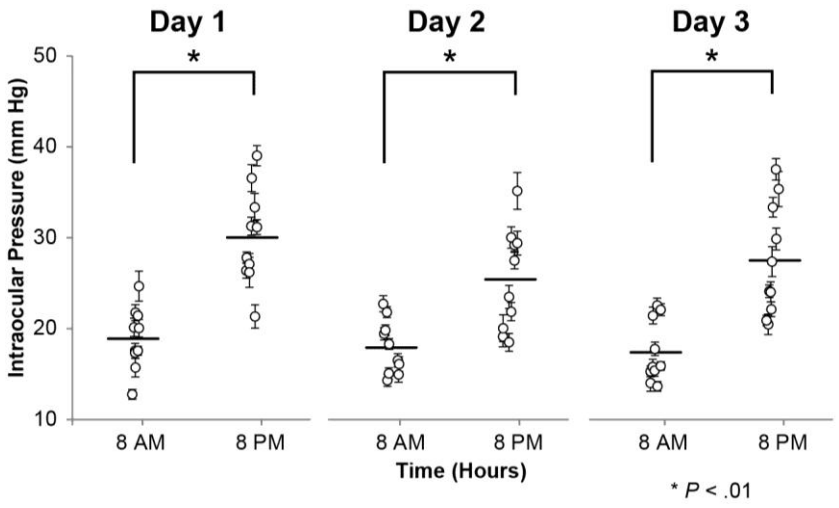

Figure 2.6: Intraocular pressure (IOP) measured in ten normal adult Brown Norway rats housed in standard light-dark environmental conditions.

Measurements were acquired twice a day for three consecutive days. Measurements were taken an hour after the lights came on (8 AM) and an hour after the lights were turned off (8 PM). Open circles are mean (± standard error) IOP for each animal. The solid horizontal line is the mean IOP for all animals. These measurements show that IOP varies between animals, that IOP is higher during the dark-phase than light-phase, and that this pattern is maintained for several days.

2.6 Discussion

The TonoLab rebound tonometer is a reliable method to measure IOP in rats. Each tonometer had different calibration curves, suggesting that it is important to calibrate each tonometer before utilizing it in animals. Three experimental set-ups were evaluated: (1) *Open* means that the connection between the cannulated eye and the syringe used to adjust IOP was left opened; (2) *Closed* means that this connection was closed off; and (3) *Pump* refers to closed-loop IOP control using a software controlled syringe pump to keep IOP at the desired pressure level while measurements were being acquired. The general findings from these experiments show that the TonoLab rebound tonometer is a reliable method to measure IOP in rats. This was demonstrated by the small bias and tight 95% limits of agreements measured with both *Open* and *Closed* experimental set-ups. The 95% limits of agreement were wider with the *Pump* experimental set-up. Theoretically, the *Pump* experimental set-up should have performed better than the *Open* or *Closed* experimental set-ups because the pump dynamically pushes or pulls fluid from the anterior chamber depth when the pressure transducer reports pressure values outside the desired level. It is likely that adding more samples to this experimental group would have improved these results. Lastly, the bias and 95% limits of agreement were larger with *TonoLab #2* than with *TonoLab #1.* These results highlight that there are intrinsic differences between rebound tonometers and not all rebound tonometers have similar reliability. Groups using this tonometer need to perform their own calibration experiments to determine the reliability of their rebound tonometer.

The calibrated TonoLab rebound tonometers were then used to quantify the circadian rhythm of IOP in Brown Norway rats housed in standard light-dark environmental conditions. The results from this study showed that IOP varies over the

course of the day (**Figure 2.5**) and that these variations are maintained for several days (**Figure 2.6**).

Non-invasive measurements of IOP are needed to evaluate how ocular hypertension damages optic nerve fibers in animal models of experimental glaucoma. The rebound tonometer,[136-139] TonoPen tonometer, [132-135, 140] Goldmann tonometer,[141, 142] and telemetric systems[89] have been used to measure IOP in rodents. In particular, Mermoud and colleagues used the TonoPen to measure IOP in 229 normal Lewis rats and showed that IOP between 8:30 – 9:30 AM was 16.98 ± 5.17 mm Hg.[140] These results are similar to the 8 AM measurements reported in the current study (18 ± 1 mm Hg), however, our measurements are less variable than those reported by Mermoud. In the current study, a 10 mm Hg IOP difference was measured between the 8 AM and 8 PM measurements and these results are similar to those reported by Moore and colleagues (dark-phase: 31.3 ± 1.3 mm Hg; light-phase: 19.3 ± 1.9 mm Hg).[91] In conclusion, the TonoLab is a reliable method for measuring IOP in the Brown Norway rat, making it a valuable tool for tracking IOP changes in the rat model of glaucoma.

Chapter Three

Circadian Rhythm of Intraocular Pressure in the Adult Rat

Contributing Authors:

Diana C. Lozano[1], Andrew T.E. Hartwick[2], Michael D. Twa[1]

1. University of Houston College of Optometry

2. The Ohio State University College of Optometry

Submitted for Review to Chronobiology International on September 21, 2014

3.1 Preface

In this chapter, the circadian rhythm of IOP was quantified in relation to the animal's temperature rhythm when animals are housed in standard light-dark environmental conditions and in continuous dim light (40 – 90 lux). The main findings from this study were that there is a persistent, but dampened, circadian rhythm of IOP in continuous dim light and that the circadian rhythms of temperature and IOP are not synchronized by the same central oscillator.

3.2 Abstract

Ocular hypertension is a risk factor for developing glaucoma, which consists of a group of optic neuropathies characterized by progressive degeneration of retinal ganglion cells and subsequent irreversible vision loss. Our understanding of how intraocular pressure (IOP) damages the optic nerve is based on clinical measures of IOP that only gives a partial view of the dynamic pressure load inside the eye. IOP varies over the course of the day and the oscillator regulating these diurnal changes has not yet been conclusively identified. The purpose of this study was to compare and contrast the circadian rhythms of IOP and body temperature in Brown Norway rats when these animals are housed in standard light-dark and continuous dim light (40 – 90 lux) conditions. The results from this study show that there is a persistent, but dampened, circadian rhythm of IOP in continuous dim light and that the circadian rhythms of temperature and IOP are not synchronized by the same central oscillator. We conclude that once- or twice-daily clinical measures of IOP are insufficient to describe IOP dynamics. Similarly, our results indicate that, in experimental animal models of glaucoma, the common practice of housing animals in constant light does not necessarily eliminate the potential influence of IOP rhythms on the progression of nerve damage. Future studies should aim to determine whether an oscillator within the eye regulates the rhythm of IOP and to better characterize the impact of glaucoma on this rhythm.

3.3 Introduction

Glaucoma is a group of optic neuropathies characterized by progressive degeneration of retinal ganglion cells and their axons that ultimately leads to irreversible vision loss. Elevated intraocular pressure (IOP) is a risk factor for developing glaucoma and several studies have indicated that lowering IOP slows progression.[143-149] Much of what is known about glaucoma has come from animal models, including those involving rats,[56, 57, 129-131] that have characterized the structural and functional changes associated with elevated IOP.[4, 33, 150, 151] However, there remains ongoing debate about the influence of the circadian rhythm of IOP on the development and progression of glaucoma.

Our understanding of IOP dynamics and its contribution to the disease process is partly limited by the tonometry techniques commonly employed in clinical practice. Usually, a single IOP measurement is taken at each patient visit, which often occurs months apart. These IOP 'snapshots' are insufficient to characterize pressure variations due to disease, in addition to typical diurnal pressure variations. A circadian rhythm of IOP is known to exist in normal human eyes,[84-87] rodents,[88-91] rabbits,[92] cats,[93] and dogs.[94] These diurnal fluctuations in IOP might be associated with disease progression among glaucoma patients.[95, 96] Quantifying the circadian rhythm of IOP may therefore help identify which aspect of IOP is most significantly correlated with disease and its progression (e.g. between-visit fluctuations, peak IOP, diurnal fluctuations, etc.) and this could lead to more effective glaucoma treatment strategies.

While a circadian rhythm of IOP has been measured under normal environmental conditions (e.g. regular day-night cycles), the rhythm was not detected in rats,[58] rabbits,[92] and dogs[94] kept in a continuous light environment. However, these studies did not simultaneously monitor the animals' circadian phase, which is known to drift in constant light or dark environmental conditions that enable an animal's internal circadian clock to 'free-run'. Without an external time cue (light onset or offset) to synchronize the

IOP rhythms, inter-individual variations in the free-running circadian period would cause the pressure rhythms for rats in an experimental cohort to go out of phase with each other. By grouping the IOP measurements by an external clock, the presence of any persistent cyclical rhythm could be masked or appear considerably dampened. The purpose of this study was to measure the circadian rhythm of IOP in Brown Norway rats and determine whether this rhythm is regulated by a central oscillator. To test this hypothesis, we compared IOP rhythms occurring under constant light conditions to core body temperature rhythms, the latter serving as an independent marker of circadian phase.

3.4 Methods

The Institutional Animal Care and Use Committee of the University of Houston approved all experimental and animal care procedures and experiments were carried out in accordance with the recommendations in the Guide for the Care and Use of Laboratory Animals of the National Institutes of Health. Eleven adult male Brown Norway rats (average ± SD weight: 357 ± 32 g) were housed individually in transparent cages with food and water available ad libitum.

The circadian rhythms of core body temperature and IOP were assessed in two groups of animals. **Figure 3.1** illustrates the experimental timeline. Briefly, temperature was measured in Group 1 (n = 4 animals) in standard light-dark environmental conditions (LD) and in continuous dim light (40 – 90 lux) for four weeks. In Group 2 (n = 7 animals), temperature was recorded in continuous dim light (40 – 90 lux) for 7 weeks and then for 1 month during re-entrainment to standard light-dark environmental conditions. The circadian rhythm of IOP was characterized by measuring IOP every two hours over the course of 26-hours. Three 26-hour experiments were performed in Group 1; one in standard light-dark environmental conditions and two in continuous dim light

(after 1 and 4 weeks exposure to continuous dim light). Two 26-hour experiments were carried out with Group 2; one after 7 weeks of continuous dim light exposure and another one after the animals were re-entrained to standard light-dark environmental conditions. These experiments are further discussed in the following methods sections.

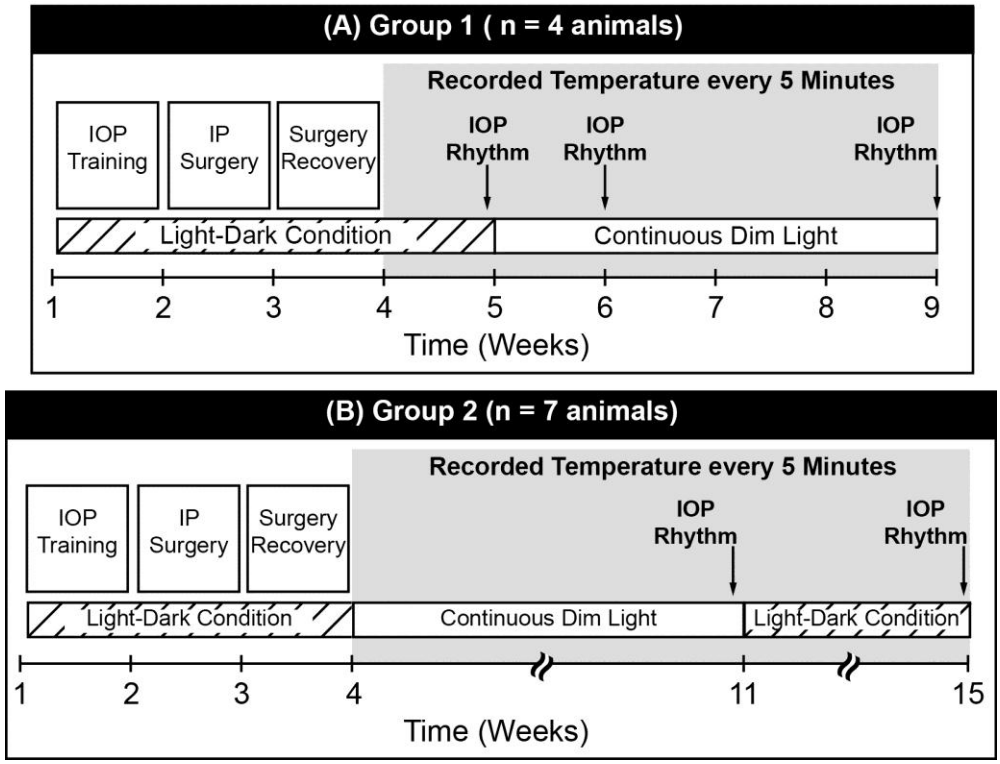

Figure 3.1: Experimental timeline used to quantify the circadian rhythm of intraocular pressure (IOP) and core body temperature in two groups of animals.

Both groups were initially housed in standard light-dark environmental conditions. Animals were trained during *Week 1* to hold still while measuring IOP. An intraperitoneal temperature sensor was implanted (IP surgery) during *Week 2*. Animals recovered from surgery during *Week 3*. Body temperature measurements were then obtained every 5 min until the end of each protocol (gray shaded area). IOP rhythms were measured every two-hours over the course of 26-hours at distinct time-points. **(A)** In group 1, IOP rhythm in the light-dark condition was measured at the end of *Week 5*. IOP rhythm was re-evaluated in Group 1 after being housed in continuous dim light for 1-week (end of *Week 6*) and 4-weeks (end of *Week 9*). **(B)** In Group 2, IOP rhythm was evaluated after the animals had been placed in continuous dim light for 7-weeks and was re-evaluated after the animals had been exposed to standard light-dark conditions for 4-weeks.

3.4.1 Quantifying the Circadian Rhythm of Core Body Temperature

Core body temperature was measured with a temperature sensor that was implanted intraperitoneally (Respironics Company, Mini Mitter, Bend, OR). The implant sensor was set to automatically record core body temperature every 5 minutes for five weeks in Group 1 and for eleven weeks in Group 2. Animals were kept in standard light-dark environmental conditions (lights on at 8 AM and lights off at 8 PM) prior to implanting the temperature sensor. Rats were anesthetized during the implant surgical procedure with an intraperitoneal injection of ketamine (Vedco, St. Joseph, MO; 50mg/kg) and xylazine (Vedco; 5 mg/kg). Post-operative pain was minimized with a single dose of ketoprofen (Fort Dodge Animal Health, Fort Dodge, IA; 100 mg/mL). Animals were allowed to recover from surgery for one week before temperature data was included in the study (**Figure 3.1**).

The circadian rhythm of core body temperature was evaluated by fitting a cosine function to the raw daily temperature data.[152-154] This procedure is commonly referred to as a cosinor analysis. Various parameters were extracted from the cosinor analysis, including the daily mean core body temperature (M ; *Equation 1*), the time when the maximum core body temperature occurs (φ; *Equation 1*), and the maximum range of temperature measurements within a day ($2 \times A$; *Equation 1*). Temperature onset time, defined as the time when temperature started to rise above the 24-hour mean, was calculated by taking the first derivate (e.g. the point of inflection) of the cosine fit function. Temperature period length (τ) was calculated from the linear regression slope of daily temperature onset times versus all days that temperature was recorded. The existence of a rhythm was quantified by calculating daily rhythmicity (correlation of determination of the cosine fit multiplied by 100%) and by testing the null hypothesis of zero-amplitude at a statistically significant level of probability (F-test; $P < .05$).

$$y = M + A\cos\left(\frac{2\pi}{\tau} \times t + \varphi\right) \quad [Equation\ 1]$$

3.4.2 Quantifying the Circadian Rhythm of Intraocular Pressure

IOP was measured in both eyes from conscious rats every two hours over a 26-hour period (**Figure 3.1**). Prior to surgical implantation of the temperature sensors, animals were trained to hold still during IOP measurements. This behavioral training was performed over the course of one week prior to surgery. During the 26-hour experiments, two-trained handlers measured IOP using two calibrated rebound tonometers (TonoLab, Icare, Vantaa, Finland).[137, 155] During rebound tonometry a small, magnetic, plastic-tipped pin is propelled towards the corneal apex. IOP is proportional to the pin's rebound speed. Ten pressure measurements were acquired for each eye every two hours, for the full 26-hour measurement period. A deep-red headlight was used to facilitate the measurement of IOP during the dark phase of the light-dark environmental condition. To minimize systematic bias, the order in which each animal was measured, the tonometer used to acquire the measurements, and the investigator handling each animal were randomized. IOP measurements from only the right eyes were included in the analysis. The circadian rhythm of IOP was quantified using the previously described cosinor analysis. The difference was that the period length (τ) of the cosine fit (*Equation 1*) was set to the temperature period length so that the phase relationship of the IOP rhythms could be quantified in relation to the animal's core body temperature rhythm.

3.4.3 Phase Relationship between Core Body Temperature and Intraocular Pressure

The phase relationship between core body temperature and IOP was investigated to evaluate if these two physiological functions are synchronized to the same central oscillator. This phase relationship was plotted in polar graphs to visually inspect the concordance between temperature and IOP phase. For example, the clustering of all points in the same polar quadrants supports the premise that the same

central oscillator regulates both physiological functions. The polar graphs were generated by calculating the time at which the maximum temperature and IOP occurred. These times were then transformed from peripheral clock time to either Zeitgeber Time (for standard light-dark environmental conditions) or Circadian Time (for continuous dim light). In Zeitgeber Time, light onset is recorded as the 0.0 h timepoint and light offset is recorded as the 12.0 h timepoint in a standard 12 h/12 h light/dark cycle. Circadian Time is based on the free-running period of a rhythm and the temperature onset time (defined above) in nocturnal animals is set as the 12.0 h timepoint. Time in the polar graphs was indicated by the angle of a vector whose length was 1 when analyzing the temperature and IOP data measured in standard light-dark environmental condition. In continuous dim light, the length of the vector was set to a ratio that was normalized to values measured in standard light-dark conditions. This ratio was used to highlight if the rhythm dampened in continuous dim light. Lastly, the phase relationship was quantified by measuring the difference between the time when core body temperature and IOP were at their maximum.

3.5 Results

3.5.1 Quantifying the Circadian Rhythm of Core Body Temperature

Core body temperature in standard light-dark environmental conditions was lowest during the light-phase (36.9 ± 0.1 °C; 95% CI: 36.8°C – 37.0 °C), highest during the dark-phase (37.5 ± 0.2 °C; 95% CI: 37.4 °C – 37.7 °C), and peaked near the middle of the dark phase (17.5 ± 1.9 Zeitgeber Time; 95% CI: 17.1 to 17.8 Zeitgeber Time). Other parameters of the body temperature rhythm are summarized in **Table 3.1**. A persistent but dampened temperature rhythm was measured in continuous dim light. For example, the maximum range in temperature measurements within a day was larger in standard light-dark environmental conditions (0.60 ± 0.11 °C) than that measured after 7-weeks of exposure to continuous dim light (0.34 ± 0.07 °C).

Table 3.1: Circadian rhythm of core body temperature by lighting condition

Light Condition	Group	Mean ± SD (95% Confidence Interval)		
		Rhythmicity [%]	24-hour Mean [°C]	Temperature Range [°C]
LD	1 & 2	46 ± 21 (32 – 60)	37.2 ± 0.1 (37.1 – 37.3)	0.60 ± 0.11 (0.44 – 0.74)
1 week in LL	1	19 ± 6 (9 – 28)	37.0 ± 0.2 (36.7 – 37.2)	0.32 ± 0.03 (0.20 – 0.42)
4 weeks in LL	1	10 ± 2 (7 – 13)	37.0 ± 0.2 (36.7 – 37.4)	0.26 ± 0.02 (0.20 – 0.30)
7 weeks in LL	2	17 ± 7 (10 – 23)	37.1 ± 0.1 (37.0 – 37.2)	0.34 ± 0.07 (0.20 – 0.43)

Mean temperature recorded under all lighting conditions by experimental group. Light condition LD refers to animals being housed in standard light-dark environmental conditions and LL refers to animals that were housed in continuous dim light. Two groups of animals were included in this study; Group 1 (n = 4 animals) was first housed in LD and transferred to LL for 4 weeks; Group 2 (n = 7 animals) was housed in LL for 7-weeks and then switched to LD. Rhythmicity refers to the correlation of determination of the cosine fit times 100%.

Figure 3.2 shows temperature data recorded from one animal and illustrates the circadian rhythm of temperature that occurs under continuous dim light (**Figure 3.2A**) and standard 12 h/12 h light-dark environmental conditions (**Figure 3.2B** and **Figure 3.2C**). In continuous dim light, the temperature rhythm drifted forward relative to external time, indicating that the rhythm was free-running and being regulated by an internal biological clock (**Figure 3.2A**). Temperature rhythm drifted forward at a rate that ranged between 0.5 to 0.8 hours per day, which translated to a longer period length (24.6 ± 0.3 hours; 95% CI: 24.5 – 24.8 hours) than that measured in light-dark conditions (P = .001). This forward drift persisted for four days after the animal returned to standard light-dark conditions before synchronizing with the external lighting cycle once again (**Figure 3.2B**). Temperature period length in the light-dark condition was 24.0 ± 0.2 h (95% CI: 23.9 – 24.2 h; **Figure 3.2C**).

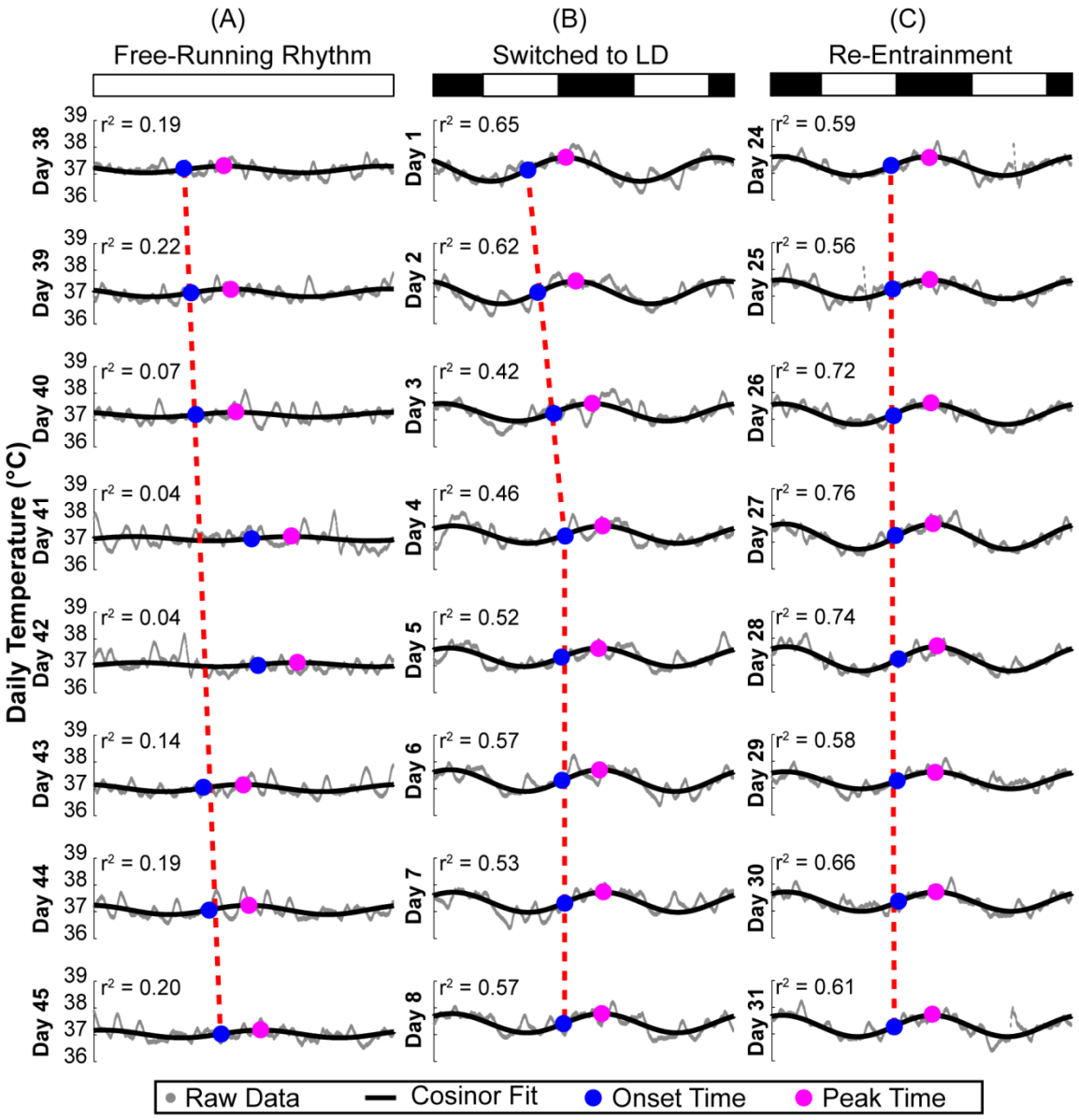

Figure 3.2: Diurnal temperature variations in standard light-dark environmental conditions and continuous dim light for one representative animal from Group 2.

The gray line represents the raw temperature data, blue dots indicate temperature onset times and magenta points indicate temperature peak times. The black line is the least-squared cosine fit through the raw temperature data and the correlation of determination (r^2) are shown for each graph. **(A)** Temperature recorded after 38 – 45 days exposure to continuous dim light and shows that temperature onset time drifted forward in continuous

dim light. **(B)** Temperature recorded for the first 8 days after the animal was switched to light-dark environmental conditions. Temperature onset time drifted forward for the first four days of re-entrainment and then it consistently occurred at the beginning of the dark phase. **(C)** Temperature recorded when the animal had re-entrained to the light-dark conditions for four weeks. Temperature onset time in standard light-dark conditions consistently occurred at the beginning of the dark phase and temperature peaked in the middle of the dark phase.

3.5.2 Quantifying the Circadian Rhythm of Intraocular Pressure

IOP measurements acquired from two animals during the 26-hour experiments are shown in **Figure 3.3**. IOP in the standard light-dark condition was lowest during the light-phase (16 ± 2 mm Hg), highest during the dark-phase (30 ± 7 mm Hg), and peaked near the middle of the dark phase (16.6 ± 1.2 Zeitgeber Time; 95% CI: 15.8 to 17.4 Zeitgeber Time). Rhythmicity analysis showed that a dampened circadian rhythm of IOP persisted while the animals were maintained in continuous dim light ($P < .001$; **Table 3.2**). The maximum range of IOP measurements was 14 ± 3 mm Hg under light-dark conditions, and this maximum range dampened to 8 ± 1 mm Hg after 1 week (Group 1), 8 ± 2 mm Hg after 4 weeks (Group 1) and 6 ± 1 mm Hg after 7 weeks (Group 2) of exposure to continuous dim light (**Table 3.2**).

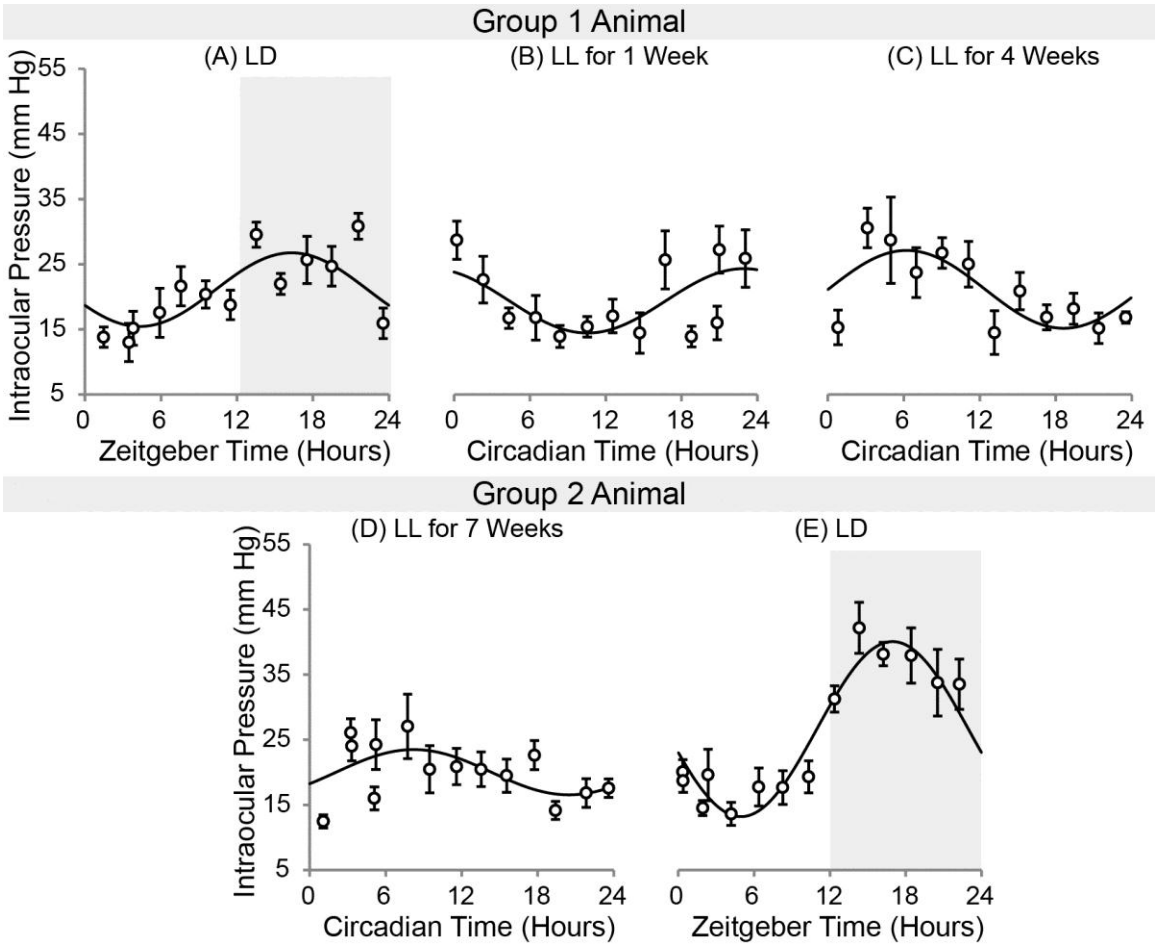

Figure 3.3: Circadian rhythm of intraocular pressure (IOP) in two Brown Norway rats (a Group 1 animal and a Group 2 animal) housed in standard light-dark conditions and in continuous dim light.

The open circles are the raw (mean ± standard deviation) IOP measurements. The cosine fits for IOP (black solid line) are plotted in either Zeitgeber Time (when animals were kept in light-dark environmental conditions) or Circadian Time (when animals were housed in continuous dim light). In the Group 1 animal, IOP was measured in **(A)** light-dark conditions and then measured again after **(B)** 1 week and **(C)** 4 weeks of continuous dim light exposure. In the Group 2 animal, IOP was measured **(D)** after being housed for 7 weeks in continuous dim light and **(E)** then after it re-entrained to the standard light schedule.

Table 3.2 : Circadian rhythm of intraocular pressure by lighting condition

Light Condition	Group	Mean ± SD (95% Confidence Interval)				
		Rhythmicity [%]	24-hour Mean [mm hg]	IOP Range [mm Hg]	Maximum [mm Hg]	Minimum [mm Hg]
LD	1 & 2	46 ± 14 (37 – 55)	22 ± 3 (20 – 24)	14 ± 3 (10 – 18)	30 ± 7 (25 – 34)	16 ± 2 (14 – 17)
1 Week in LL	1	24 ± 7 (13 – 35)	18 ± 2 (16 – 21)	8 ± 1 (6 – 12)	23 ± 2 (19 – 26)	14 ± 1 (12 – 16)
4 Weeks in LL	1	30 ± 14 (8 – 51)	20 ± 2 (18 – 23)	8 ± 2 (2 – 14)	27 ± 6 (17 – 37)	13 ± 5 (6 – 21)
7 Weeks in LL	2	20 ± 10 (11 – 30)	22 ± 2 (20 – 23)	6 ± 1 (4 – 8)	25 ± 2 (23 – 26)	18 ± 2 (16 – 20)

Mean intraocular pressure measured under all lighting conditions by experimental group. Light condition LD refers to animals being housed in standard light-dark environmental conditions and LL refers to animals that were housed in continuous dim light. Two groups of animals were included in this study; Group 1 (n = 4 animals) was first housed in LD and transferred to LL for 4 weeks; Group 2 (n = 7 animals) was housed in LL for 7 weeks and then switched to LD. Rhythmicity refers to the correlation of determination of the cosine fit analysis multiplied by 100%.

3.5.3 Phase Relationship between Core Body Temperature and Intraocular Pressure

The relationship between core body temperature and IOP are illustrated in **Figure 3.4** (for all Group 1 animals) and **Figure 3.5** (for all Group 2 animals). Temperature and IOP peaked at a similar time when the animals were housed in the standard 12 h/12 h light-dark conditions. The mean difference between the timepoints for maximum temperature and IOP measurements was not significantly different from zero for Group 1 (+1.8 ± 1.4 h; 95% CI: -0.4 to 4.1 h; *P* = .08) or for Group 2 (-0.1 ± 0.6 h; 95% CI: -0.63 to 0.43 h; *P* = .65), indicating that both physiological functions peaked at the same time under these environmental conditions. However, temperature and IOP peaked at different times when the animals were place in continuous dim light. In Group 1, this time difference was -4.6 ± 1.0 h (95% CI: -6.1 to -3.0 h) after 1 week of continuous dim light exposure and +9.5 ± 6.8 h (95% CI: -1.3 to 20.3 h) after 4 weeks of continuous dim light exposure. In Group 2, the time difference was +6.2 ± 8.4 h (95% CI: -1.5 to 14.0 h) after 7 weeks of continuous dim light exposure. These results are further summarized in the polar graphs shown in **Figure 3.6**. These polar graphs show that, in standard light-dark environmental conditions, both maximum temperature and maximum IOP occurred near the middle of the dark phase (**Figure 3.6A**). In continuous dim light, Circadian Time is based on the free-running period of a rhythm and the temperature onset time in nocturnal animals is set as the 12.0 h timepoint. For this reason, the temperature peak times for all animals line up at the same time (**Figure 3.6B** to **Figure 3.6D**). These figures also show that, in continuous dim light, the time when IOP peaked drifted further away from the time when temperature peaked (**Figure3. 6B** to **3.6D**). The distribution of when IOP peaked was normally distributed around the clock after 7-weeks of exposure to continuous dim light (**Figure 3.6D**). These results collectively indicate that the circadian phase between core body temperature and IOP was synchronized under

light-dark environmental conditions, but then the circadian phase of IOP rhythm drifted relative to the phase of core body temperature rhythm under constant light conditions.

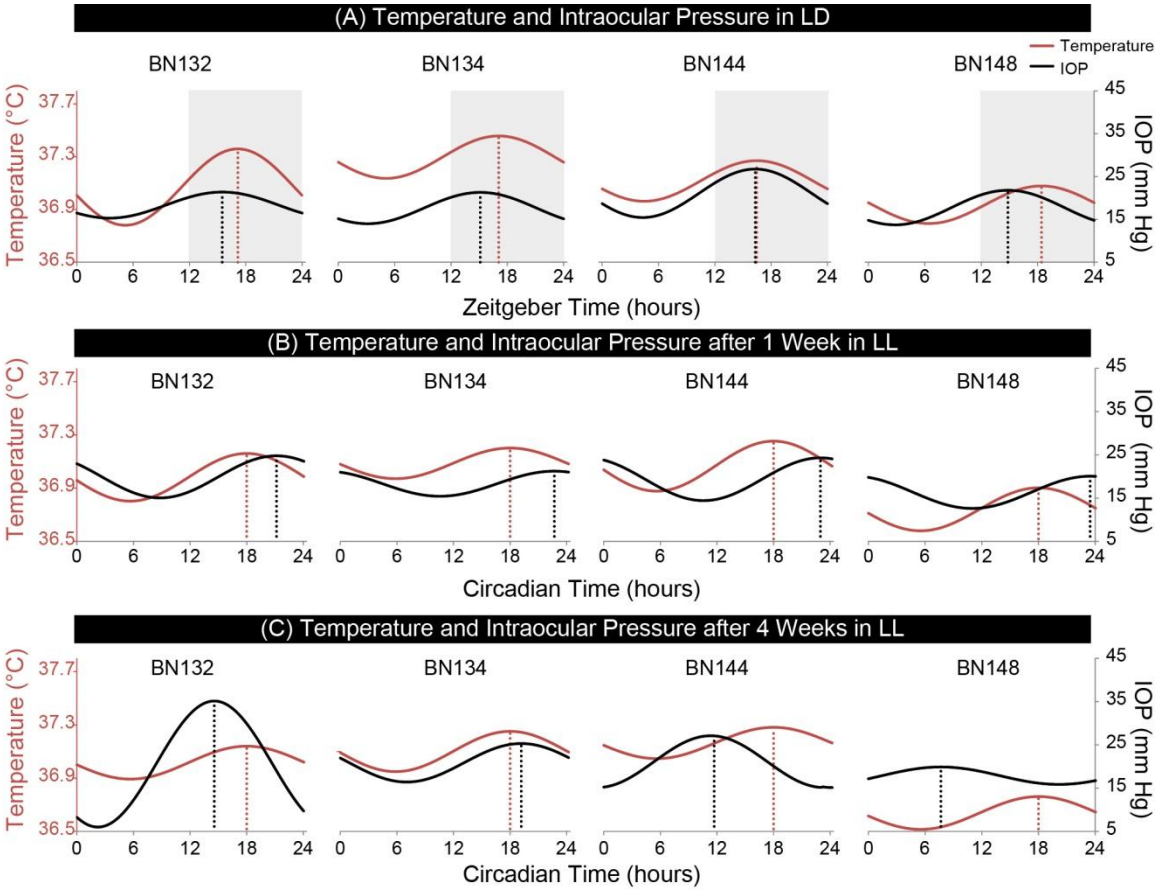

Figure 3.4: Relationship between core body temperature (red solid lines) and intraocular pressure (black solid lines) cosine-fit results for all animals in Group 1 **(A)** in standard light-dark conditions, **(B)** after 1 week in continuous dim light, and **(C)** after 4 weeks in continuous dim light. Temperature peak time is indicated by the red dashed line and intraocular pressure peak time is indicated by the black dashed line.

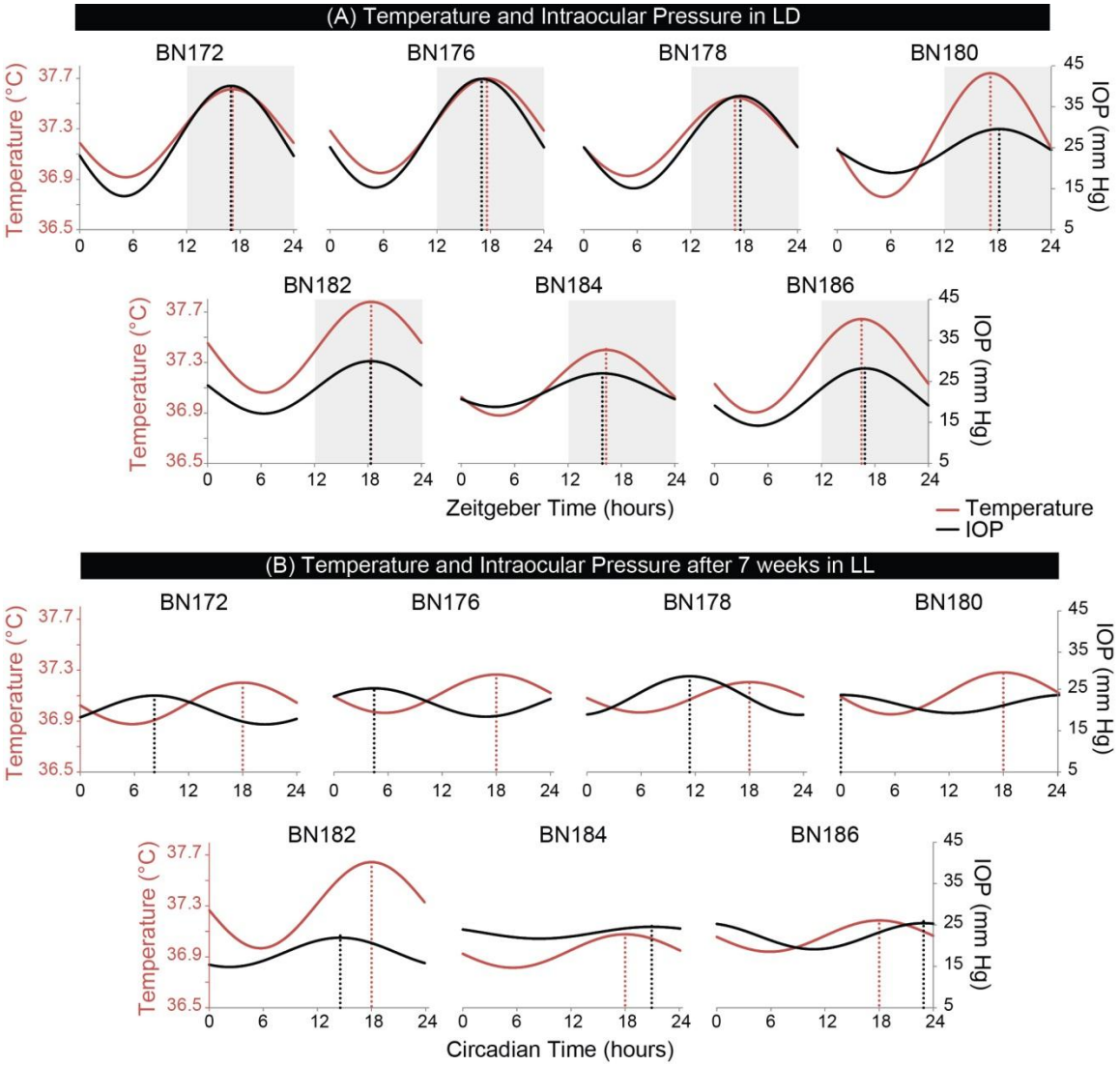

Figure 3.5: Relationship between core body temperature (red solid lines) and intraocular pressure (black solid lines) cosine-fit results for all animals in Group 2 **(A)** in standard light-dark conditions, and **(B)** after 7 weeks in continuous dim light. Temperature peak time is indicated by the red dashed line and intraocular pressure peak time is indicated by the black dashed line.

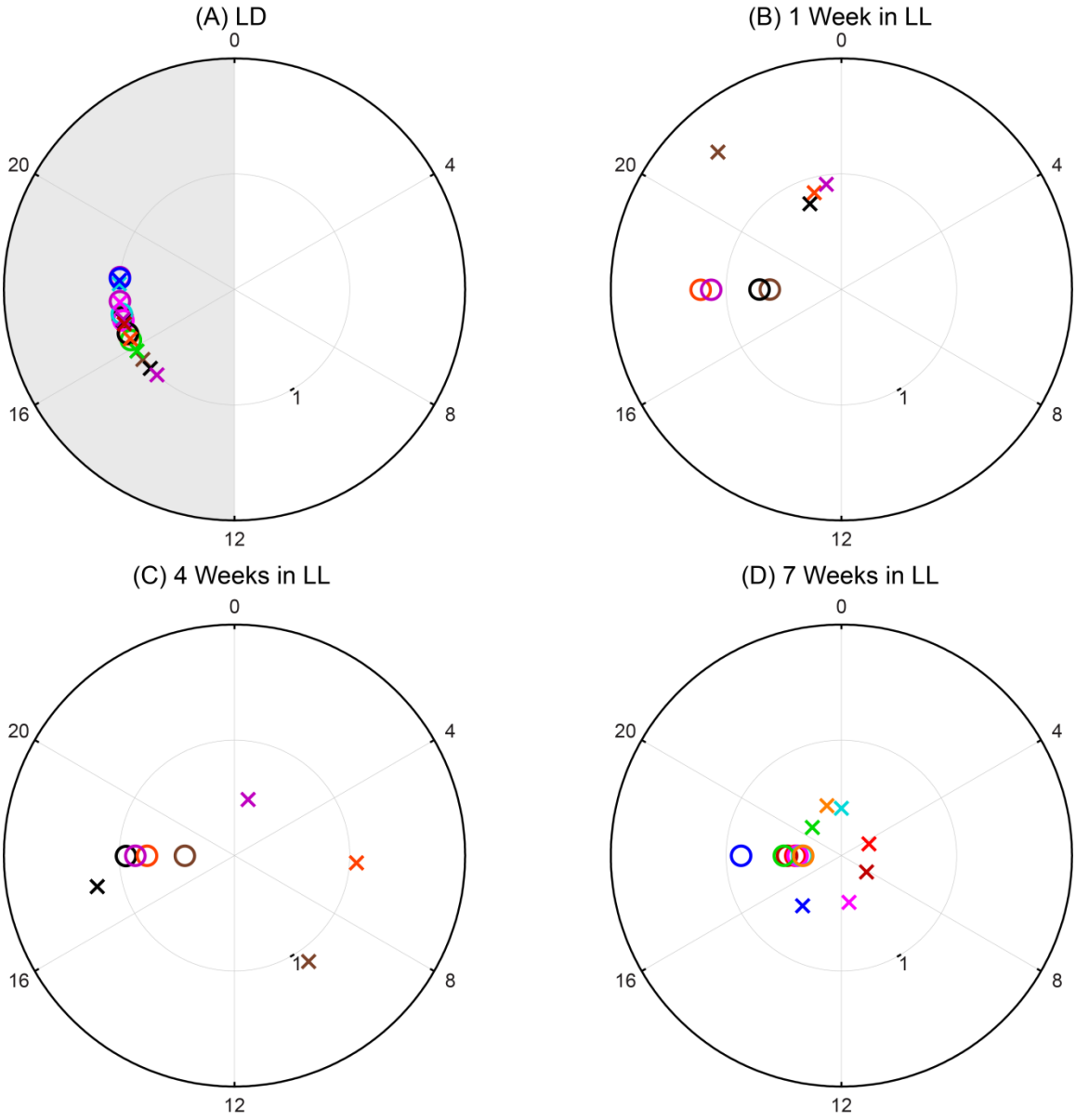

Figure 3.6: Relationship between core body temperature (○) and intraocular pressure (×) peak times in standard light-dark environmental conditions (LD), and 1, 4, and 7 weeks of exposure to continuous dim light (LL).

Points are color coded by animal. **(A)** Plotting Zeitgeber Time (clockwise) at a normalized radial distance of 1. In standard light-dark environmental conditions, temperature and intraocular pressure peaked at similar times near the middle of the dark phase. **(B – D)** Plotting Circadian Time at a radial distance equal to the normalized

amplitude (e.g. temperature amplitude in LL divided by the temperature amplitude in LD). The difference between temperature and intraocular pressure peak times was more variable in continuous dim light and amplitude dampened in all animals housed in continuous dim light for 7 weeks.

3.6 Discussion

In this study, we quantified the circadian rhythm of IOP in adult rats and determined the phase relationship between the timing for this rhythm and that for core body temperature, a commonly used circadian phase marker.

A normal temperature circadian rhythm was measured under standard light-dark environmental conditions and a dampened but significant rhythm was still present after up to seven weeks of continuous dim light exposure. It has been previously reported that, although there is a gradual decrease in the amplitude, circadian temperature rhythms can still be observed in rats that have been maintained in continuous light conditions for several weeks.[97, 98, 100] Light intensity is also an important consideration when measuring any physiological function under free-running conditions because the coherence of the rhythm decreases more quickly with increasing light intensity.[156, 157] With the dim light used in the current study (40 – 90 lux), our finding that the temperature rhythms persisted after one to seven weeks in constant light conditions is therefore consistent with the results reported in these previous studies.

Others have shown the TonoLab rebound tonometer to be a repeatable and accurate method of measuring IOP in rats,[139, 158] and we have verified the applicability of this device in our lab (Lozano DC *et al.*, IOVS, 2009, 50: ARVO E-Abstract: 2853). With this tonometer, we quantified the fluctuation in IOP that occurs across a standard 12 h/12 h light-dark cycle, and showed that the peak of this pressure rhythm occurs during the dark phase, as has been described previously.[91] In the current study, a smaller-amplitude but significant IOP rhythm could still be detected after the animals had been exposed to continuous dim light for one to seven weeks (**Table 3.2**). Morrison and colleagues reported that no diurnal variation in IOP was detected in Brown Norway rats housed in continuous dim light for 35 days, even though their experimental set-up and light intensity was similar to that used in the current study.[58] However, in this prior study,

IOP was only measured twice a day and the timing of these measurements was based on an external (morning and evening) timing schedule. In nocturnal animals exposed to continuous light, the circadian period generally lengthens,[159] a finding that is consistent with the temperature rhythm data outlined in the present study. Therefore, the peak and trough for daily IOP values would be expected to gradually shift, in terms of external time, from when they occurred while the animals were maintained on a standard light-dark condition. Furthermore, due to the absence of any external synchronization cues (i.e. zeitgebers) during the continuous light exposure, variations in each animal's circadian period would cause the animals in an experimental cohort to gradually become significantly out-of-phase with each other over time. Averaging data that was obtained from multiple animals at potentially different times in their internal circadian phase would mask detection of an underlying rhythm. In this study, we obtained 13 IOP measurements over a 26-h period, and performed cosinor analysis on data obtained from each individual animal. This may explain the apparent discrepancy in our finding of a significant rhythm for IOP that persisted for weeks in constant light, as opposed to those reported in previous studies on rats, rabbits and beagles that characterized rhythmicity using time-point averaged data.[58, 92, 94]

Comparing the rhythm of IOP to that for core body temperature, which served as an independent marker of circadian phase, we showed that these two rhythms became uncoupled from each other after the animals had been exposed to the continuous light conditions (**Figure 3.6**). In the rat, the rhythms of core body temperature, locomotor activity and plasma corticosterone all remain synchronized with each other in continuous light conditions, indicating that these rhythms are regulated by a common central oscillator.[99] Our finding that the separation between the peak times for IOP and body temperature increased with longer exposure to continuous dim light indicates that a separate oscillator is the primary regulator for IOP rhythms. The location of this oscillator

is a subject for future research, but one intriguing possibility is that it may be located peripherally within the eye itself.

Even though we have the ability to accurately and repeatedly measure IOP, this study still has the limitation that we only acquired a limited number of IOP measurements. These discrete measurements only give a partial view of IOP dynamics over the course of the day. New technology is now emerging to continuously monitor the circadian rhythm of IOP. For example, contact lenses[160-163] and implantable sensors[164] are available to measure IOP in humans. Telemetric systems are being developed and tested to acquire continuous IOP measurements in non-human primates,[165] rabbits,[166-168] and mice.[89] A more thorough description of IOP dynamics will become possible and further enhance our understanding of how fluctuations in this physiological variable contribute to glaucomatous disease progression.

Rat models of elevated IOP have been used extensively to model glaucomatous pathophysiology. It has become standard practice to house the rats used in these experiments in constant light.[169-174] With the assumption that there is negligible diurnal variation in IOP under these conditions, the advantage of this approach is that a single measurement was thought to provide a reasonable estimate of the cumulative pressure exposure for that day. However, we found that a significant pressure rhythm can persist for weeks in constant light (see **Figure 3.4**, **Figure 3.5** and **Table 3.2**). Thus, the daily variation in IOP may influence the progression of optic nerve damage in these experimental glaucoma models to a greater extent than previously appreciated. This finding supports the use of more continuous recording techniques in order to more definitively measure cumulative pressure exposure.

In summary, the results from this study show that there is a persistent circadian rhythm of IOP in continuous dim light and that the same central oscillator does not regulate the circadian rhythms of temperature and IOP. Future studies on the rhythm of

IOP should benefit from the development of more continuous data acquisition techniques, which will enable the impact of glaucoma on this rhythm to be better characterized.

Chapter Four

Circadian Phase Relationship between Intraocular Pressure and Mean Arterial Pressure in Normal Rats

Contributing Authors:

Diana C. Lozano, Jessica Lee, Laura Frishman, Andrew T.E. Hartwick, and Michael Twa

4.1 Preface

The purpose of these experiments was to measure the diurnal rhythm of mean arterial pressure and intraocular pressure (IOP) in normal rats housed in standard light-dark conditions. The general findings from this study were that IOP peaked during the dark phase (active phase) and that blood pressure peaked during the light phase (resting phase). The 9 hour phase lag between IOP and blood pressure likely puts the optic nerve head at risk for reduced vascular supply at night when blood pressure is at a minimum and IOP is at a maximum.

4.2 Abstract

Purpose: To determine the phase relationship between the circadian rhythms of intraocular pressure and mean arterial pressure in normal rats.

Methods: The circadian rhythms of **i**ntraocular pressure (IOP) and mean arterial pressure were measured in 8 adult Brown Norway rats that were housed in 12 hours of light and 12 hours of darkness. IOP was measured every two hours over the course of 24 hours using two calibrated rebound tonometers. Mean arterial pressure was measured with a non-invasive tail-cuff system. IOP was measured first at each time point followed by mean arterial pressure measurements. The circadian rhythms were quantified by fitting a cosine function to mean pressure values.

Results: Significant time-dependent variations in IOP were detected in all animals. Mean IOP during the light phase was 18 ± 2 mm Hg and 24 ± 2 mm Hg during the dark phase. Mean arterial pressure measurements from two animals were excluded from the analysis because they did not show a significant rhythm. Mean arterial pressure during the light phase in the remaining six animals was 101 ± 3 mm Hg and was 94 ± 3 mm Hg during the dark phase. On average, IOP peaked 4.6 hours after the lights turned off and blood pressure peaked 4 hours before the lights turned off.

Conclusion: The 9 hour phase lag between IOP and blood pressure likely puts the optic nerve head at risk for reduced vascular supply at night when blood pressure is at a minimum and IOP is at a maximum.

4.3 Introduction

Glaucomatous optic neuropathies are affected by the balance of intraocular pressure (IOP), systemic mean arterial blood pressure, and intracranial pressure.[175-177] Disregulation of ocular perfusion pressure (mean arterial pressure minus IOP) can contribute to the development of glaucomatous neuropathy.[65-70] For example, glaucomatous damage may occur when a spike in IOP coincides with a drop in blood pressure. The circadian rhythms of each parameter (IOP and blood pressure) have been characterized independently, but the exact diurnal phase relationship between these two physiological functions has not been measured in the same animal. The purpose of this work was to quantify the circadian rhythm of IOP and mean arterial pressure in normal Brown Norway rats and determine the phase relationship between these two physiological functions. Furthermore, the results from this study can be used to develop a model to quantify the interactions between mean arterial pressure, IOP and corresponding optic nerve damage.

4.4 Methods

The experimental design was to measure IOP and blood pressure every two hours over the course of 24 hours. At each timepoint, IOP was measured first, followed by blood pressure measurements. Eight retired breeder Brown Norway rats (8 months old) were house individually in clear cages with free access to food and water.

IOP was measured in right eyes from un-anesthetized rats every two hours over a 24 hour period. During the 24 hour experiments, two-trained handlers measured IOP using two calibrated rebound tonometers (TonoLab, Icare, Vantaa, Finland; See Chapter Two).[137, 155] Ten pressure measurements were acquired for each eye every two hours, for the full 24 hour measurement period. A deep red headlight was used to facilitate the measurement of IOP during the dark phase of the light-dark environmental condition.

The circadian rhythm of IOP was evaluated as previously described in Chapter Three. Briefly, a cosine function (commonly referred to as the Cosinor method) was fitted to the mean IOP measurements.[152-154] Diurnal mean IOP (M ; *Equation 1*), the time when the maximum IOP occurs (φ; *Equation 1*), and the maximum range of IOP measurements ($2 \times A$; *Equation 1*) were calculated. Physiological parameters measured in standard light-dark conditions closely follow a 24 hour period, and for that reason, period length (τ) in Equation 1 was set to 24. The existence of a rhythm was quantified by calculating daily rhythmicity (correlation of determination of the cosine fit multiplied by 100%) and by testing the null hypothesis of zero-amplitude at a statistically significant level of probability (F-test; $P < .05$).

$$y = M + A\cos\left(\frac{2\pi}{\tau} \times t + \varphi\right) \quad [Equation\ 1]$$

Mean arterial pressure was measured with a tail-cuff system (CODA, Kent Scientific; Torrington, CT). This system uses two tail cuffs to measure systolic and diastolic blood pressure. The first cuff is an occlusion cuff that is placed at the base of the tail in order to restrict tail blood flow when inflated. This occlusion cuff slowly deflates and the second cuff (the volume pressure recoding cuff), which is placed below the occlusion cuff, estimates blood pressure as blood flow returns to the tail. Animals were placed in tube holders on top of a warming platform during all blood pressure measurements. Animals were trained to hold steady while blood pressure measurements were being acquired. This behavioral training occurred at least one to two weeks before measuring the circadian rhythm of blood pressure. The training entailed placing the animals in the tube holders and warming platform to get them acclimated to the measurement procedure. Ten blood pressure measurements were acquired at each time point during the 24 hour experiment. Blood pressure measurements acquired when the animals moved were excluded from the analysis. A

total of 11% of the measurements were excluded. The circadian rhythm of mean arterial pressure was then quantified by fitting a cosine function to the blood pressure data as described above.

4.5 Results

Significant time-dependent variations in IOP were detected in all animals (**Table 4.1**). Mean IOP during the light phase was 18 ± 2 mm Hg and was 24 ± 2 mm Hg during the dark phase (**Figure 4.1**). The 24-hour mean IOP calculated from the Cosinor method was 21 ± 3 mm Hg (95% CI: 19 – 23 mm Hg) and the mean range was 10 ± 3 mm Hg (95% CI: 8 – 12 mm Hg) across all animals. The blood pressure data from two animals were excluded from the analysis because they did not show a significant rhythm (**Table 4.2**). Mean arterial pressure during the light phase was 101 ± 3 mm Hg and was 94 ± 3 mm Hg during the dark phase (**Figure 4.2**). The 24-hour mean for blood pressure in the remaining six animals was 97 ± 6 mm Hg (95% CI: 91 – 104 mm Hg) and the maximum range was 21 ± 7 mm Hg (95% CI: 13 – 28 mm Hg). The circadian rhythms of IOP for the same six animals for which a significant circadian rhythm of blood pressure was detected are plotted in **Figure 4.3.** The phase relationship between IOP and blood pressure is highlighted in **Figure 4.3** and shows that IOP peaked 4.6 hours after the lights turned off and blood pressure peaked 4 hours before the lights turned off. These results show that there is about a 9 hour phase lag between the mean times when IOP and mean arterial pressure peaked.

Table 4.1: Cosine Fit Parameters for Intraocular Pressure

ID	Mean (mm Hg)	Range (mm Hg)	Rhythmicity (%)	P Value
BN132	18	6	30	<0.001
BN134	18	7	43	<0.001
BN144	21	11	46	<0.001
BN148	18	8	32	<0.001
BN180	24	11	34	<0.001
BN182	24	12	44	<0.001
BN184	23	8	32	<0.001
BN186	21	14	35	<0.001
Mean ± SD	21 ± 2	10 ± 3	39 ± 6	

The Cosinor results for intraocular pressure measurements by animal. The 24-hour mean, the full range (max to min), rhythmicity (r^2 times 100%), and P-value of the cosine fit are shown. All eight animals had a significant intraocular pressure rhythm. Mean ± SD values are for eight animals with a significant IOP rhythm.

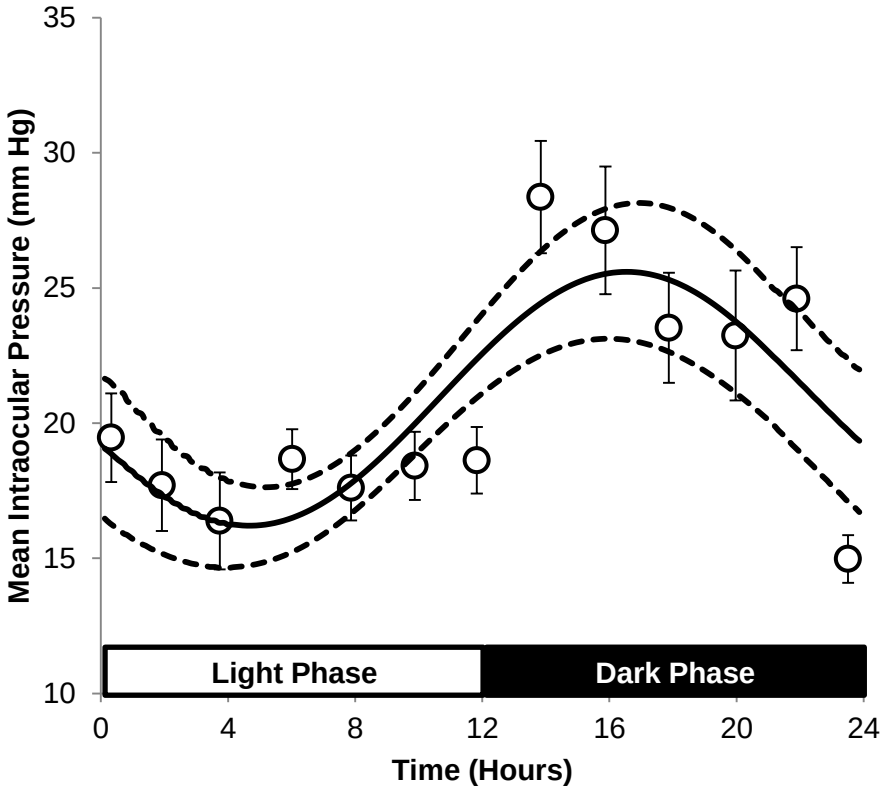

Figure 4.1: Mean intraocular pressure in 8 normal adult Brown Norway rats housed in standard light-dark conditions.

Mean intraocular pressure peaked near the middle of the dark-phase. Plots show the mean IOP and standard error (open circles), as well as the cosine fit through the data (solid red line), and the 95% confidence interval (dashed lines).

Table 4.2: Cosine Fit Parameters for Mean Arterial Pressure

ID	Mean	Range	Rhythmicity	P-value
BN132	105	6	2	0.37
BN134	92	34	53	< .001
BN144	88	21	16	< .001
BN148	103	21	23	< .001
BN180	104	9	3	0.17
BN182	96	14	10	< .001
BN184	101	21	19	< .001
BN186	103	14	7	0.02
Mean ± SD	97 ± 6	21 ± 7	21 ± 16	

The Cosinor results for mean arterial pressure measurements by animal. The 24-hour mean, the full range (max to min), rhythmicity (r^2 times 100%), and P-value of the cosine fit are shown. Two out of eight animals (BN132 and BN180) did not show a significant blood pressure rhythm. Mean ± SD values are for six animals with a significant blood pressure rhythm.

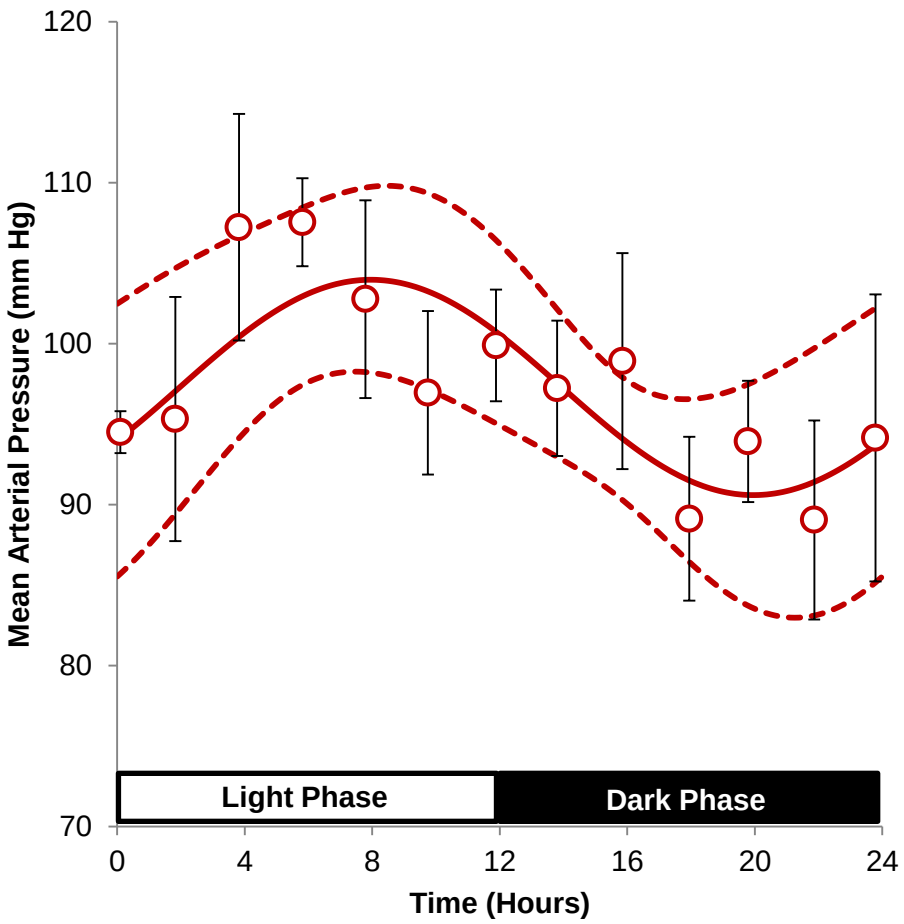

Figure 4.2: Mean Arterial Pressure for six normal Brown Norway rats that have a circadian rhythm when housed in a standard light-dark condition.

This diurnal rhythm showed that peak mean arterial pressure occurred during the light phase. Plots show the mean arterial pressure and standard error (open circles), as well as the cosine fit through the data (solid red line), and the 95% confidence interval (dashed lines).

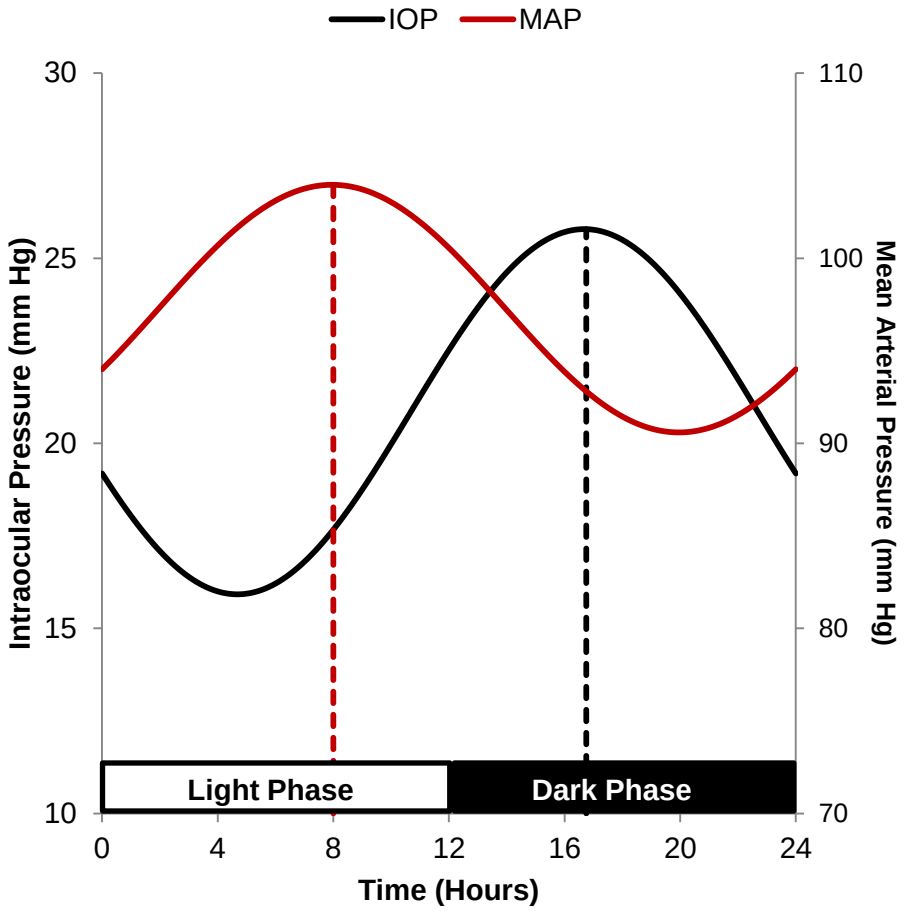

Figure 4.3: Phase relationship between intraocular pressure (IOP) and mean arterial pressure (MAP) in six normal adult Brown Norway rats housed in standard light-dark conditions.

The black dash line indicates that, on average, the maximum IOP occurred 4.6 hours after the lights turned off. The red dashed line indicates that, on average, the maximum MAP occurred 4.0 hours before the lights turned off.

4.6 Discussion

Significant time-dependent changes in both IOP (n = 8 animals) and mean arterial pressure (n = 6 animals) were detected in adult Brown Norway rats. IOP peaked during the dark phase (time = 16.6 Zeitgeber Time), while mean arterial pressure peaked during the light phase (time = 8.0 Zeitgeber Time). The diurnal IOP variation results in these animals (mean range of IOP measurements = 10 ± 3 mm Hg) were similar to the results reported in Chapter Three. The results from that study showed that IOP in the standard light-dark condition peaked near the middle of the dark phase (16.6 ± 1.2 Zeitgeber Time; 95% CI: 15.8 to 17.4) and that the mean range of IOP measurements was 14 ± 3 mm Hg (95% CI: 10 – 18 mm Hg).

Blood pressure was at a maximum during the animal's rest period (e.g. light phase) and at a minimum during the animal's active period (e.g. dark phase), and these results are counterintuitive. Circadian blood pressure variations are generally related to daily activities. Therefore, blood pressure would be expected to peak during the animal's active period and then decrease during the resting phase.[178, 179] Rats are nocturnal animals displaying highest activity during the dark-phase, and we might therefore expect peak blood pressure to occur during the dark phase.[180] Telemetric blood pressure measurements in both mice and rats have conflictingly reported peak blood pressure to coincide with the animal's active or dark phase.[178, 179, 181, 182] The discrepancy between studies may be related to the way blood pressure was measured (tail cuff system vs. telemetric devices). However, blood pressure measurements acquired with telemetric or tail cuff systems are deemed comparable in normotensive rats and not in spontaneous hypertensive rats.[182] For example, Irvine and colleagues showed that spontaneous hypertensive rats had a higher heart rate and blood pressure when measured with the tail cuff system than with the telemetric. A limitation of studies that compared the tail cuff system and telemetric systems is that they only acquired one measurement during the

day. This is very different from our current study where we measured blood pressure 12 times over the course of 24 hours. These many measurements may have stressed the animal and, while measurements were still valid, the measurements may have been influenced by the experimental design. For example, some studies report that blood pressure is higher when rats are restrained or warmed up during the measurement procedure.[182, 183] However, this would simply imply that our diurnal blood pressure curve is biased upward and warming/restraining the animal cannot account for the shift in the time when blood pressure peaked. In this study, the first blood pressure measurements were acquired during the light phase and this may have caused blood pressure to peak during these early time points. This limitation could be addressed by conducting another circadian rhythm study where measurements are first acquired during the dark-phase, instead of the light-phase, and determining the time when blood pressure peaks. Lastly, the 9 hour phase lag between IOP and blood pressure likely puts the optic nerve head at risk for reduced vascular supply at night when blood pressure is at a minimum and IOP is at a maximum. Hypothetically, in an animal model of glaucoma, this would create the perfect storm for damage and should be further investigated.

Chapter Five

Quantitative Evaluation of Factors Influencing the Repeatability of SD-OCT Thickness Measurements in the Rat

Accepted for publication in Investigative Ophthalmology and Visual Science 2012

Citation: Lozano DC and Twa MD. Quantitative evaluation of factors influencing the repeatability of SD-OCT thickness measurements in the rat. *Invest Ophthalmol Vis Sci*. 2012; 53 (13): 8378–8385

5.1 Preface

In this chapter, the repeatability and reproducibility of thickness measurements were quantified from *in vivo* spectral domain optical coherence tomography images from adult rat eyes. The effects of realignment techniques and image quality on measurement of retinal thickness were also evaluated from optical coherence tomographic images of rat and human eyes. Repeatable retinal thickness measurements from SD-OCT in the rat were acquired by combining manual and automated realignment procedures. These results are encouraging because they suggest that the realignment techniques are robust and can be implemented to quantify disease progression in experimental rat models of glaucoma.

5.2 Abstract

Purpose: To quantify repeatability and reproducibility of thickness measurements and the effects of realignment and image quality on measurements of retinal thickness from optical coherence tomographic (OCT) imaging in the rat eye.

Methods: Retinal imaging was performed in 16 Brown Norway rats (n=16 eyes; $\bar{x}$ = 372 g). Precision metrics: 95% limits of agreement (LoA), intraclass correlation coefficient (ICC) and the coefficient of variation (CV), were calculated using manual and combined manual+automated realignment procedures for nerve fiber and retinal ganglion cell layer (NFL/GCL), NFL/GCL and inner plexiform layer (NFL/GCL+IPL), and total retinal thicknesses (excluding blood vessels). The influence of image quality on NFL thickness measurement was assessed by comparing high and low quality image data (real and simulated) from the rat, as well as clinical data.

Results: Mean NFL/GCL thickness was 26 ± 3µm, NFL/GCL+IPL thickness was 70 ± 3 µm, and total retinal thickness was 192 ± 7µm. Thickness difference between imaging sessions for NFL/GCL was 1µm (95% LoA: –4 to 3 µm; ICC = 0.82; CV = 4.7%), for NFL/GCL+IPL was 0 µm (95% LoA: –4 to 4 µm; ICC = 0.88; CV = 1.4%), and total retinal thickness was 1 µm (95% LoA: –3 to 4 µm; ICC = 0.97; CV = 0.7%). Thickness differences were similar between realignment procedures (NFL/GCL: *P* = .43; NFL/GCL+IPL: *P* = .33; total retina: *P* = .62). Although NFL thickness measurements increased slightly in low quality rat images (4 µm; *P* = .04), this was not true with clinical images (1.4 µm; *P* = .36).

Conclusion: Precision of retinal layer thickness estimation from OCT imaging is excellent when manual and automated realignment procedures are combined, but may still be influenced by image quality and segmentation methods.

5.3 Introduction

Since it was first described in 1991, optical coherence tomography (OCT) imaging technology has evolved rapidly and has become one of the most important clinical imaging tools available.[184] Current clinical SD-OCT systems have sufficient speed and resolution that they have been successfully adapted for *in vivo* imaging in animal models of ocular disease, including a rat model of glaucoma[116] and genetic retinal degenerations in mice.[185, 186] A benefit of adapting commercial clinical OCT imaging systems for use with these animal models is the ability to perform longitudinal studies through high-resolution *in vivo* ocular imaging without the need or expense to develop custom instrumentation. While this capability will further encourage the use of OCT imaging as a tool for ocular disease research, the utility of OCT imaging in animal models of ocular disease will be determined in part by the system's resolution and sensitivity for detecting structural changes.

Precision of retinal thickness measurements from OCT data is influenced by factors that vary both within and between imaging sessions, including factors related to the examiner (e.g., alignment, stability, focus, etc.), the subject (e.g., motion, optical clarity, etc.), image hardware (e.g., acquisition speed, resolution), and post-acquisition image processing routines (e.g., registration, segmentation, etc.). Despite these potential limitations, excellent repeatability of OCT thickness measurements has been reported in humans.[106-115, 187] There are a number of additional unique considerations for achieving repeatable scan-path alignment with non-fixating anesthetized animal subjects that can further influence reproducibility studies in the rodent eye.[116] Previous studies reporting reproducibility of retinal thickness from OCT imaging limit analysis to only a few of the factors listed above and generally do not account for the influence of image quality on measurement precision. The purpose of this study was to quantify the effects of ocular–instrument realignment and image quality on measurements of retinal thickness from

OCT imaging in the rat eye. The precision of retinal thickness measurements between and within imaging sessions was determined using a commercial OCT instrument with a manual and a combined manual + automated realignment procedure designed to account for scan location and ocular rotational orientation.

5.4 Methods

All experimental and animal care procedures were approved by the Institutional Animal Care and Use Committee of the University of Houston and were in accordance with the ARVO Statement for the Use of Animals in Ophthalmic and Vision Research. Sixteen healthy 8-month old male Brown Norway rats (n = 16 eyes) were included in this study. Rats were anesthetized with an intraperitoneal injection of ketamine (Vedco, St. Joseph, MO; 50mg/kg) and xylazine (Vedco, St. Joseph, MO; 5 mg/kg). Pupils were dilated using a topically applied drop of tropicamide (Bausch and Lomb, Inc., Tampa, FL; 0.5%).

5.4.1 Image Acquisition

Scanning laser ophthalmoscopic (SLO) fundus images and single horizontal OCT line scans were simultaneously captured using the Spectralis HRA+OCT system (Heidelberg Engineering, Heidelberg, Germany, Acquisition Module Version 5.4.7). Images were acquired at a scan speed of 40,000 A-scans per second using a super luminescent diode light source with a central wavelength of 870 nm and nominal axial resolution of 4 µm. A 30° line scan image comprised of 1536 A-scans per B-scan and at least 51 averaged frames were acquired. Repeatability was evaluated at several different retinal locations ranging from 0.3 to 1.1 mm away from the optic nerve head center in the superior and inferior retina; however, a single line scan position was evaluated for each eye. A scaled schematic illustration of the rat retina and line-scan locations is shown in **Figure 5.1**. All images had an image quality greater than 25 dB

(mean image quality value: 37 ± 3). The manufacturer considers image quality values greater than 25 dB to be *good;* image quality ranges from 0 dB (poor) to 40 dB (excellent).

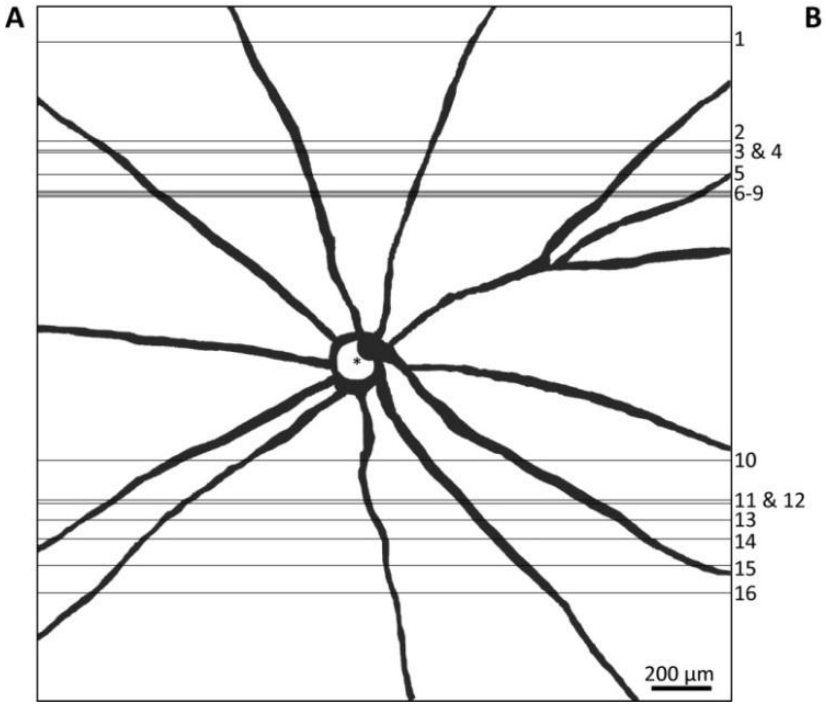

B

Location	NFL/GCL	NFL/GCL+IPL	Total Retina
1	19 ± 4	65 ± 5	202 ± 5
2	28 ± 4	73 ± 5	192 ± 7
3	28 ± 3	66 ± 8	184 ± 7
4	24 ± 3	69 ± 5	191 ± 6
5	25 ± 3	70 ± 4	189 ± 5
6	24 ± 4	66 ± 5	195 ± 7
7	28 ± 4	75 ± 5	191 ± 4
8	22 ± 4	69 ± 5	193 ± 6
9	27 ± 3	69 ± 4	187 ± 5
10	25 ± 5	70 ± 7	201 ± 7
11	27 ± 4	71 ± 6	190 ± 5
12	29 ± 3	78 ± 8	205 ± 8
13	29 ± 6	73 ± 7	194 ± 8
14	26 ± 2	71 ± 6	196 ± 9
15	28 ± 3	68 ± 6	177 ± 4
16	26 ± 8	68 ± 5	188 ± 4
Average	26 ± 3	70 ± 3	192 ± 7

Figure 5.1: Scaled schematic illustration of the rat retina along with SD-OCT scan line locations.

(A) Horizontal lines (labels 1-16) indicate the location where each OCT B-scan image was acquired and repeatability assessed. The optic nerve head center is marked by the asterisk and the radial lines represent blood vessels. Scale bar represents 200 µm. **(B)** Baseline retinal layer thickness measurements (mean ± SD) for each scan location. Layers evaluated included: nerve fiber layer and ganglion cell layer (NFL/GCL), NFL/GCL and inner plexiform layer (NFL/GCL + IPL), and total retina.

Adapting this commercial SLO/SD-OCT imaging system for use in the rat eye required several modifications to account for the shorter axial length and optical characteristics of the rat eye. The modifications for this study included adjustments to the spectrometer reference arm length, image scaling to correct for image lateral magnification, and compensation for some higher and lower order optical aberrations of the eye. The position of the reference arm was adjusted using the available OCT system software and no additional optics were added to the imaging system to compensate for the shorter axial length of the rat eye. The optical power of the rat eye is approximately 5 times greater than the human eye, producing much greater image lateral magnification.[119, 188] Image lateral magnification was corrected by calculating an average conversion factor (1.39 µm/pixel) using a three-surface schematic eye derived from ultrasonic measurements of axial length (n=10 eyes; data not shown) and from published indices of refraction.[117, 119] Finally, a +3.50 D contact lens, with a 3.31 mm base curvature and 6.5 mm overall diameter, was placed on the eyes to preserve corneal hydration and to compensate for some optical aberrations of the eye.

Using a pre-alignment procedure, eyes were aligned perpendicular to the OCT scan path with a six-axis positioning stage and bite bar.[189] This stage consists of a platform for rotation along the y-axis (vertical), and two stage goniometers for rotation along the x (horizontal) and z- axes (imaging axis). Linear translation stages were used for fine positioning along the x, y, and z-axes. Next, the SLO image was optimized by making fine adjustments to the stage and camera position until there was minimal vignetting of the SLO image and the optic nerve head was located in the center of the image. Camera focus and spectrometer reference arm settings were adjusted until the best image contrast was achieved at the depth of the nerve fiber layer and there was even illumination and contrast across the entire SLO. OCT B-scans were acquired after

final adjustments were made to minimize any residual vertical or horizontal tilt to the OCT image.

The OCT reference arm setting, camera focus, and positioning stage settings (translation and rotation) were recorded and were used to realign the rat eye during the follow-up imaging sessions. At the end of the first imaging session, the baseline SLO image and its corresponding OCT scan location were printed on transparencies to facilitate realignment during follow-up imaging sessions.

Two realignment procedures were evaluated: manual realignment and a combined manual + automated realignment procedure. The manual realignment procedure began with physical positioning of the animal and eye as described above in the pre-alignment procedures. The OCT reference arm and OCT camera focus were also set to the baseline imaging session values. Next, the SLO transparency was placed on top of the live SLO fundus image and the positioning stage further adjusted until the size and location of the retinal blood vessels and optic nerve head matched the baseline SLO image by visual inspection. Finally, the OCT scan line location was positioned at the baseline scan position; any residual vertical tilt in the OCT scan was minimized and the image was acquired. This re-alignment procedure was a balance between optimizing the SLO and OCT alignment and image contrast. In some cases, the optimized OCT image had some slight residual tilt. In these instances, the image was flattened using post-hoc image processing to shift all A-scans until the OCT was leveled relative to the RPE. The combined manual + automated realignment procedure began with the manual realignment procedure described above and further included use of the instrument's built-in automated realignment procedure (follow-up mode). The instrument and the animal were not repositioned between the manual and automated realignment procedures. Automated realignment alone (without manual realignment) was not

sufficient because the length of time required for gross positioning and final realignment could exceed the instrument's maximum permitted scan duration of 5 minutes.

The reproducibility of retinal thickness measurements between imaging session for each realignment method was calculated from two images acquired during two different imaging sessions separated by an average of 10 ± 4 days. Within session repeatability using the manual alignment procedure was calculated from thickness measurements of two images captured within a single imaging session, without adjusting the animal, OCT system, or repositioning the stage settings.

5.4.2 Quantifying Manual Realignment Precision

Raw image data were extracted from the binary output files and segmented for quantitative analysis with a customized Matlab program (2011b, The MathWorks, Natick, MA). The precision of OCT scan line placement was quantified from scan line position within the SLO fundus images. The follow-up SLO image was registered to the baseline SLO image using an affine transformation.[190] The distance and angle between scan positions was calculated and used to quantify the precision of OCT scan line placement within imaging sessions and between imaging sessions using the manual realignment procedure. **Figure 5.2** shows how the slope of the baseline and follow-up scans were used to calculate the angle between these two OCT scan lines. Small rotational and translational parameters translate to better agreement in scan placement between images. It was not possible to quantify the precision of scan line placement using the automated realignment procedure because image registration transformation parameters used by the OCT system software are not accessible.

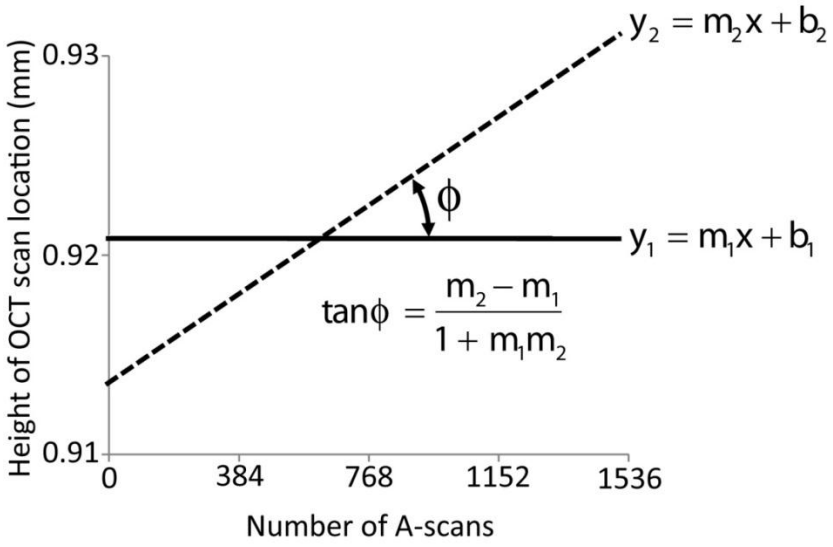

Figure 5.2: Method to determine the precision of SD-OCT scan line placement for repeated imaging.

The precision of OCT scan line placement was quantified from scan line position within the SLO fundus image. The follow-up SLO image was registered with the baseline SLO image. The B-scan locations between images were then extracted from the registered SLO images and plotted against the baseline scan location. The x-axis represents the individual A-scan number (pixel column) in each OCT B-scan image; the y-axis is the scan location within the SLO retinal image relative to the optic nerve head center. The solid (y_1) and dashed (y_2) lines represent the locations of the OCT B-scans during the first and second imaging sessions. The slopes of these lines were used to calculate the angle between the two lines. An angle close to zero suggests minimal differences in retinal location between the two imaging sessions.

5.4.3 Thickness Measurement Precision

A customized segmentation protocol was developed to automatically delineate the nerve fiber layer/ganglion cell layer (NFL/GCL), while the inner plexiform layer (IPL) and retinal pigmented epithelium (RPE) were manually segmented. **Figure 5.3** shows a comparison between OCT and histologic retinal layers of the rat eye. This figure illustrates that the innermost layer of the rat retina is composed of the retinal ganglion cell axons along with their cell bodies and displaced amacrine cells.[49] This corresponds with a prominent hyper-reflective layer in the inner-most region of the OCT image, followed by the less reflective IPL. The RPE is one of the last hyper-reflective signals of the outer retina in the OCT image, deep to the photoreceptors and before the structured choroid and hyper reflective sclera.[191] Automated segmentation was performed using a Canny edge detection algorithm (Gaussian filter size of $\sqrt{2}$). Intensity peaks were detected in the filtered image that corresponded to the boundary of the layers of interest. NFL/GCL thickness was defined as the distance between the inner limiting membrane (ILM) and outer boundary of the combined nerve fiber layer and ganglion cell layer. The NFL/GCL + IPL was defined as the distance from the ILM to the outer boundary of the IPL. Total retinal thickness was defined as the distance from the ILM to the RPE (**Figure 5.3**). Mean NFL/GCL, NFL/GCL + IPL, and total retinal thicknesses were calculated for each OCT image (excluding blood vessel regions).

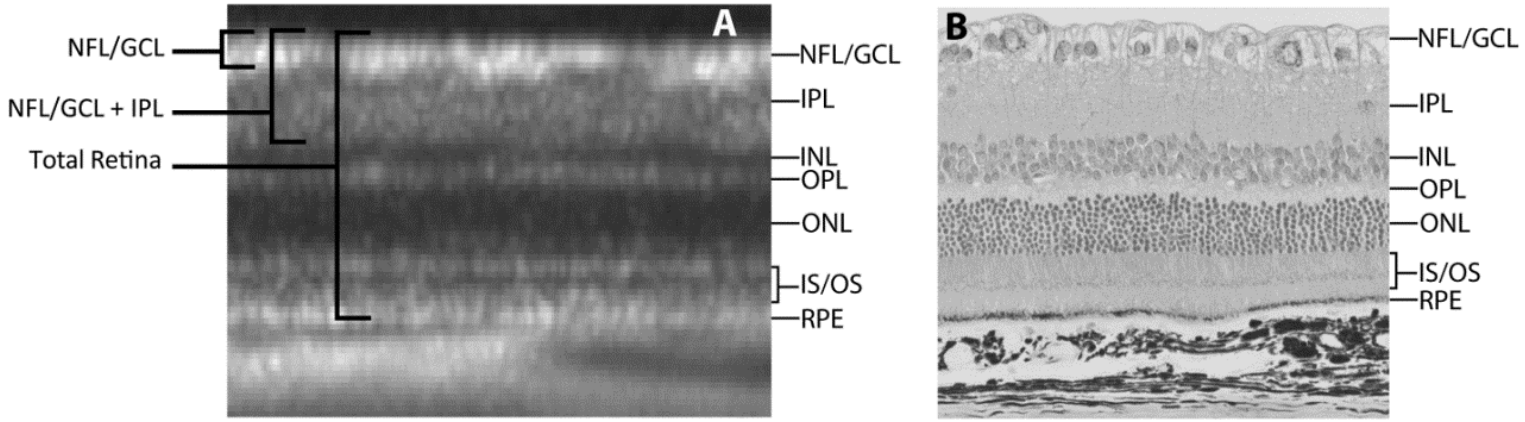

Figure 5.3: Comparison of rat retinal cross section by OCT and histology.

(A) Close up of OCT rat retinal image indicating the various retinal layers as well as how thickness measurements were made for the repeatability study. NFL/GCL: Nerve fiber layer and retinal ganglion cell layer; IPL: Inner plexiform layer; INL: Inner nuclear layer; OPL: Outer plexiform layer; ONL: Outer nuclear layer; IS/OS: Inner and outer segments; RPE: Retinal pigmeted epithelium. **(B)** Histological image of the rat retina showing the various retinal layers and their correspondence with the OCT image.

5.4.4 Influence of Image Quality on Thickness

The impact of image quality on measurements of NFL/GCL thickness was evaluated by three methods. In the first method, NFL/GCL thickness was measured from simulated models of OCT images with varying degrees of image quality. These simulated models were generated by adding speckle noise to 5 reference OCT images (image quality = 37 ± 5 dB). Speckle noise is an inherent part of OCT images and results from backscattered light from multiple scatter points. Noise was modeled using a multiplicative approach ($I_n = I_o + I_o \times N$) where I_o is the original image, I_n is the noisy image, and N is random noise with zero mean and user specified variance to generate a range of signal-to-noise ratios between 15 to 30 dB (in increments of 5 dB). Signal-to-noise ratio was defined as $10 \times \log(P_o/P_n)$, where P_o is the original image power and P_n is the power of the image with added noise. The mean change in NFL/GCL thickness was calculated as a function of decreasing signal-to-noise ratio. Image quality in the OCT system, is calculated as $10 \times \log(S/N)$, where S is the maximum image intensity amplitude and N is the maximum noise intensity amplitude. This is a conventional definition of signal-to-noise ratio used in physical optics. **Figure 5.4** illustrates image quality over a range of signal-to-noise ratios. Statistical analysis was performed from thickness measurements taken across the entire OCT image at each signal-to-noise ratio (**Figure 5.4B**). The second evaluation of image quality on NFL/GCL thickness measurements was performed with a paired sample (n = 8 eyes; 16 images) of real images from normal adult rats that had high and low quality scans (**Figure 5.4C** and **5.4D**). A third evaluation of the effects of image quality on NFL thickness measurements was performed with clinical images from normal human subjects (**Figure 5.4E** and **5.4F**). All scans (12-degree circular scan pattern) were manually positioned on the optic nerve head center by a single examiner within an imaging session. A convenience sample

(paired data; n = 26 images from 13 eyes) of high quality (≥ 25 dB) and low quality (< 25 dB) scans were segmented using the native Spectralis system software and nerve fiber layer thickness was compared between the two groups.

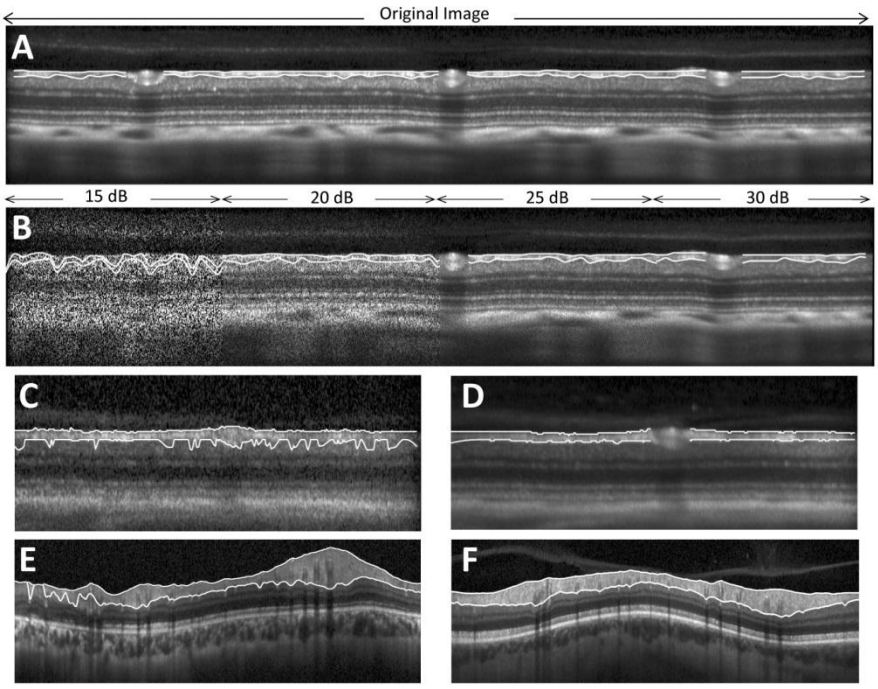

Figure 5.4: The effect of image quality on nerve fiber layer/ retinal ganglion cell layer segmentation.

(A) Original reference OCT image; The combined nerve fiber layer and ganglion cell layer (NFL/GCL) is delineated by white lines. For illustrative purposes here, the original reference OCT image was divided into four regions (indicated by the arrows above B). **(B)** Images were degraded by adding speckle noise across the entire image to yield signal-to-noise ratios ranging from 15 to 30 dB. **(C)** NFL/GCL segmentation of a real rat image with an image quality of 19 dB. Segmentation errors were prominent in low quality images (less than 25 dB). Automatic blood vessel localization was more difficult to discern in low quality images. **(D)** NFL/GCL segmentation of a real rat scan with image quality of 39 dB where blood vessels were successfully located and excluded from thickness analysis. **(E)** NFL segmentation errors in human eyes using the native Spectralis segmentation routines were also prominent in circular scans with an image quality of 19 dB. **(F)** NFL segmentation of a circular scan of a human eye that had an image quality of 32 dB.

5.4.5 Statistical analysis

Mean NFL/GCL, NFL/GCL + IPL and total retinal thicknesses were calculated within imaging sessions and between imaging sessions. The measures of precision that were assessed included: the difference in thickness measurements between imaging sessions and within imaging sessions, as well as, the 95% limits of agreement (LoA), intraclass correlation coefficients (ICC) and coefficient of variation (CV).[192] Statistical comparison of mean thicknesses between (for both manual and the combined manual + automated realignment procedures) and within imaging sessions (manual alignment) were assessed using paired t-test. The methods described by Shrout and Fleiss (1979) were used to calculate the appropriate ICC, for assessing precision of a single rater (the OCT) performing multiple measurements (averaged) from a random sample of animals.[193] Wolf- Schnurrbusch's method was used to calculate the coefficient of variation (*equation 1*).[114] In equation 1, x_i and x_j are thickness measurements from the first and second imaging session, respectively, and n is the number of eyes included in the study.

$$CV = \frac{\sqrt{\frac{\sum (x_i - x_j)^2}{2 \times n}}}{\frac{\sum x_i}{n}} \times 100\% \qquad (1)$$

Dunnett's test (multiple comparisons to a single reference standard) was used to compare NFL/GCL thickness values between the original reference OCT image (**Figure 5.4A**) against the images with added noise (**Figure 5.4B**). A paired t-test was used to compare mean NFL/GCL thickness between high and low quality images from rat eyes, as well as for comparing NFL thickness for the clinical human images.

5.5 Results

5.5.1 Quantifying Manual Realignment Precision

The mean and standard deviation of the residual distance and angle between scan locations captured between two imaging sessions was 5 ± 10 µm and 0.34 ± 0.59° (rotation). **Figure 5.5A** illustrates the follow-up image aligned and superimposed on top of the baseline SLO image for one animal. The checkerboard pattern at the bottom and left margins of the SLO images highlight the non-overlapping regions of the two SLO images and **Figure 5.5A** also shows that the residual difference in scan location for this particular animal and between these two images was 0 µm. Similar analysis was conducted from SLO images captured within imaging sessions, and the residual difference in scan position was 1 ± 0.4 µm and the averaged angle between these two lines was 0.04 ± 0.03°.

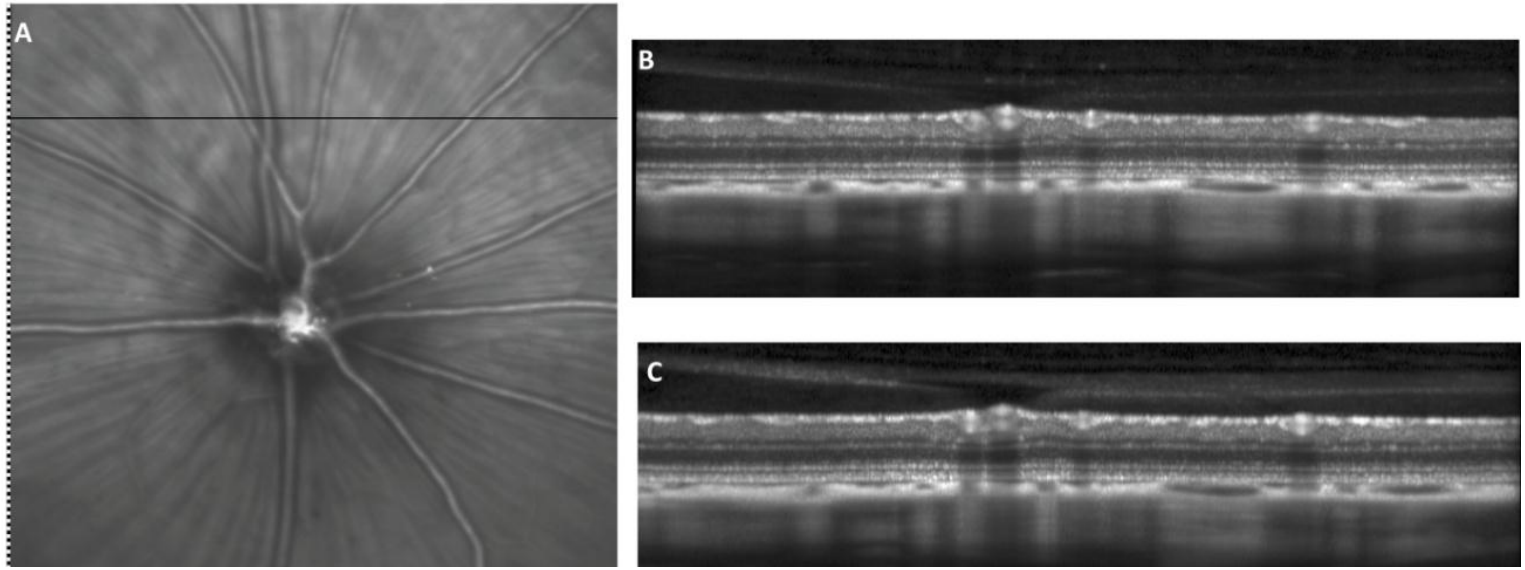

Figure 5. 5: Illustration of scanning laser ophthalmoscope (SLO) and OCT repeatability in the rat eye.

Retinal fundus images and their associated OCT images are shown for one animal captured at two different time points. **(A)** SLO retinal fundus image captured during the second imaging session was registered and superimposed on the baseline SLO retinal fundus image. The residual difference between the baseline and follow-up scan locations was 0 µm for this particular animal. Checkerboard pattern highlights the non-overlapping regions of the baseline and repeated SLO images. The horizontal line represents the OCT b-scan position. **(B)** Baseline OCT image. **(C)** OCT image captured during the second imaging session with the manual realignment procedure.

5.5.2 Thickness Measurement Precision

Baseline NFL/GCL thickness (mean ± SD) was 26 ± 3 μm, while mean NFL/GCL+IPL was 70 ± 3 μm, and total retinal thickness was 192 ± 7 μm. There was no significant difference between these baseline and follow-up measurements using the manual realignment procedure: NFL/GCL (26 ± 3; *P* = .24), NFL/GCL + IPL (70 ± 4; *P* = .81), and total retinal thickness (192 ± 7; *P* = .18).

The limits of agreement for measurements of retinal thickness *between* imaging sessions using the manual realignment procedure are shown in **Figure 5.6** for NFL/GCL, NFL/GCL + IPL, and total retinal thickness. These plots demonstrate that the thickness difference is close to zero and that the limits of agreement are between –4 and 4 μm or better for all measurements. Intraclass correlation coefficients between imaging sessions with the manual realignment were all greater than 0.82 (**Table 5.1**). The coefficients of variation were below 4.7% for all thickness measurements.

The mean difference and limits of agreement for measurements of retinal thickness *within* an imaging session using the manual realignment procedure are also shown in **Figure 5.6**. There was no significant difference in NFL/GCL (25 ± 2; *P* = .33), NFL/GCL + IPL (70 ± 5; *P* = .11) or total retinal thickness (192 ± 8; *P* = .75) measured from two images captured within the same imaging session. Over all of the retinal layers considered, the widest calculated limits of agreement observed within an imaging session (–3 to 3 μm: total retina) were similar to the widest limits of agreement between imaging sessions (–4 to 4 μm: NFL/GCL+IPL). In summary, there were no significant differences in retinal thickness measurements when comparing within and between imaging sessions with manual realignment: NFL/GCL (*P* = .52), NFL/GCL + IPL (*P* = .33), and total retinal thickness (*P* = .22).

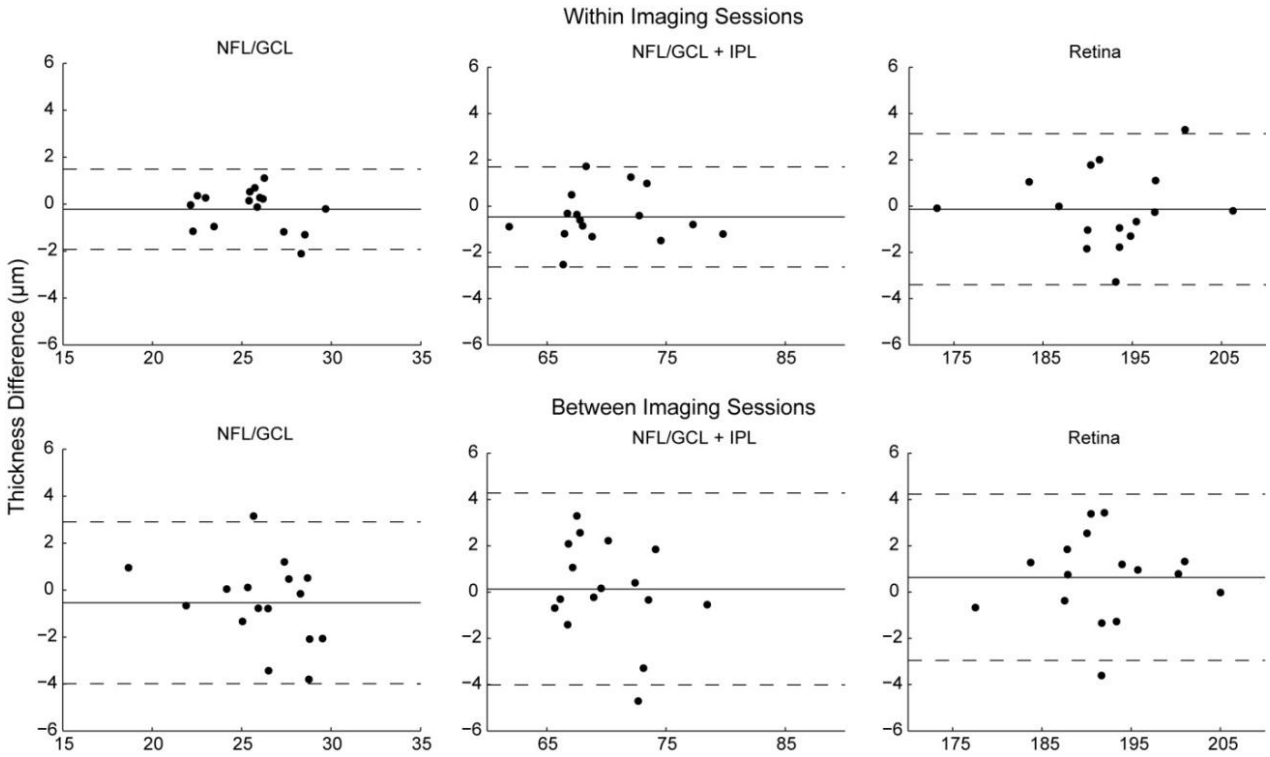

Figure 5.6: Precision of thickness measurements taken within and between imaging session with manual realignment. Residual difference in measured thickness is plotted versus mean thickness. Each point represents the difference in mean thickness calculated for each animal. Mean difference is indicated by the solid line and the upper and lower 95% limits of agreement are indicated by dashed lines. NFL/GCL: Nerve fiber layer and retinal ganglion cell layer, NFL/GCL + IPL: Nerve fiber layer and retinal ganglion cell layer plus inner plexiform layer, and total retinal thicknesses withing and between imaging sessions for all subjects.

Table 5.1: Precision metrics for retinal OCT Thickness measurements in the normal Brown Norway rat. NFL/GCL: Nerve fiber layer and retinal ganglion cell layer; NFL/GCL + IPL: Nerve fiber layer and retinal ganglion cell layer plus inner plexiform layer; ICC: intraclass correlation coefficients; CV: Coefficient of variation. The 95% limits of agreement were not significantly different between manual and combined (manual + automated) realignment procedures.

	Mean Difference (µm)	**95% Limits of Agreement (µm)**	**ICC**	**CV**
Between Session				
Manual Realignment				
NFL/GCL	1	–4 to 3	0.82	4.70%
NFL/GCL + IPL	0	–4 to 4	0.88	1.40%
Total Retina	1	–3 to 4	0.97	0.70%
Manual + Automated Realignment				
NFL/GCL	0	–3 to 4	0.98	4.20%
NFL/GCL + IPL	0	–3 to 4	0.95	3.30%
Total Retina	2	–2 to 6	0.98	1.00%
Within Session				
NFL/GCL	0	–2 to 2	0.97	2.40%
NFL/GCL + IPL	1	–3 to 2	0.99	1.20%
Total Retina	0	–3 to 3	0.99	0.60%

Using the combined manual + automated realignment procedure, the mean difference in NFL/GCL thickness was 0 µm (95% LoA: –3 µm to 4 µm). The mean difference for the NFL/GCL + IPL was 0 µm and the 95% LoA were –3 to 4 µm. The mean difference for total retinal thickness was 2 µm and the 95% LoA were –2 to 6 µm. The mean differences calculated between imaging session with the combined manual + automated realignment procedures were not statistically different from those calculated with the manual realignment procedure alone: NFL/GCL (*P* = .38), NFL/GCL + IPL (*P* = .27), and total retina (*P* = .10).

5.5.3 Influence of Image Quality on Thickness

Using simulated data, NFL/GCL thickness measurements increased as image quality was degraded. In the 5 high-quality reference images (SNR= 37 ± 5 dB), NFL/GCL thickness ranged between 20 to 26 µm. In the degraded images, NFL/GCL thickness at the lowest SNR was, on average, 2 ± 2 µm thicker than at the highest SNR. On average, NFL/GCL thickness increased by 1.3 µm per 10 dB decrease in signal-to-noise ratio.

The NFL/GCL thickness for real rat images with high quality (31 ± 5 dB) was 30 µm (95% CI = 22 to 39 µm) and 34 µm (95% CI: 27 to 41 µm) for low quality images (22 ± 2 dB). The 4 µm increase in thickness between high and low quality images was statistically significant (*P* = .04). The NFL thickness measurements for high quality (30 ± 4 dB) clinical images in human eyes was 99 µm (95% CI= 95 to 103 µm). The NFL thickness measurements for low quality (22 ± 2 dB) clinical images in human eyes was 101 µm (95% CI= 97 to 104 µm). These differences were not statistically significant (1.4 ± 5.3 µm; *P* =.36).

5.6 Discussion

The purpose of this study was to analyze factors that influence repeatability of SD-OCT thickness measurements in the rat. Ocular and instrument realignment was the first factor analyzed. The mean differences in retinal thickness measurements between and within imaging sessions were less than 2 µm and the 95% limits of agreement were within –4 µm to 6 µm, near the axial resolution of the OCT system (4 µm). Thickness measurements from the manual realignment procedure were not significantly different from the combined manual + automated realignment procedure. Fortune and colleagues[194] similarly reported that manual and the Spectralis built-in automated realignment procedures yielded comparable thickness results. However, they did not provide details about the realignment procedures used to quantify the similarity in thickness measurements that were reported. While there may be advantages to using the automated realignment procedure, it cannot be used alone in non-fixating anesthetized animal subjects without some pre-alignment procedure. In some cases, the length of time required for gross positioning and final realignment can exceed the instrument's maximum permitted scan duration of 5 minutes. Both realignment methods evaluated in this study performed well and did not contribute significant variability to retinal thickness measurements between imaging sessions.

In vivo measurements of NFL/GCL, NFL/GCL + IPL, and total retinal thicknesses have been reported in several studies. Nagata and colleagues[195] reported a NFL/GCL thickness of 27.9 ± 1.8 µm at a location 500 µm away from the optic nerve head center. These measurements agree with those reported in this study (26 ± 3 µm) that were collected at an average distance of 617 µm away from the optic nerve head center. NFL/GCL + IPL thickness measurements in the current study are thinner (70 ± 4 µm) than the measurements reported by Guo et al.[116](84.87 µm) who also used the Spectralis (Heidelberg Engineering) but made their measurements closer to the optic

nerve head center (~300 µm) and used a different rat strain (Dark Agouti). Srinivasan and colleagues used a custom built spectral domain OCT system to measure total retinal thickness in Long-Evans rats. They generated thickness maps over a 2.6 mm^2 region and reported a mean total retinal thickness of 189.3 µm. Total retinal thickness measurements in the current study were thicker (192 ± 7 µm) than those reported by Guo et al.[116] (172.19 ± 5.17 µm) and Srinivasan et al.[196] Total retinal thickness in this study was defined as the distance from the internal limiting membrane to the RPE, whereas the previous two studies[116, 196] defined retinal thickness as the distance from the NFL/GCL to the outer segments of photoreceptors. There is disagreement about how to assign anatomical correspondence between histology and OCT imaging.[197-199] This is especially true in the outer retina where distinctions between RPE and photoreceptor outer segments have similar contrast. This disagreement might account for some of the differences in retinal thickness reported between studies.

The ability to scan the same retinal location between imaging sessions was quantified by registering the follow-up SLO image with its corresponding baseline SLO image and measuring the distance between scan locations. The average residual difference between scan locations was 5 µm. NFL/GCL measurements were made at 0.3 to 1.1 mm away from the optic nerve head center in 11 Brown Norway rats and were used to calculate the average rate of change in NF/GCL thickness. NFL/GCL decreased by 18 µm/mm, and this translated to a 0.09 µm difference in NFL/GCL thickness when scan locations are separated by 5 µm. These results show that a small portion (less than a micron thickness difference) of the calculated thickness difference is attributable to the variability in scan location between imaging sessions with the manual realignment procedure. The image registration and transformation parameters used in the automated realignment procedure are proprietary and limited the ability to evaluate the precision of scan line placement and its contribution to the observed variations in retinal thickness in

the combined manual + automated realignment procedure. Nevertheless, it was still possible to quantify the repeatability of retinal thickness measurements with the manual + automated realignment procedure. We found that they were not significantly different from thickness measurements made from images captured with the manual realignment procedure alone.

Gabriele and colleagues[200] collected volumetric data with a different spectral domain-OCT system (Bioptigen, Inc., Durham, NC) and measured total retinal thickness in the C57Bl/6 mouse. Their global coefficient of variation for total retinal thickness was greater (1.6%) than the CV calculated in the current study (0.7%). This may be due, in part, to the fact that the authors used mice which have thinner retinas (178 µm) than the rat. The authors also did not account for out-of-plane rotational alignment in their analysis. They performed post-acquisition image realignment, which cannot account for variations in the OCT beam angle that can influence thickness measurements. In this study, a positioning stage was used to systematically control the amount of rotation, and translation used during an imaging session. Also, the vertical and horizontal scan alignment was checked before image capture to insure that the scan beam was as normal to the retinal surface as possible. This positioning technique minimized the variation in OCT beam angle and maximized the ability to repeatedly scan the same retinal location both within and between imaging sessions.

The native segmentation routines of the Spectralis failed to automatically segment the layers of the rat retina. We developed customized segmentation routines specifically for this purpose. Results show that retinal boundaries and blood vessels localization are more difficult to be correctly discerned from images with poor image quality (**Figure 5.4**). Using an image processing approach to simulate degraded image quality, NFL/GCL thickness increased by 1.3 µm per 10 dB decrease in SNR. This increase in thickness was also observed in a paired analysis of *in vivo* high and low

quality images from the rat eye (+4 μm). These differences in thickness were similar to the nominal resolution of the instrument (4 μm) and are unlikely to have an important impact on the repeatability of retinal thickness measurements. Paired comparisons of clinical images of human eyes using the native segmentation routines of the Spectralis showed no detectable difference in thickness between high quality (≥ 25 dB) and low quality OCT scans, suggesting that the native segmentation routines are robust over a range of image quality. More detailed and systematic studies of the effects of image quality on retinal thickness measurements are needed.

Other studies with human subjects have found that poor image quality leads to differences in thickness measurements (both increased and decreased values have been reported).[201-205] Reported differences in retinal thickness arising from poor image quality may be related to the OCT imaging system as well as the methods of image processing.[206] For example, two studies[202, 205] that used the Stratus OCT (a time-domain OCT system) to evaluate the influence of signal strength, a metric used to quantify image quality, on retinal nerve fiber layer (RNFL) thickness measurements found that RNFL thickness increased by approximately 10 μm with higher signal strengths. Balasubramanian and colleagues evaluated the effect of image quality on thickness measurements using three spectral domain OCT systems.[201] They reported that total retinal thickness increased by 20 to 40 μm with decreasing image quality (average image quality of 24 dB to 11 dB) on the Spectralis. It should be noted that Balasubramanian and colleagues made a deliberate effort to obtain poor quality images. These low quality scans may be similar to the simulated image degradation performed in the present study. The likelihood of acquiring these low quality images in a clinical setting is low and their relevance therefore questionable. It is unlikely that image quality plays an important role in retinal thickness measurements with moderate to high quality images.

In summary, the combined manual + automated realignment procedure helped to repeatedly image the same retinal location between imaging sessions. In future studies, the combined manual + automated realignment procedure will be used to longitudinally track the retinal structural changes associated with elevated IOP in the rat eye.

Chapter Six

Development of a Rat Schematic Eye from in vivo Biometry and Correction of Lateral Magnification in SD-OCT Imaging

Accepted for publication in Investigative Ophthalmology and Visual Science 2013

Citation: Lozano DC and Twa MD. Development of a rat schematic eye from in vivo biometry and the correction of lateral magnification in SD-OCT imaging. *Invest Ophthalmol Vis Sci*, 2013, 54(9), 6446–6455

6.1 Preface

In this chapter, a schematic model eye was developed from in-vivo biometric measurements (e.g. axial length) to compensate for lateral magnification in optical coherence tomography (OCT) images of the neural retina in normal rats. This is an important challenge to address when imaging the rat eye because image lateral magnification has a direct impact on the location of where thickness estimates are acquired. By compensating for image lateral magnification, we were able to show that estimates of retinal thickness and optic nerve head size were in good agreement with previously reported measurements.

6.2 Abstract

Purpose: Optical magnification in optical coherence tomography (OCT) depends on ocular biometric parameters (e.g. axial length). Biometric differences between eyes will influence scan location. A schematic model eye was developed to compensate for lateral magnification in OCT images of the normal rat.

Methods: SD-OCT images were acquired in 19 eyes of 19 Brown Norway rats. Images were scaled using the OCT instrument's built-in scaling function and by calculating the µm/degree from schematic model eyes developed from in-vivo biometry (immersion A-scan and videokeratometry). Mean total retinal thickness was measured 500 µm away from the optic nerve head and optic nerve head diameter was measured. Corneal curvature, lens thickness and axial length were modified to calculate their effects on OCT scan location and total retinal thickness.

Results: Mean total retinal thickness increased by 21µm and the standard deviation doubled when images were scaled with the *Built-in scaling* (222 ± 13 µm) compared to scaling with individual biometric parameters (201 ± 6 µm). Optic nerve head diameter was three times larger when images were scaled with the *Built-in* scaling (925 ± 97 µm) than the individual biometric parameters (300 ± 27 µm). Assuming no other change in biometric parameters, total retinal thickness would decrease by 37 µm for every mm increase in anterior chamber depth due to changes in ocular lateral magnification and associated change in scan location.

Conclusion: Scaling SD-OCT images with schematic model eyes derived from individual biometric data is important. This approach produces estimates of retinal thickness and optic nerve head size that are in good agreement with previously reported measurements.

6.3 Introduction

The use of spectral-domain optical coherence tomography (SD-OCT) for ocular imaging has increased steadily in the recent years, with over 1,500 manuscripts published last year alone. Methods for quantitative analysis of the resulting image data are needed and this is an area of active development that will facilitate further use and correct interpretation of the structural observations available from SD-OCT imaging.

Compensation for lateral magnification is an important consideration with SD-OCT imaging as this influences scan location and, in turn, correct interpretation of measurements that depend on precise positioning. Scan position will vary due to natural biological variations in axial length and other biometric parameters, e.g. corneal power, anterior chamber depth, etc. Changes in these biometric parameters caused by ocular growth or induced by disease also influence scan location and, thereby, interpretation of the size and position of observed structural features. These concerns are relevant to investigators seeking to compare observations between animals, especially when the data are acquired longitudinally or where differences in age, ocular growth, or axial biometric parameters are relevant considerations.

Lateral magnification is especially challenging in the rodent eye due to its small size and corresponding greater optical power. The rat eye is one-third the size of the human eye (6-7 mm axial length) and has significantly greater total optical power (+ 289 D).[117-119] OCT imaging in the mouse or rat eye is typically performed with the aid of a contact lens or cover slip to reduce the optical power of the eye, which will impact image lateral magnification.[207-210] Thus, use of a contact lens or differences in axial length between animals will lead to scans acquired from different retinal locations that will limit the comparability of structural measurements between animals and between studies.

The axial (depth) dimension of SD-OCT imaging is independent of the optical power of the eye and does not change after scaling for lateral magnification. However, the position of the axial scan is directly dependent upon lateral magnification, i.e. total optical power of the eye. Eyes with greater axial length or higher optical power will produce a minified retinal image that alters scan position relative to eyes with shorter axial length. Previous studies of human eyes demonstrated the importance of this effect by showing that OCT thicknesses are comparable between subjects only after correction of image lateral magnification.[211-214]

Previous measurements of the biometric dimensions of the rat eye were invasive and destructive, involving enucleation and histological analysis of the tissue. This approach can alter tissue properties and dimensions.[117-119, 215, 216] Recent studies used less invasive techniques (e.g. A-scan ultrasonography, ultrasound biomicroscopy, and magnetic resonance imaging) to measure axial length in the rat eye.[217-219] However, ultrasonic immersion A-scan measurements were reportedly unreliable beyond postnatal day 17 in the rat because they "*proved impossible to identify peaks corresponding to the posterior crystalline lens and the vitreo-retinal interface*."[218] The objectives of this study were (1) to develop a schematic model of the rat eye from axial biometric measurements in the adult rat (aged greater than 8 months), (2) to quantify the impact of the use of a contact lens on SD-OCT image magnification, (3) to measure total retinal thickness and optic nerve head size from SD-OCT images after compensation for the effects of lateral magnification, and (4) to assess the impact of varying ocular component dimensions on OCT scan location using a schematic model of the rodent eye.

6.4 Methods

All experimental and animal care procedures were approved by the Institutional Animal Care and Use committee of the University of Houston and were in accordance

with the ARVO Statement for the Use of Animals in Ophthalmic and Vision Research. Biometric measurements were collected from 33 male Brown Norway rats (average ± SD weight: 391± 64 g; Age: 10 – 28 months). A subset of these animals (19 of 33 animals; Age: 14 months) was imaged with the Spectralis HRA+SD-OCT system (Heidelberg Engineering, Heidelberg, Germany). Rats were anesthetized with an intraperitoneal injection of ketamine (Vedco, St. Joseph, MO; 50 mg/kg) and xylazine (Vedco, St. Joseph, MO; 5 mg/kg). Pupils were dilated using topically applied 1% atropine sulfate (Bausch and Lomb, Inc., Tampa, FL) and eyes were anesthetized with 1% proparacaine hydrochloride (Bausch and Lomb, Inc., Tampa, FL).

6.4.1 Derivation of Model Eye Parameters

The schematic model eye was developed from the positions and curvature of the refractive surfaces of the rat eye including the cornea, anterior chamber depth, lens, and vitreous chamber depth. Measured biometric parameters were incorporated into the schematic model eye to transform visual angle (in degrees) to retinal size (in microns). Retinal size was determined from the location of the secondary nodal point of the schematic model eye to the retina. The cornea was treated as a single refracting surface while the index of refraction of the crystalline lens was considered to be homogenous. Measured values included in the schematic model included anterior corneal curvature (K), anterior chamber depth (ACD), lens thickness (LT), vitreous chamber depth (VCD), and total axial length (AL). Anterior and posterior lens radii of curvature were measured from digital photographs of excised lenses from 8 animals (n = 8 eyes). The indices of refraction were not measured, but were assumed using values previously reported by Hughes.[119] Individual and mean schematic models were compared to determine if a simplified mean biometric model provided adequate lateral magnification correction for SD-OCT images. For comparison, image lateral magnification was also corrected using the standard scaling factor from the Spectralis SD-OCT system (*Built-in Model)*.

Ultrasonic immersion A-scan measurements (n = 10 scans per eye; AXIS II, Quantel Medical, Bozeman, MT; resolution = 0.04 mm; frequency = 11MHz) were acquired in 33 rats (n = 66 eyes) to measure ACD, LT, VCD, and AL. The ACD and VCD ultrasound velocities used were 1532 m/s, while the ultrasound velocity of the lens was 1641 m/s. A customized immersion cup was constructed for the rat eye (**Figure 6.1A**). The A-scan probe attached to one end of the cylindrical shell and the opposite end was placed in contact with the bulbar conjunctiva and orbital rim of the rat eye. A sample A-scan measurement is shown in **Figure 6.1B**, where peaks corresponded to the anterior corneal surface, anterior and posterior crystalline lens surfaces, and retina. ACD was measured as the peak-to-peak distance between the anterior cornea and anterior crystalline lens, LT was the distance between the positions of the anterior and posterior crystalline lens surface peaks, VCD was the distance between posterior crystalline lens and retinal peaks, and AL was the distance between the anterior corneal and retinal peaks. The mean difference and 95% limits of agreement were calculated between left and right eye biometric measurements. After confirming that the two eyes of each animal were comparable, one eye per animal was randomly selected for study and this sample was used to calculate the average (±SD) of ACD, LT, VCD, and AL measurements. Corneal curvature was measured in 8 animals (n = 8 eyes) using the Keratron Scout videokeratography system (Optikon 2000, Rome, Italy, **Figure 6.1C**).

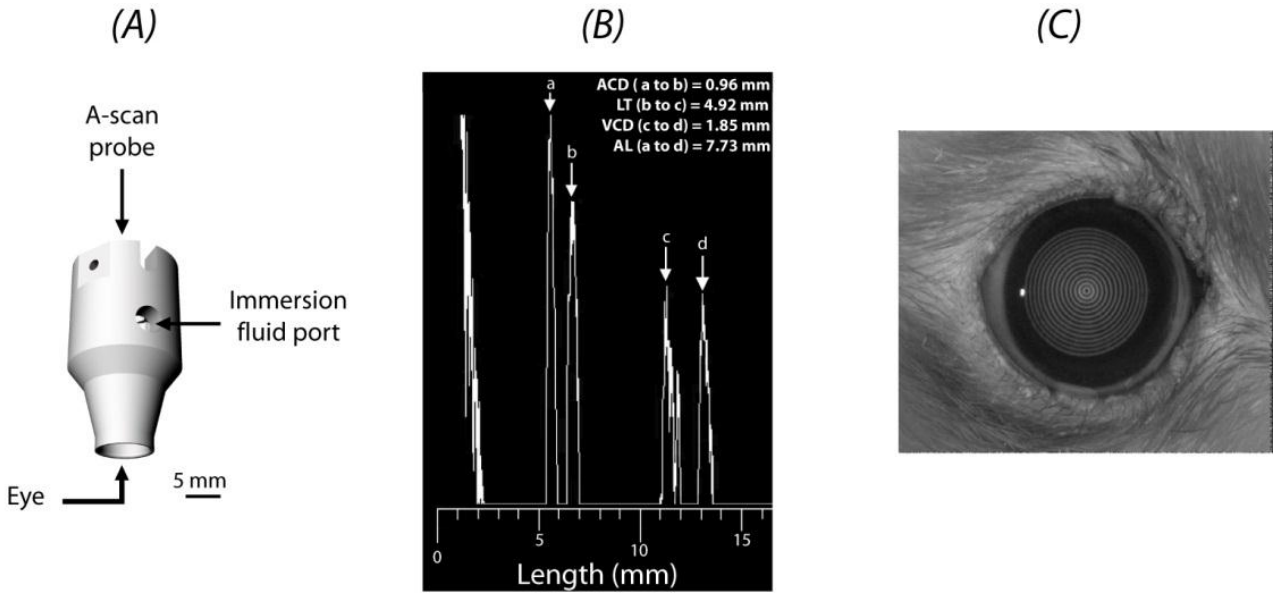

Figure 6.1: Measuring the ocular dimensions in the normal Brown Norway rat.

(A) A custom-built immersion cup, scaled for the rat eye, was used to acquire ultrasonic immersion A-scans. **(B)** A sample immersion A-scan showing the anterior corneal peak (a), anterior (b) and posterior (c) crystalline lens peaks, and retinal peak (d). Anterior chamber depth (ACD) was measured as the distance between a and b; Lens thickness (LT) was measured between b and c; Vitreous chamber depth (VCD) is the distance between c and d; and axial length (AL) is the distance between a and d. **(C)** Anterior corneal curvature was measured using Placido videokeratography.

6.4.2 Model Eye Correction of SD-OCT Lateral Magnification

Each schematic model eye (**Figure 6.2**) was used to correct image lateral magnification in scanning laser ophthalmoscopy (SLO) and SD-OCT images of the rat eye. Animals were imaged with and without a plano powered PMMA contact lens and the potential magnification effects of this lens were also evaluated. This lens was verified as having a 3.35 mm radius of curvature, 6 mm overall diameter, and 270 µm thickness. Three schematic model eyes were used to compensate for image lateral magnification. These models were based upon, individual biometry with and without the PMMA contact lens (*Individual ± CL Model) and* mean biometric parameters with the contact lens (*Mean + CL Model)*.

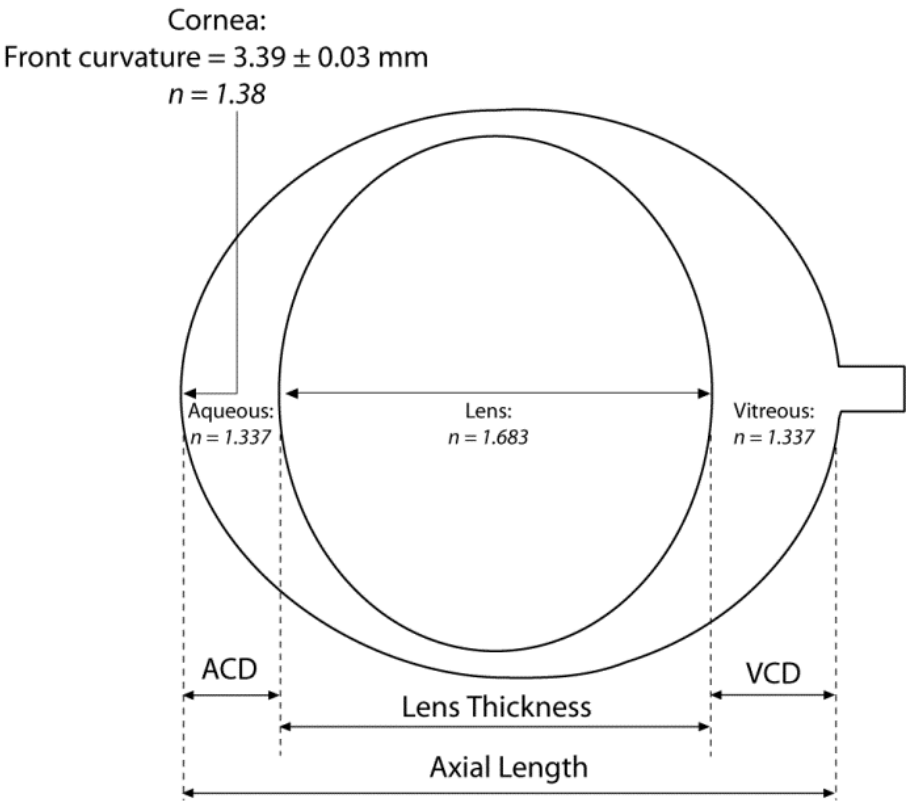

A-Scan Measurement	Mean ± SD	95 % CI
Anterior Chamber Depth (ACD)	1.03 ± 0.17	[0.97, 1.09]
Lens Thickness	4.57 ± 0.45	[4.41, 4.73]
Vitreous Chamber Depth (VCD)	1.32 ± 0.25	[1.22, 1.41]
Axial Length	6.91 ± 0.44	[6.76, 7.07]

Figure 6.2: The schematic model eye was developed from the position and curvature of the refractive surfaces of the rat eye.

The cornea was treated as a single refracting surface while the index of refraction of the crystalline lens was considered to be homogenous. Measured values included in the schematic model and table: anterior chamber depth (ACD), lens thickness (LT), vitreous chamber depth (VCD), axial length (AL), and anterior corneal curvature (K). Indices of refraction (italicized numbers) were based on previous studies by Hughes.

First, the *Individual – CL Model* was used to correct image lateral magnification of images acquired without the contact lens and the *Individual + CL Model* results were used to correct lateral magnification of images acquired with the contact lens. Then, total retinal thickness and optic nerve head diameter were measured from SD-OCT images after compensation of image lateral magnification with the *Built-in Model, Individual + CL Model* or the *Mean + CL Model*. We hypothesized that structural features (e.g. total retinal thickness and optic nerve head diameter) from images acquired with and without the contact lens would be of equal size and that their dimensions would be uncorrelated with axial length after compensation for image lateral magnification.

Retinal images were acquired at a scan speed of approximately 40,000 A-scans per second using a superluminescent diode light source with a central wavelength of 870 ± 55 nm and nominal axial resolution of 4 µm. Eyes were aligned normal to the OCT scan path with a previously established imaging protocol.[220] Briefly, animals were placed in a positioning stage and were rotated and translated such that the optic nerve was aligned to the imaging axis and there was minimal vignetting of the scanning laser ophthalmoscopy (SLO) image. The camera location and focus settings were adjusted to maximize the contrast at the depth of the nerve fiber layer. Then the position of the OCT reference arm was adjusted to bring the SD-OCT B-scan image into view. A 25° x 30° horizontal volumetric image dataset was collected from 19 animals (n = 19 eyes), which was comprised of 31 B-scans, 1536 A-scans per B-scan, and 51 averaged frames per B-scan. Two volumetric image datasets were collected per animal, one with the plano powered contact lens and one without a contact lens (11 of the 19 animals were included).

Two approaches were used to quantify the effects of the contact lens on lateral magnification correction. The first was a computational approach based on determination of the relative magnification required to register SLO images with and

without contact lens use. The second method was based upon the direct measurement and comparison of distances between blood vessels observed in the volumetric SD-OCT images obtained with and without the contact lens. In the computational approach, the mean registration magnification was calculated and a one sample t-test was conducted to evaluate if this value was significantly different from 1 (e.g. no magnification). The magnification parameter was derived from image registration using an affine transformation (e.g. the amount of translation, rotation, shearing, or magnification needed to align two images) of the two SLO images captured with and without the contact lens. The image magnification parameter was calculated using i2K Align Retinal Software (DualAlign CC, version 1.3.8). In the second method, image magnification with and without the contact lens was assessed by comparing the mean center-to-center distance between two adjacent blood vessels in two different SD-OCT image volumes. The difference in these distances between blood vessels in each imaging condition was compared using a paired t-test.

Total retinal thickness was then measured from each of the volumetric image datasets collected from 19 animals (n = 19 eyes). A customized segmentation protocol using a Canny edge detection algorithm (Gaussian filter size of $\sqrt{2}$) was developed (Matlab, Natick, MA) to automatically delineate the inner limiting membrane (ILM) and retinal pigmented epithelium (RPE) from the SD-OCT image data. Intensity peaks of the filtered image corresponded to the layers of interest. Total retinal thickness was measured as the distance between the ILM and RPE. Thickness measurements were taken at each individual A-scan (1536 point-wise measurements) and for all 31 B-scans. Images were corrected for lateral magnification using the three different scaling factors (*Built-In Model, Individual + CL Model,* and *Mean + CL Model*). Three-dimensional spatial thickness maps were generated using bilinear interpolation of thicknesses across individual B-scans (**Figure 6.3**). Mean total retinal thickness was then taken from a

circular scan pattern (diameter = 1 mm) centered on the optic nerve head. Mean total retinal thickness was compared between the three scaling models using repeated measures ANOVA. Linear regression analysis was performed to determine whether total retinal thickness measurements were dependent upon axial length after lateral magnification correction of the image.

After correction for lateral magnification, the diameter of the optic nerve head was determined as the best-fitting circle to a series of circumferential points manually selected at the RPE end near the optic nerve head margin (Bruch's membrane opening). These points were selected from 24 radial B-scan images (15° scan length; 7.5° angular separation) that were centered on the optic nerve head (**Figure 6.4**). Univariate linear regression analysis was performed to analyze the relationship between optic nerve head diameter and axial length.

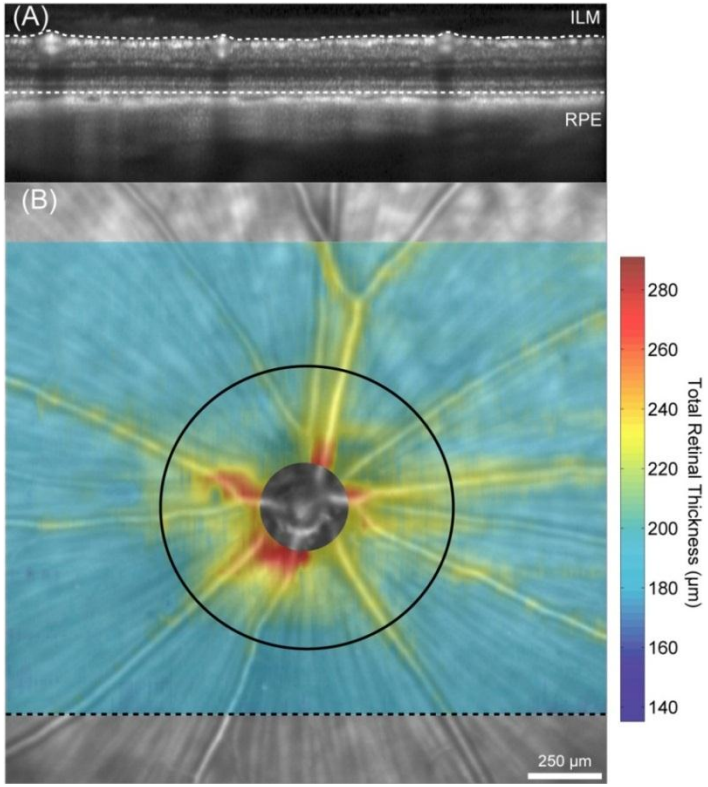

Figure 6.3: Total retinal thickness measurements in the normal Brown Norway rat.

(A) Total retinal thickness was measured from volumetric SD-OCT scans (25°h x 30°w) comprised of 31 horizontally oriented b-scans. The black dashed line in (B) shows the location where the OCT image (A) was acquired. Total retinal thickness was calculated as the distance from the inner limiting membrane to the retinal pigmented epithelium. **(B)** Spatial thickness maps were generated from bilinear interpolation of thickness measurements between successive B-scans. The retinal thickness map is superimposed on top of the scanning laser ophthalmoscope image and shows that thicker measurements are consistently located around blood vessels and near the optic nerve head. The black circle (diameter = 1 mm) was placed on the optic nerve head center and shows the location where mean thickness measurements were calculated and compared between animals

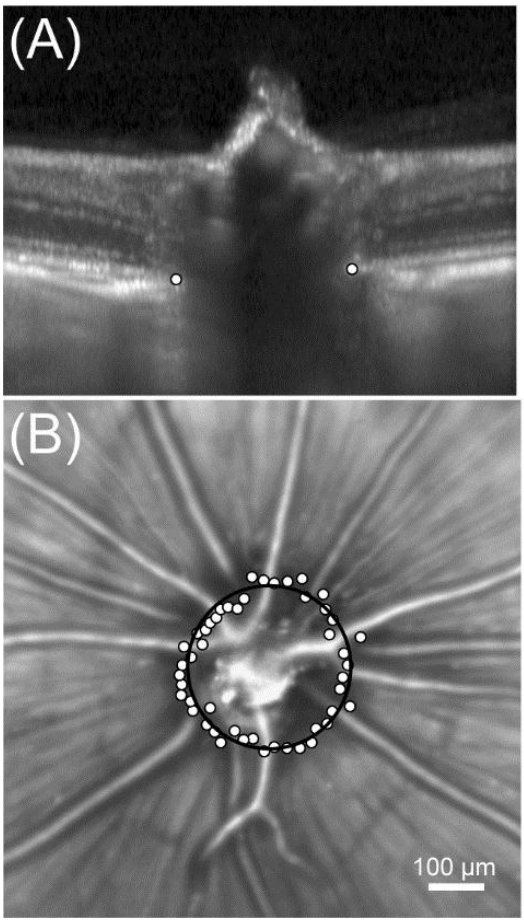

Figure 6.4: Measuring the diameter of the optic nerve head in the normal Brown Norway rat.

(A) Radial scans were acquired around the optic nerve and Bruch's membrane opening (BMO) was manually annotated (white points) for each B-scan (n = 24 radial scans). **(B)** BMO annotations are plotted (white points) on top of the scanning laser ophthalmoscopy image. The optic nerve head diameter was measured from a circle fit (black circle) through BMO annotations.

6.4.3 Impact of Individual Biometric Parameters on Observed Retinal Thickness

Four simulations were developed to assess the impact of varying individual biometric parameters on ocular lateral magnification, SD-OCT scan position and the corresponding retinal thickness measurements. In these simulations, one parameter (ACD, LT, VCD, or corneal curvature) was modified while setting all others to their mean value. Axial length was considered to be the summation of ACD, LT, and VCD. Anterior chamber depth ranged between 0.5 – 2.5 mm in the *ACD Simulation;* lens thickness ranged between 3.7 – 5.4 mm in *the LT Simulation.* In the *VCD Simulation,* the vitreous chamber depth was varied from 0.5 to 2 mm. Lastly, in *K Simulation,* corneal curvature was varied from 2.5 – 3.5 mm while keeping ACD, LT, VCD, and AL constant. Schematic model eyes were generated for each simulation case described above and the corresponding lateral magnification produced by that model was calculated.

A 3D Composite map of rat retinal thickness was constructed by averaging scaled volumetric data from all animals (n = 19) and mean retinal thickness was determined from a circular OCT scan pattern (1 mm diameter) centered at the optic nerve. The observed change in mean total retinal thickness produced by altering each biometric parameter was calculated using univariate linear regression analysis. The interaction between changes in all parameters on magnification was also evaluated using multiple linear regression analysis. Five explanatory variables (ACD, VCD, LT, AL, and K) were included in the multiple linear regression analysis and are shown in *equation 1*. The coefficients (β) for each variable indicate the amount of total retinal thickness difference per mm change for a specific biometric parameter while holding all other parameters constant.

$$Thickness = \beta_0 - (\beta_1 \times ACD) - (\beta_2 \times LT) - (\beta_3 \times VCD) + (\beta_4 \times AL) - (\beta_5 \times K) \qquad eq.1$$

Lastly, variations in ocular biometry between animals will alter scan location, and the impact of this was quantified using a *2D Map Composite* generated from a compilation of

scaled volumetric line scans (n = 19 eyes). Retinal thickness was averaged along the horizontal meridian to determine the horizontal thickness profile (mean ± 95% CI) of the retina. The *Individual + CL Model* was then used to calculate the scan location that would have been observed for each individual animal.

6.5 Results

6.5.1 Derivation of Model Eye Parameters

There was no difference between left and right eyes with respect to ACD (Mean difference: 0.02 mm; *P* = .1), LT (Mean difference: 0.03; *P* = .73), VCD (Mean difference: 0.08 mm; *P* = .11), and AL (Mean difference: 0.13 mm; *P* = .17). One eye per animal was then randomly selected and included to calculate the mean (±SD) ACD (1.03 ± 0.17 mm), LT (4.57 ± 0.45 mm), VCD (1.32 ± 0.25) and AL (6.91 ± 0.44 mm). The mean measured anterior lens radius of curvature was 2.42 ± 0.22 mm and the mean posterior lens radius of curvature was 2.62 ± 0.15 mm. Mean corneal curvature was 3.39 ± 0.03 mm (95% CI: 3.37 to 3.41 mm). **Figure 6.5** shows the distribution of mean ACD, VCD, LT and AL measurements included in the model.

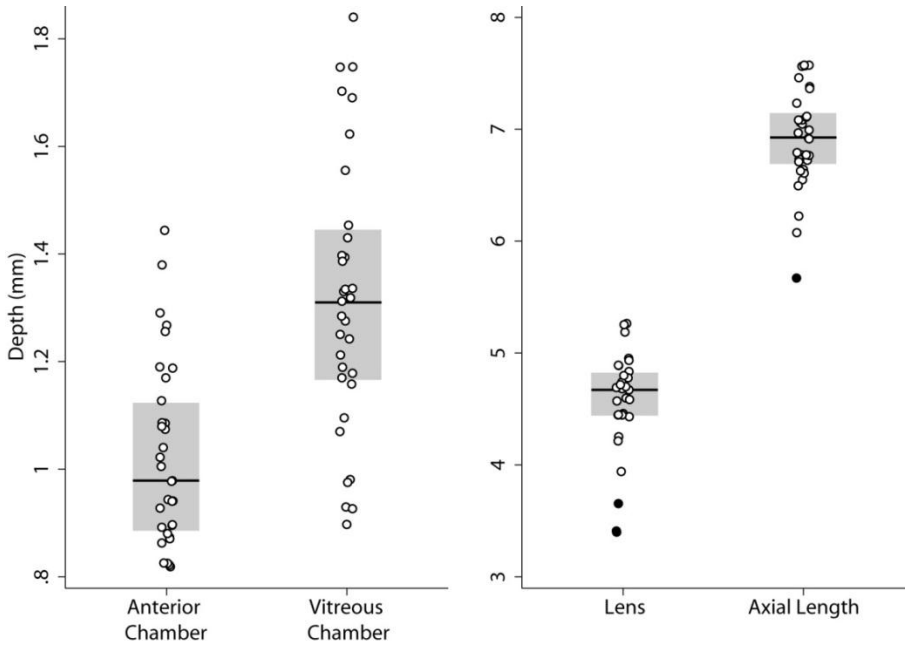

Figure 6.5: Distribution of ultrasonic immersion A-scan biometric measurements in the normal Brown Norway rat.

The points are the ACD, VCD, LT, and AL measurements included in the schematic model eye, the solid black line is the median, the gray box is the interquartile range (IQR), and filled in points are points that fall outside ±1.5 x IQR.

6.5.2 Model Eye Correction of SD-OCT Lateral Magnification

The mean lateral magnification factor (microns per degree of visual angle) for the rat retina calculated from the *Individual + CL Model* was 65.3 ± 6.7 µm/degree (95% CI: 62.9 – 67.6 µm/degree) and for the *Individual –CL Model* it was 62.3 ± 6.6 µm/degree (95% CI: 59.9 – 62.9 µm/degree).

The registration magnification parameter computed from the affine image registration of SLO images captured with and without the contact lens was 1.00 ± 0.03 (95% CI: .98 to 1.02) and this value was not significantly different from 1 (P = .94). The distances between selected blood vessels calculated from images acquired without the contact lens (95% CI: 213 to 389 µm) were not significantly different (P = .49) from the distances measured from images with the contact lens (95% CI: 207 to 380 µm).

Figure 6.6 shows that significantly greater total retinal thickness measurements were acquired when images were scaled using the *Built-in Model* (222 ± 13 µm; 95% CI: 216 to 228 µm) versus the *Individual + CL Model* (201 ± 6 µm; 95% CI: 198 to 204 µm; P < .001) or the *Mean + CL Model* (201 ± 6 µm; 95% CI: 198 to 203 µm; P < .001). There was no significant difference (P = .74) between mean total retinal thickness when images were scaled with the *Individual + CL Model* vs. *Mean + CL Model.* There was a non-significant relationship between mean total retinal thickness and axial length after images were scaled using the *Built-in Model* (R^2=0.13; P = .12), *Individual + CL Model* (R^2 = 0.08, P = .24) or the *Mean + CL Model* (R^2 = 0.03, P = .47).

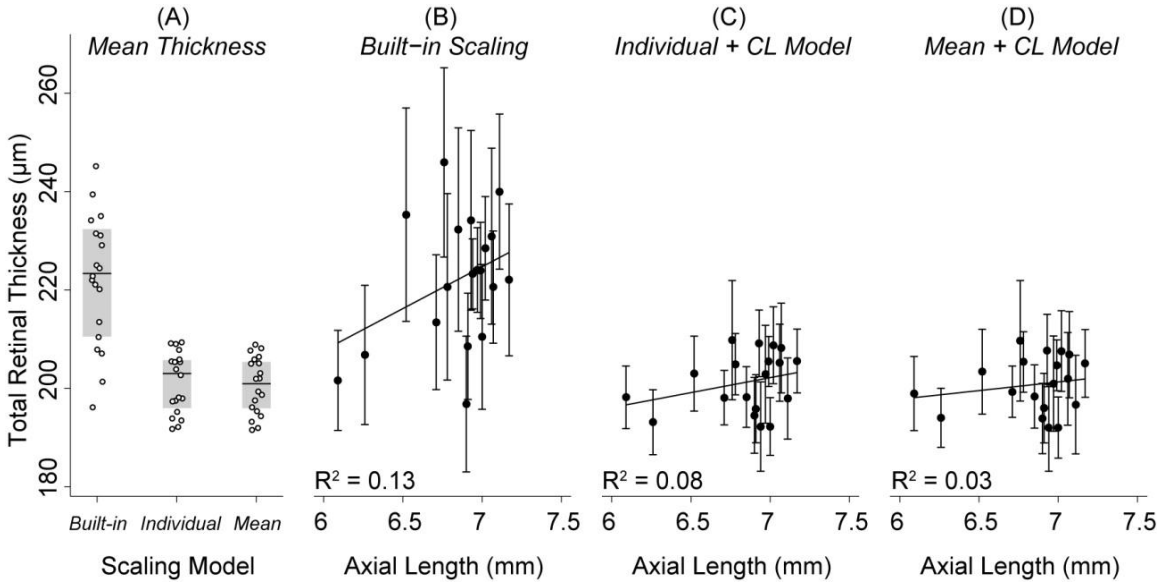

Figure 6.6: Mean total retinal thickness measured 500 µm away from the optic nerve head center in normal Brown Norway rats.

(A) Mean total retinal thickness for each animal (white points) after images were scaled using the *Built-in* scaling, *Individual + CL Model* or *Mean + CL Model*. The gray box shows the interquartile range of the data and the black line is the median. Significantly greater total retinal thickness measurements were acquired after images were scaled using the built-in factor (222 ± 13 µm) than either the *Individual + CL Model* (201 ± 6 µm; $P < .001$) or the *Mean + CL Model* (201 ± 6 µm; $P < .001$). Total retinal thickness was not significantly ($P = .74$) different when images were scaled with the *Individual + CL* or the *Mean + CL Model.* **(B)** The goodness of fit (R^2) between total retinal thickness and axial length was not significantly different from zero after images were scaled with the *Built-in Model* (R^2=0.13; $P = .12$) or the **(C)** *Individual + CL Model* (R^2=0.08; $P = .24$) or **(D)** the *Mean + CL Model* (R^2=0.03; $P = .47$).

Figure 6.7 shows that the optic nerve head diameter was significantly larger when images were scaled with the *Built-In Model* (925 ± 97 µm; 95% CI: 878 to 972 µm) than when images were scaled with the *Individual + CL Model* (300 ± 27 µm; 95% CI: 287 to 313 µm; $P < .001$) or the *Mean + CL Model* (297 ± 29 µm; 95% CI: 283 to 311 µm; $P < .001$). There was a non-significant relationship between optic nerve head diameter and axial length after images were scaled using the *Built-in* model (R2 = .11, $P = .17$), the *Individual + CL Model* ($R^2 = 0.01$; $P = .74$), or the *Mean + CL Model* ($R^2 = 0.20$; $P = .06$).

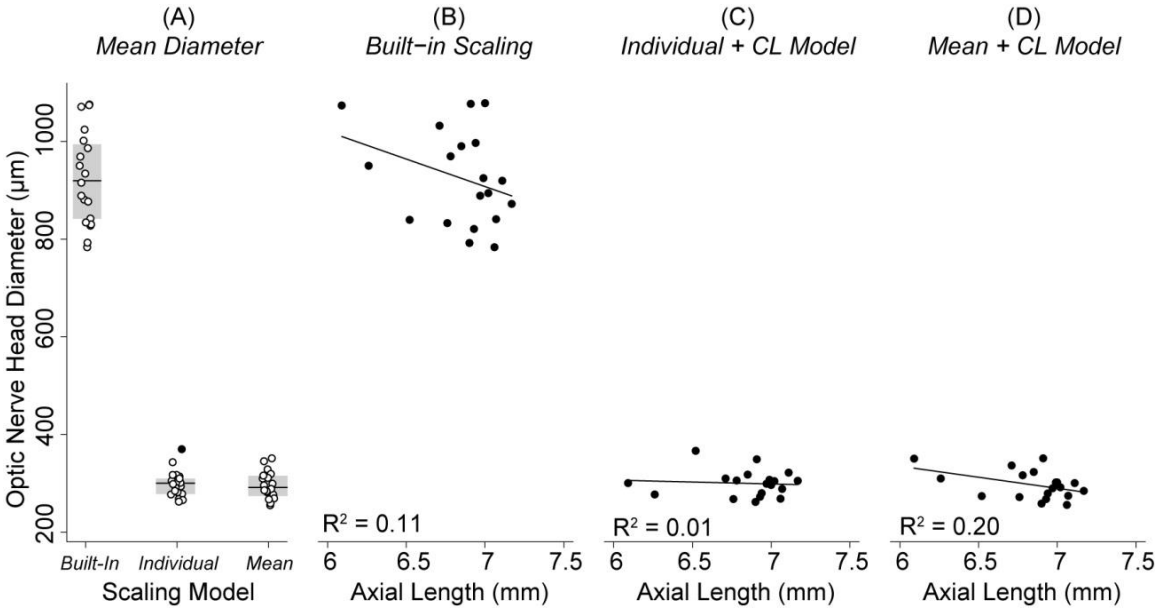

Figure 6.7: Optic nerve head diameter in the normal Brown Norway rat.

(A) Points show the distribution in optic nerve head diameters between animals included in the study. The gray box shows the interquartile range (IQR) of the data, the black line is the median, and the filled in points are points that fall outside ±1.5 x IQR. Optic nerve head diameter was significantly larger when images were scaled with the *Built-In* scaling (925 ± 97 µm) than when images were scaled with the *Individual + CL Model* (300 ± 27 µm, $P < .001$) or the *Mean + CL Model* (297 ± 29 µm, $P < .001$). There was a non-significant relationship between optic nerve head diameter and axial length after images were scaled using the **(B)** *Built-in* model ($R^2 = .11$, $P = .17$), **(C)** the *Individual + CL Model* ($R^2=0.01$; $P = .74$), or the **(D)** *Mean + CL Model* ($R^2=0.20$; $P = .06$).

6.5.3 Impact of Individual Biometric Parameters on Observed Retinal Thickness

In each case the reference scan location was set to 500 µm away from the optic nerve head center for comparison purposes. Over the range of ACD values tested, the observed scan location in the *ACD Simulation* was 477 ± 30 µm away from the optic nerve head center (95% CI: 463 – 491 µm), in *LT Simulation* it was 508 ± 64 µm (95% CI: 476 – 540 µm), in *VCD Simulation* it was 517 ± 68 µm (95% CI: 481 – 554 µm), and *K Simulation* it was 501 ± 37 µm (95% CI: 484 – 518 µm). **Figure 6.8** shows the effect that each of these biometric parameters had on the observed total retinal thickness as a consequence of varying scan position due to differences in ocular lateral magnification. These results show that retinal thickness increased or decreased between 2 – 6 µm per mm change for each biometric parameter. For example, total retinal thickness measurements increased by 3 µm per mm deepening of the ACD (*ACD Modifications*). The multiple linear regression results are shown in equation 2. The goodness of fit (adjusted R-squared) for this equation was 0.995 and indicates that 99.5% of the variability observed in retinal thickness is accounted for by the model, even after taking into account the number of predictor variables (e.g., ACD, VCD, LT, etc.) in the model. For example, this equation shows that if the angular position of scan location is not changed, total retinal thickness would decrease by 37 µm for every mm increase in ACD due to changes in ocular lateral magnification, assuming that all other parameters are constant.

$$TRT = 174 - (37 \times ACD) - (34 \times LT) - (33 \times VCD) + (40 \times AL) - (3 \times K) \qquad eq.2$$

Figure 6.9 illustrates the influence that differences in ocular biometry between animals can have on SD-OCT scan diameter. The actual 500 µm scan radius was magnified to 506 µm (95% CI: 490 to 522 µm). This variation in the scanned position resulted in observed total retinal thickness that was between 195 to 201 µm (95% CI).

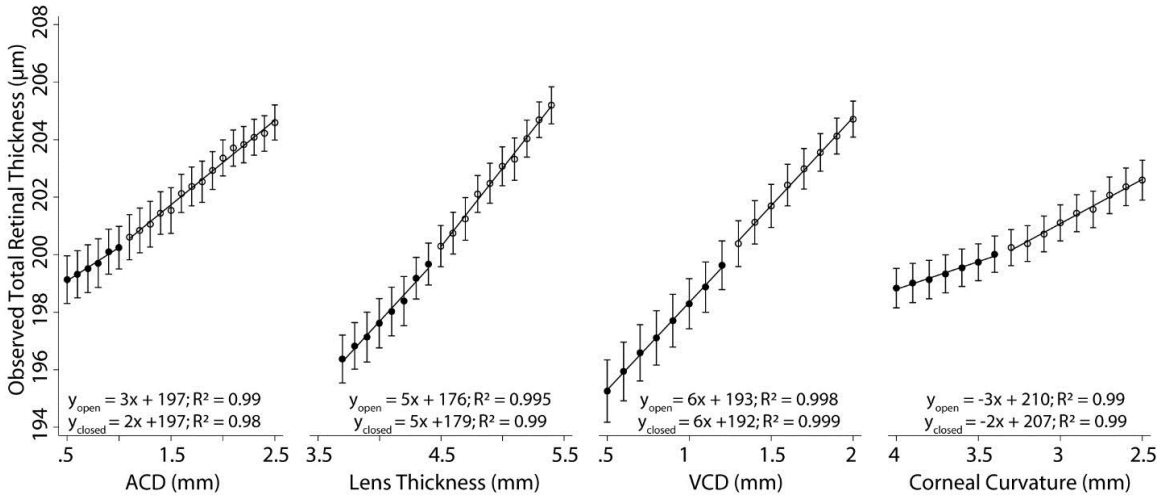

Figure 6.8: Four simulations were developed to quantify the impact of changing the model eye parameters on scan location and measured total retinal thickness at the new scan location.

In these simulations, one parameter (ACD, LT, VCD, or corneal curvature) was modified at a time while setting all others to their mean value. Axial length was considered to be the sum of ACD, LT, and VCD. Each parameter (ACD, LT, VCD, or corneal curvature) was modified to be either smaller (closed circles) or larger (opened circles) than the mean value for that particular parameter. The linear regression equations show that total retinal thickness changed between 2 to 6 µm per mm change in the parameters.

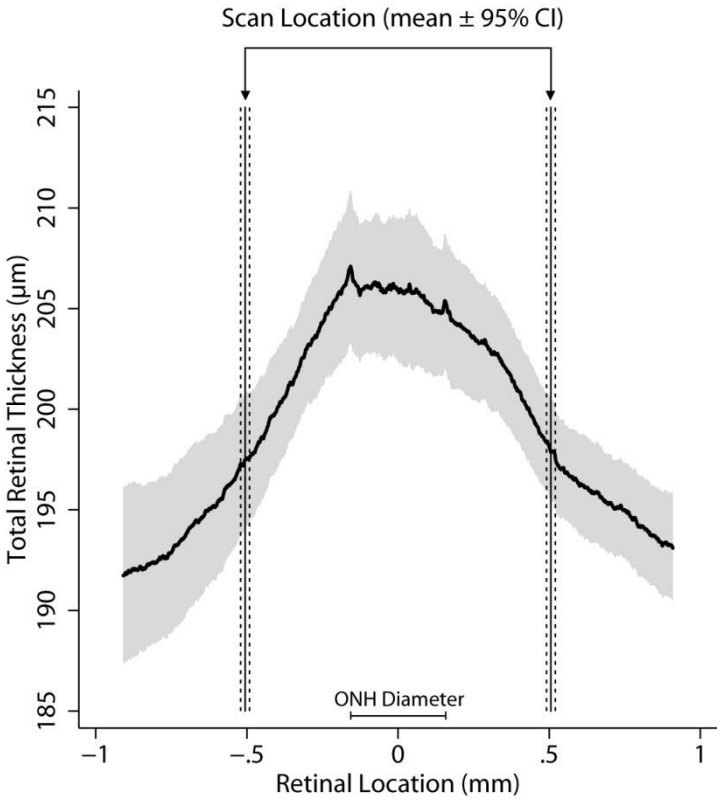

Figure 6.9: Distribution in total retinal thickness within the central 2 mm retinal area in normal Brown Norway rats.

Total retinal thickness maps were scaled using the *Mean + CL Model* and cropped to cover a similar retinal area between animals. The mean (solid curved line) and 95% confidence intervals (gray area) was calculated along the horizontal dimension from these maps. The *Individual + CL Model* were used to determine the expected scan location. The vertical solid lines represent the mean scan location and the dashed lines are the associated 95% confidence interval. This figure illustrates the variability in OCT scan location due to differences in biometry between animals as well as the possible range of observed total retinal thickness due to scan position.

6.6 Discussion

The purpose of this study was to develop a schematic model eye of the rat to properly account for image lateral magnification. These results will facilitate the correct measurement and interpretation of structural observations from SD-OCT imaging between animals, within animals imaged longitudinally, or when comparing observations between studies. The proposed schematic model eye was developed from in-vivo measurements of the ocular dimensions in the rat. Using an immersion cup developed for the rat eye improved the visibility of A-scan peaks, enabling us to measure the axial dimension of the adult rat eye by immersion A-scan ultrasonography with good repeatability.

The resulting schematic model eyes were used to scale SLO and SD-OCT images captured with and without a contact lens and found that the plano powered contact lens used did not significantly impact image lateral magnification. These results suggest that structures measured from images captured with this contact lens are not magnified. The advantage of using the contact lens is that it improves image quality, maintains normal corneal hydration, and prevents loss of lens clarity.[221, 222] Next, total retinal thickness was measured and compared after correcting for image lateral magnification using the *Built-in Model*, an individual (*Individual + CL Model)* and mean (*Mean + CL Model)* schematic models. Higher thickness values and larger optic nerve head diameters were measured after scaling images with the *Built-in Model* relative to the schematic model eyes evaluated. The *Mean + CL Model* did not yield significantly thicker/thinner total retinal thickness measurements or bigger/smaller optic nerve head diameters than images that were scaled using the *Individual + CL Model*. These results suggest that the mean biometry data for normal animals provided adequate lateral magnification correction for SD-OCT images in the normal adult rat eye.

Nissirios et al. reported a ~71% increase in anterior chamber depth in rats with experimental glaucoma.[219] The amount of change in the axial dimension may vary between animals and an individualized schematic model eye is likely needed to correct image lateral magnification for animals whose biometry is changed by disease induction. Ocular biometry can vary for a number of other reasons, including strain, age, gender, etc., and this variability can impact the scaling required to compensate for image lateral magnification. For example, the anterior corneal curvature measurements reported in this study were flatter than previously reported by others (3.39 mm vs. 3.13 mm) and differences in rat strain (Brown Norway vs. albino Sprague-Dawley) may account for some of the variability between the reported values.[223] We have also observed corneal curvature differences (~0.5 mm steeper, data not shown) in another cohort of Brown Norway rats of similar age, but obtained from a different colony.

Ocular biometry (e.g. axial length, anterior chamber depth, etc.) also changes with age and the rate of change in these parameters was calculated by combining the results from previous studies reporting the axial dimensions in rats that ranged in age from post-natal day 17 to 28-months. **Figure 6.10** shows the results from 9 studies (including this study) that measured the axial dimension of the rat eye either from histological processing or from in-vivo measurements (by A-scan, UBM, or MRI).[117-119, 215-219] Age related changes in ocular biometry were analyzed with log-regression analysis through the results from these 9 studies. While differences in biometric parameters are reported (corneal thickness, lens curvature and thickness, axial length, etc.), they are relatively small in comparison to differences due to age (**Figure 6.10**). For example, a comparison of results from studies with two different strains of comparable ages (Hughes 1978: 115-130 days old; Chaudhuri 1983: >120 days old) shows that axial length differed between these two cohorts by 0.152 mm. Using the model eye parameters from this study, this difference would change the length of a 30-degree OCT

line-scan by 4% (60 µm/1593 µm). However, axial length can change by almost 2 mm, from 5 mm at 1 month-of-age to 6.8 mm at 15 months-of-age. This will effectively change the length of a 30-degree OCT line-scan by 46% (600 µm /1900 µm). This underscores the impact that ocular biometry changes due to age may have on image lateral magnification and subsequent structural measurements.

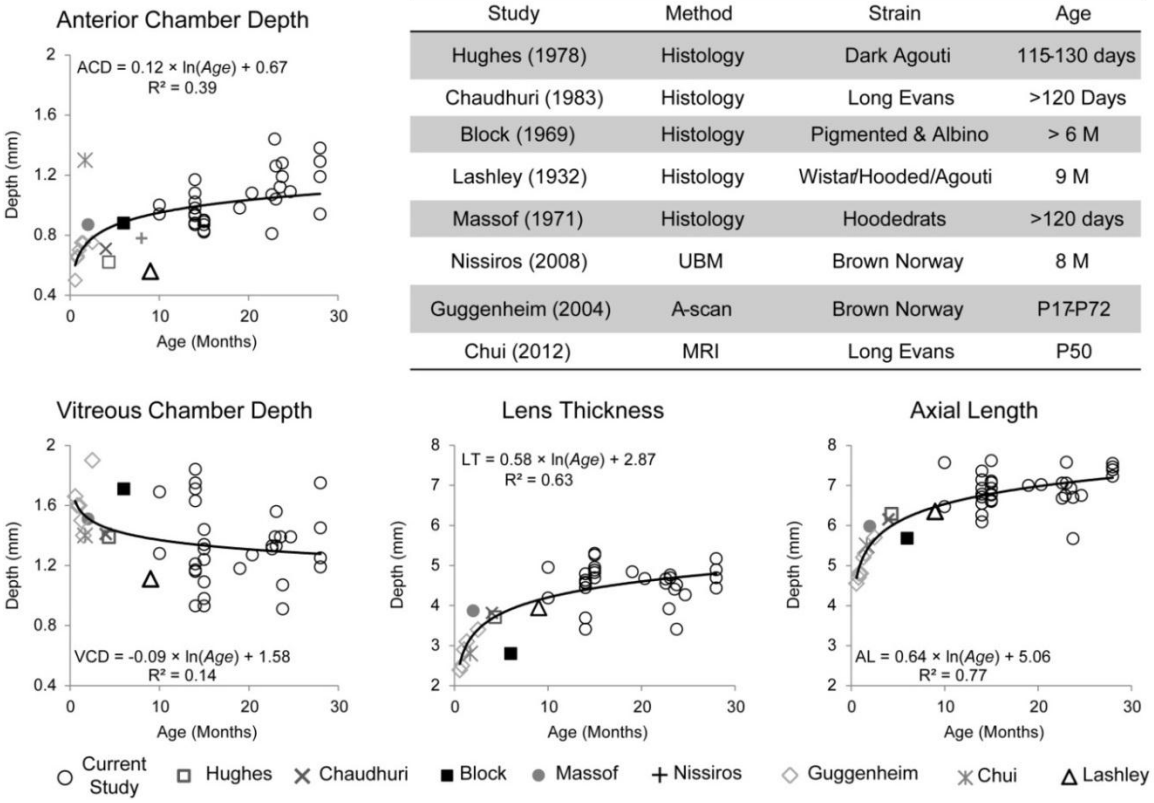

Study	Method	Strain	Age
Hughes (1978)	Histology	Dark Agouti	115-130 days
Chaudhuri (1983)	Histology	Long Evans	>120 Days
Block (1969)	Histology	Pigmented & Albino	> 6 M
Lashley (1932)	Histology	Wistar/Hooded/Agouti	9 M
Massof (1971)	Histology	Hoodedrats	>120 days
Nissiros (2008)	UBM	Brown Norway	8 M
Guggenheim (2004)	A-scan	Brown Norway	P17-P72
Chui (2012)	MRI	Long Evans	P50

Figure 6.10: Age-related changes in anterior chamber depth, vitreous chamber depth, lens thickness and axial length in normal rats.

The table shows the method used to measure these ocular dimensions, the strain and age of the animals. These graph show that there is an early fast growth in the ocular dimension in the rat eye and the growth progressively slows as the animal ages.

Total retinal thickness observed in this study was different from previous histological or in-vivo measurements and this difference appears to be due, in part, to age differences, inter-animal differences, or the underlying assumptions used to compensate for image lateral magnification in other studies. In the current study, mean total retinal thickness 500 µm away from the optic nerve head center was 201 ± 6 µm and this was thinner than histological measurements of total retinal thickness acquired from similar retinal locations (~210 µm) in other studies.[224] Differences in weight/age of the animals (391 g vs. 270 g) can account for some of the disparity in thickness measurements between these studies. For example, there are age-related changes in thickness where total retinal thickness decreased by ~60 µm between adult (12-month-old, 210 ± 31.6 µm) and old (24-month-old, 150 ± 18.3 µm) rats.[225]. Guo et al. imaged Dark-Agouti rats with a commercial SD-OCT system (Spectralis) and reported that total retinal thickness was 172.19 ± 5.17 µm approximately 350 µm away from the optic nerve head center.[116] Inter-animal differences in total retinal thickness can account for some of the variability in the reported measurements between these studies. For example, **Figure 6.9** shows that total retinal thickness can vary by 6 µm between animals of different strains. Another component of the variability in reported thickness measurements can be attributed to the underlying assumptions used to compensate for image lateral magnification. For example, Guo and colleagues assumed that the posterior focal length of the rat eye was 4.5 mm, as previously reported by Campbell.[188] Campbell considered a non-homogenous index of refraction for the lens. The scaling factor for a 4.5 mm posterior focal length is 78.5 µm/degree, as opposed to the 65.3 ± 6.7 µm/degree calculated in the current study. The difference in scaling factors between these two studies underscores the importance of stating the assumptions made when compensating for image lateral magnification, as this will impact the reported scanned position and subsequent reported thickness measurements.

The optic nerve head diameter was three times larger when images were scaled with the *Built-in* scaling model (925 ± 97 µm) than when lateral magnification was compensated with the *Individual + CL Model* (300 ± 27 µm) or the *Mean + CL Model* (297 ± 29 µm). A previous study showed that the rat optic nerve diameter was 300 µm, well within the measured optic nerve head diameter reported here, after images were scaled with the schematic model eye.[226] The Built-in model is meant to compensate for image lateral magnification in the human eye (approximately 3 times larger than the rat eye) and the large difference observed in the scaled optic nerve head diameter is proportional to the difference in optical power between the rat and human eye. This fact highlights the importance of compensating for image lateral magnification with an appropriate model. There was also a weak correlation between optic nerve head diameter and axial length irrespective of the method used to compensate for image lateral magnification. We conclude that the schematic model eye built from in-vivo ocular biometric measurements provides a good approximation to compensate for image lateral magnification and that structural measurements made after compensating for image lateral magnification with the schematic model eye are in good agreement with previous measurements of the normal rat.

A limitation of the current study is the difficulty of aligning the A-scan probe along the same optical axis between animals. This misalignment may yield smaller measurements or greater variability in the measurements as evident from the higher coefficient of variation for VCD measurements (18.2 ± 7.3%) than axial length (4.6 ± 2.1%). Advances in ocular imaging (e.g. long range OCT scanning) will help address this limitation as it has already been demonstrated that the entire dimension of the mouse eye can be imaged with custom built SD-OCT systems.[227-229]

The schematic model eye results reported here may improve further if a core lens model and lens curvature measurements from the specific animals included in the study

are used. Chaudhuri reports that the position of the posterior nodal point would move backwards by ~0.05 mm if the core lens model is used instead of the homogenous model.[118] This change in the position of the posterior nodal point would lead to an increase in total retinal thickness of ~1 µm and the optic nerve head diameter would increase by ~6 µm.

The schematic model eyes described in this study provide an appropriate way to compensate for image lateral magnification in the normal rat eye. Future studies should quantify these changes for other strains. While this model is based upon biometric measurements from male rats, it could easily be adapted to female rats that have a different growth rate than male rats.[230] This image scaling approach has been used for scaling OCT images in non-human primates and may be used for other species as well.[28]

Chapter Seven

Quantification of Circumpapillary Retinal Thickness from Volumetric SD-OCT Images in Normal Rats and in a Rat Model of Glaucoma

Contributing Authors:

Diana C. Lozano, Jason Porter , Michael D. Twa

7.1 Preface

In this chapter, spectral domain optical coherence tomography scans of the neural retina were used to quantify the spatial distribution of retinal thicknesses and to measure the diameter of the optic nerve head in normal adult Brown Norway rats and in a rat model of glaucoma. IOP was measured with the calibrated rebound tonometers discussed in Chapter Two. The imaging methods developed in Chapter Five were used to image the same retinal location between imaging sessions. The scaling methods developed in Chapter Six were used to develop schematic eyes to compensate for image lateral magnification. The general findings of this study were that, in normal eyes, the nerve fiber layer/retinal ganglion cell layer thickness was greatest in the temporal retinal quadrant, in agreement with previous histological studies that indicated that the highest density of retinal ganglion cells is found in the temporal quadrant. In rats with experimental glaucoma, maximum IOP measured over the course of the experimental study correlated well with larger optic nerve heads. Furthermore, rats with larger optic nerve heads and thinner retinas showed greater histological damage (e.g. collapsed myelin sheaths and gliosis) throughout optic nerve cross-sections, further supporting the idea that this structural damage is a result of the elevation in IOP.

7.1 Abstract

Purpose: To quantify the spatial distribution of retinal thickness in the adult Brown Norway rat and to evaluate structural changes in a rat model of glaucoma using computationally generated and scaled circumpapillary scans.

Methods: Spectral domain optical coherence tomography (Spectralis HRA+OCT) images were acquired in 18 normal aged male Brown Norway rats (36 eyes; weight = 422 ± 32 g). IOP was surgically elevated in six of these animals (6 eyes) by injecting hypertonic saline into an episcleral vein. Pre- and post-injection images were corrected for lateral magnification using individual ultrasonic axial biometric measurements. Circumpapillary scans were generated from 30° x 25° horizontal raster retinal scans centered on the optic nerve head. Global (mean of circumpapillary scan) and regional (superior, inferior, nasal, and temporal) mean nerve fiber layer/retinal ganglion cell layer (NFL/RGCL), NFL/RGCL plus inner plexiform layer (NFL/RGCL+IPL), and total retinal thicknesses were calculated from the circumpapillary scans. Optic nerve head (ONH) diameter was measured by fitting a circle though annotations of Bruch's membrane opening.

Results: In normal rats, mean temporal NFL/RGCL thickness (39 ± 6 μm) was significantly thicker than inferior (33 ± 5 μm) and superior (31 ± 5 μm) NFL/RGCL thicknesses ($P < .05$), but was not significantly different from the nasal quadrant (36 ± 8 μm; $P > .05$). In the rat model of glaucoma, IOP was significantly higher for 5 to 10 weeks (95% CI: 21 – 43 mm Hg) after disease induction compared to baseline (95% CI: 17 – 20 mm Hg; $P = .02$). Baseline NFL/RGCL thickness measured from a 0.5 mm circumpapillary scan radius was 83 ± 10 μm (95% CI: 72 – 94 μm) and decreased by 17% (68 ± 17 μm; 95% CI: 51 – 86 μm) after surgical elevation of IOP, but this thickness

decrease did not reach significance (*P* = .09). ONH enlargement correlated well with histological optic nerve damage (r^2 = .48; *P* = .01).

Conclusion: SD-OCT is a viable method for *in vivo* detection of ONH enlargement and decreased retinal thickness in rats with experimental glaucoma. The decrease in circumpapillary retinal thicknesses in the rat model of glaucoma correlated well with histological assessment of optic nerve damage (e.g. gliosis and collapse myelin sheaths).

7.3 Introduction

Quantification of structural damage to the optic nerve head and peripapillary tissues is critical to the diagnosis and monitoring of glaucomatous damage. Various in-vivo imaging modalities (e.g. optical coherence tomography (OCT), adaptive optics scanning laser ophthalmoscope) are providing essential information about changes in retinal thickness and changes to the optic nerve head region (e.g. cupping) in glaucoma.[31, 184, 231-239] Several groups are looking at morphological changes in the lamina cribrosa in humans and non-human primates as an indicator of early damage in glaucoma.[31, 32] Currently, there is a disagreement about the value of using retinal thickness as a useful indication of glaucoma. The thought is that these changes in retinal thickness occur too late in the disease process to be used as an early indicator of disease.[240, 241] However, others have shown that macular retinal thickness is useful for detecting early glaucoma.[242-244] Here, we explore the usability of measuring retinal thickness as an indicator of axonal degeneration in a rat model of experimental glaucoma.

Circumpapillary OCT scans of the neural retina show that the nerve fiber layer thickness in normal healthy humans is thicker in the superior and inferior retinal quadrants and that these quadrants are more susceptible to damage in patients with glaucoma than other quadrants.[30, 42-44] Whether these quadrant specific thickness variations exist in rodents is still a matter of debate, with some histological studies showing that the highest density of retinal ganglion cells in rats is located between the superior and temporal retinal quadrants,[45-51] while others have not.[52] It is also unclear if the location of highest retinal ganglion cell density determined histologically in the rat retina correlates with *in vivo* OCT retinal thickness measurements from retinal locations where the nerve fiber layer/retinal ganglion cell layer is thickest.

In a previous study, circumpapillary retinal scans were acquired in rats using a clinical OCT system.[194] However, the size of the circumpapillary scans in clinical OCT systems are optimized for a human eye, and may not be optimal for the rat eye.[245, 246] Furthermore, changes in ocular biometry (e.g. deepening of the anterior chamber) may occur after acute and chronic elevations in IOP that will impact the location of where retinal thickness measurements are acquired.[219] Since the rat retina thins with increasing radial distance from the optic nerve head, changes in the optical power (lateral magnification) may lead to erroneous results that could indicate decreased thickness estimates which are unrelated to elevations in IOP. The present study is innovative because OCT retinal scans were compensated for image lateral magnification to quantify:[246] (1) thickness estimates as a function of distance from the optic nerve head and by retinal quadrant (superior, inferior, nasal, and temporal) in normal rats; and (2) in-vivo structural changes (retinal thickness and diameter of the optic nerve head) in a rat model of glaucoma. These in-vivo structural changes were also correlated with histological assessments of the optic nerve cross-sections.

7.4 Methods

7.4.1 In-vivo Retinal Thickness Estimates in Normal Rats

All experimental and animal care procedures were approved by the Institutional Animal Care and Use Committee of the University of Houston and were in accordance with the ARVO Statement for the Use of Animals in Ophthalmic and Vision Research. Eighteen normal aged male Brown Norway rats (36 eyes; weight = 422 ± 32 g) were imaged with the Spectralis HRA+SD-OCT system (Heidelberg Engineering, Heidelberg, Germany). Rats were anesthetized with an intraperitoneal injection of ketamine (Vedco, St. Joseph, MO; 50 mg/kg) and xylazine (Vedco, St. Joseph, MO; 5 mg/kg) and pupils

were dilated using topically applied 1% atropine sulfate (Bausch and Lomb, Inc., Tampa, FL).

Retinal images were acquired at a scan speed of approximately 40,000 A-scans per second using a superluminescent diode light source with a nominal axial resolution of 4 µm. Eyes were aligned normal to the OCT scan path with a previously established imaging protocol.[220] Briefly, animals were rotated and translated until the optic nerve was aligned to the imaging axis. The camera focus settings were adjusted to maximize the contrast at the depth of the nerve fiber layer. Then the position of the OCT reference arm was adjusted to bring the SD-OCT B-scan image into view. A 25° x 30° horizontal raster retinal scan was collected per animal, which was comprised of 31 B-scans, 1536 A-scans per B-scan, and 51 averaged frames per B-scan (**Figure 7.1**).

Spatial retinal thickness maps were generated from each of the horizontal raster retinal scans. A customized segmentation protocol using a Canny edge detection algorithm was developed (Matlab, Natick, MA) to semi-automatically delineate the inner limiting membrane (ILM), nerve fiber layer/retinal ganglion cell layer (NFL/RGCL), inner plexiform layer (IPL), retinal pigmented epithelium (RPE) and blood vessels from the SD-OCT image dataset (**Figure 7.1**). NFL/RGCL thickness was measured as the distance between the ILM and NFL/RGCL. NFL/RGCL + IPL thickness was measured as the distance from the ILM to the IPL. Total retinal thickness was measured as the distance between the ILM and RPE. Thickness measurements were taken at each individual A-scan (1536 point-wise thickness measurements) and for all 31 B-scans. Then, spatial thickness maps were generated from bilinear interpolation of thicknesses across individual B-scans (**Figure 7.1**). These spatial thickness maps were then corrected for lateral magnification using the animal's ocular biometric information as described in our previous studies.[246] Briefly, a schematic model eye was developed based on the curvature of the anterior corneal surface and the relative locations of the anterior corneal

surface, anterior and posterior surfaces of the lens, and retina (i.e., anterior chamber depth, lens thickness, vitreous chamber depth, and axial length). These parameters were then used to convert visual angles (in degrees) from SD-OCT images to scaled retinal position (in microns).

Computationally generated circumpapillary scans were created by transforming the spatial thickness maps into polar space and extracting thickness measurements at various radii (0.3, 0.4, 0.5, and 0.6 mm) from the optic nerve head center. The center of the optic nerve head was determined to be the center of a best-fit circle through points that delineated the RPE termination near the optic nerve head margin (Bruch's membrane opening; **Figure 7.1**). These points were manually selected from 24 radial B-scan images (15° scan length; 7.5° angular separation) that were centered on the optic nerve head (**Figure 7.1**). These radial scans were segmented three times and we report the mean of the optic nerve head diameter and its center. Blood vessel fraction was calculated as the percent of blood vessel regions (i.e., edge to edge distance of the shadow cast by blood vessels in the deeper retinal layers) divided by the total linear distance of the circumferential scan. Circumpapillary scans were then used to address three key points: (1) examine the impact of blood vessels on estimates of NFL/RGCL thickness and NLF/RGCL + IPL thickness; (2) determine if there were differences between left and right eye retinal thickness measurements; and (3) assess quadrant (superior, temporal, inferior, and nasal) specific retinal thickness differences. After confirming that thickness estimates of both eyes from the same animal were comparable, one eye from each animal was randomly selected to generate a mean circumpapillary scan model along with its corresponding 95% confidence interval. Spatial thickness maps were flipped vertically to compare similar thickness measurements between retinal quadrants among all eyes (i.e., all eyes were made to appear as though they were right eyes). Retinal thickness differences by retinal quadrant were analyzed

from the circumpapillary scan model using one way ANOVA followed by Post-hoc Tukey's HSD Test at the .05 level of significance.

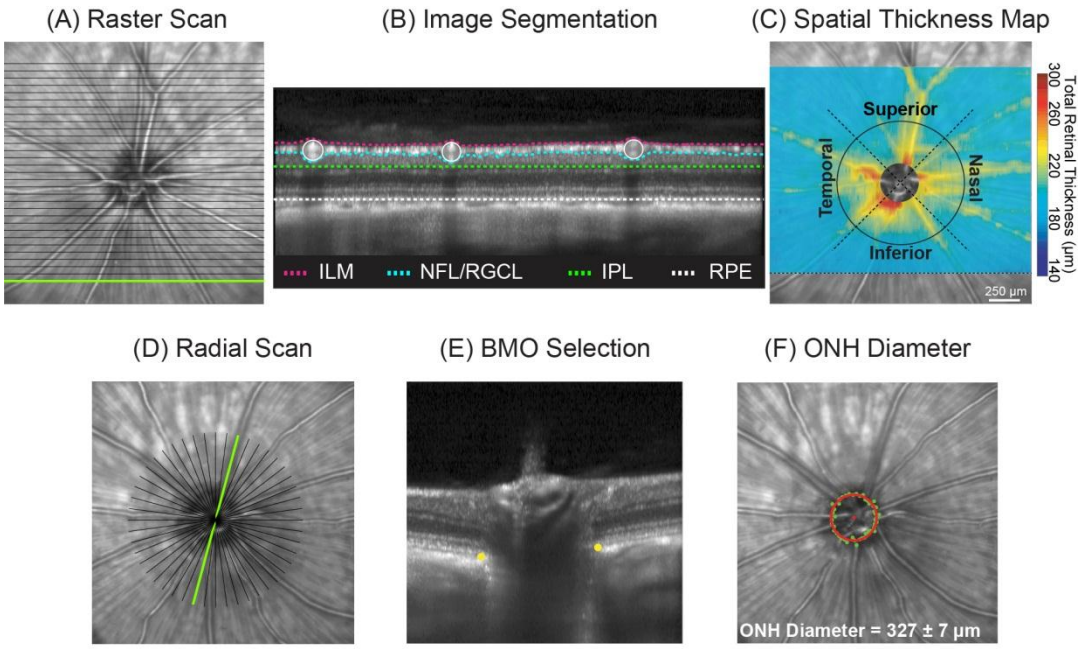

Figure 7.1: Measuring retinal structures from SD-OCT images in Brown Norway rats (n = 18 rats).

(A) Horizontal raster retinal scans centered on the optic nerve head were acquired in all eyes. The green line indicates the location of the b-scan shown in (B). **(B)** A semi-automated segmentation algorithm was used to delineate the inner limiting membrane (ILM, pink dashed line), nerve fiber layer/retinal ganglion cell layer (NFL/RGCL; blue dashed line), inner plexiform layer (IPL; green dashed line), retinal pigmented epithelium (RPE; white dashed line), and blood vessels (white circles). **(C)** Spatial thickness maps were generated using bilinear interpolation of thicknesses across individual B-scans. Circumpapillary scan (black circle; radius = 0.5 mm) were divided into superior, nasal, inferior, and temporal retinal quadrants. **(D)** Radial retinal scans were acquired to delineate the end of the retina towards the optic nerve head region (e.g. Bruch's membrane opening, BMO). The green line shows the location of the B-scan shown in (E). **(E)** The yellow dots show the annotations of Bruch's membrane opening (BMO). **(F)** Optic nerve head (ONH) diameter was measured from a best-fit circle through the annotations of the BMO.

7.4.2 In-vivo Retinal Thickness Estimates in a Rat Model of Glaucoma

IOP was surgically elevated by injecting hypertonic saline solution into one eye from six animals.[56] IOP was regularly measured in un-anesthetized animals with calibrated TonoLab rebound tonometers. The volumetric image datasets described above served to establish baseline thickness estimates prior to elevating IOP. Similar volumetric image data sets were acquired from these animals 5 to 10 weeks after elevating IOP. Ultrasonic A-scans and corneal topographies were acquired at the end of all imaging sessions to generate schematic model eyes and compensate for image lateral magnification as previously described.[246] Images were segmented, however, for rats with experimental glaucoma, only NFL/RGCL + IPL and total retinal thickness estimates are reported. Lastly, the size of the optic nerve head was also measured as the diameter of a circle best-fitted to Bruch's membrane opening.

Transverse sections of the optic nerve were used to qualitatively assess the amount of damage caused by the elevation in IOP using methods described by Jia and colleagues.[247] Animals were euthanized and their optic nerves were preserved with a mixture of 4% paraformaldehyde and 5% glutaraldehyde. Nerves were post-fixed in 2% osmium tetroxide, dehydrated in acetone, and embedded in Embed 812 resin (Electron Microscopy Sciences, Hatfield, PA). One micron thick sections were acquired 2 mm away from the globe and were stained with toluidine blue. Optic nerve sections were assessed under a light microscope and graded by an observer using a previously establish grading protocol.[247] Grade 1 indicated that the nerve is normal; progressively higher grades indicated a move from focal axonal degeneration (Grade 2) to degenerating axons found throughout the optic nerve (Grade 5). Linear regression analysis was then performed to correlate the *in vivo* estimates of optic nerve head diameter (by optical coherence tomography) with the optic nerve grade (acquired by histology).

7.5 Results

7.5.1 In-vivo Retinal Thickness Estimates in Normal Rats

In normal animals, the average scanned retinal area (30° x 25°) was 1.8 by 1.5 mm. Thickness estimates decreased as a function of distance away from the optic nerve head center. For example, NFL/RGCL thickness measured from the smallest circumpapillary scans (radius = 0.3 mm; thickness = 48 ± 17 µm) were 38% thicker than the measurements from the largest circumpapillary scans (radius = 0.6 mm; thickness = 30 ± 6 µm; **Figure 7.2**). Lastly, blood vessels made up less than 50% of circumpapillary scans with radii between 0.5 to 0.6 mm (**Figure 7.2**). NFL/RGCL thickness 0.5 mm away from the optic nerve head center were significantly thicker when blood vessels were included in the calculation (41 ± 3 µm; 95% CI: 39 – 43 µm) than when they were excluded (35 ± 2 µm; 95% CI: 33 – 36 µm; $P < .001$; **Figure 7.2**). Similarly, NFL/RGCL + IPL thickness was significantly thicker when blood vessels were included in thickness estimates (84 ± 3 µm; 95% CI: 82 – 86 µm) than when they were excluded (81 ± 3 µm; 95% CI: 79 – 83 µm; $P = .002$; **Figure 7.2**).

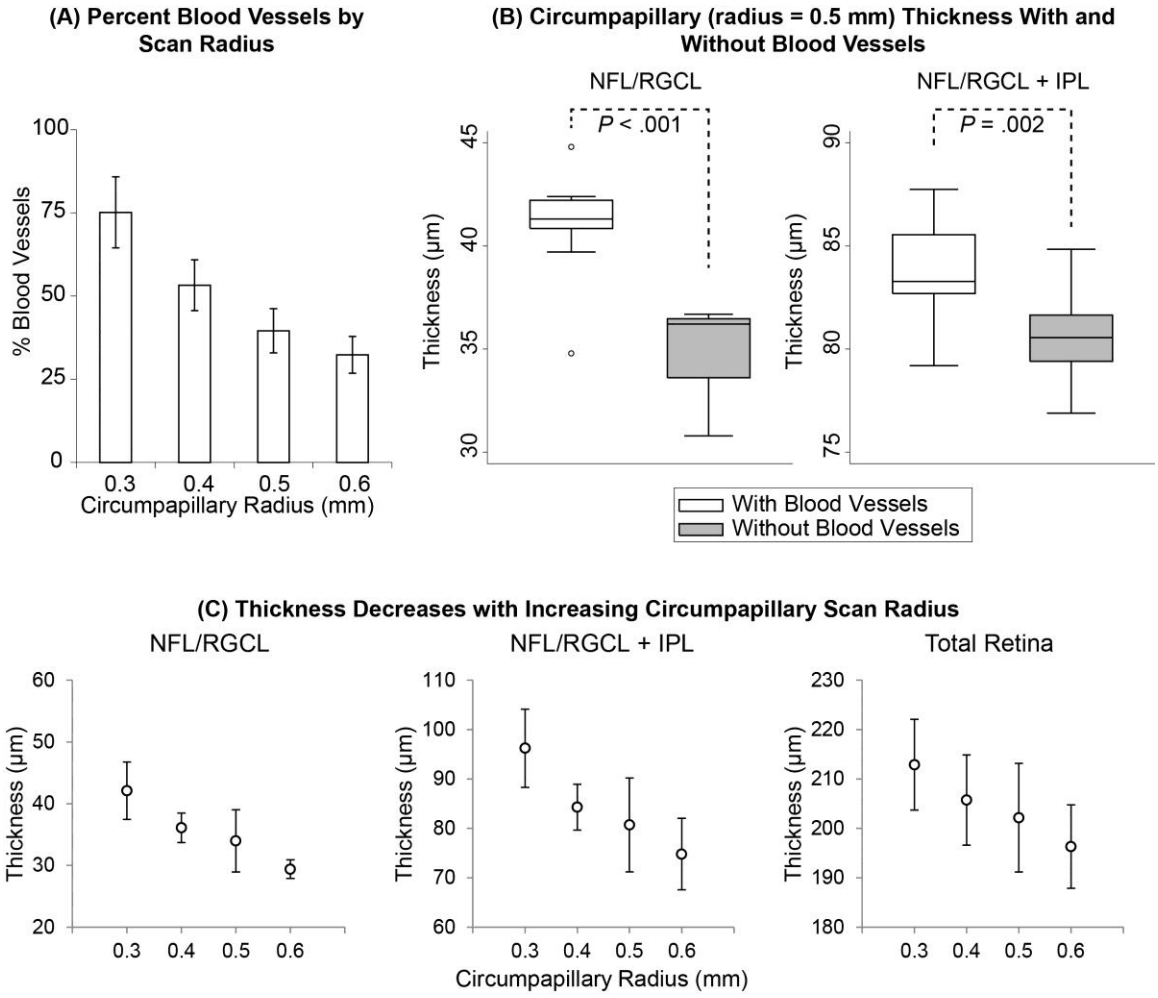

Figure 7.2: Quantification of circumpapillary retinal thickness in normal adult Brown Norway rats.

(A) Calculated blood vessel contribution in circumpapillary scans with a 0.3 to 0.6 mm radius. A circumpapillary scan with a 0.3 mm radius is composed of 75% blood vessels and the percentage of blood vessels decreased with increasing radii. **(B)** Distribution of nerve fiber layer and retinal ganglion cell layer (NFL/RGCL) and NFL/RGCL plus inner plexiform layer (NFL/RGCL + IPL) thickness measurements acquired with and without blood vessels from circumpapillary scans with a 0.5 mm radius. The box is the interquartile range (IQR), the horizontal line inside the box is the median, the whiskers are data that are within ±1.5 x IQR, and open circles are outliers. Blood vessels

significantly increased NFL/RGCL and NFL/RGLC + IPL thickness measurements. **(C)** Plotting the mean (±SD) thickness measured from circumpapillary scans with varying radii to show that thickness decreased with increasing circumpapillary scan radii.

Thickness difference between eyes of the same animal and thickness estimates by retinal quadrant (Nasal, Inferior, Superior, and Temporal) were then assessed from the circumpapillary scan with a 0.5 mm radius. This specific circumpapillary scan was chosen because retinal structures (non-blood vessel regions) comprised more than 50% of the scan. Retinal thickness measurements between left and right eyes of normal adult Brown Norway rats were not significantly different. For example, the 95% confidence interval for NFL/RGCL thickness measurements in 19 left eyes ranged between 33 – 38 µm and was 34 – 39 µm (P = .5; Paired t-test) in right eyes. Left and right eye NFL/RGCL+IPL thickness measurements (95% CI: 78 – 85 µm vs. 79 – 86 µm; P = .5), and total retinal thickness measurements (95% CI: 196 – 207 µm vs. 199 – 209 µm; P = .3) were also not significantly different between eyes (**Figure 7.3**). One eye from each animal was then randomly selected to quantify retinal quadrant differences in normal eyes. In normal rats, mean temporal NFL/RGCL thickness (39 ± 6 µm) was significantly thicker (Post-hoc Tukey's HSD Test at the .05 level of significance) than inferior (33 ± 5 µm) and superior (31 ± 5 µm) NFL/RGCL thickness (**Figure 7.4**).

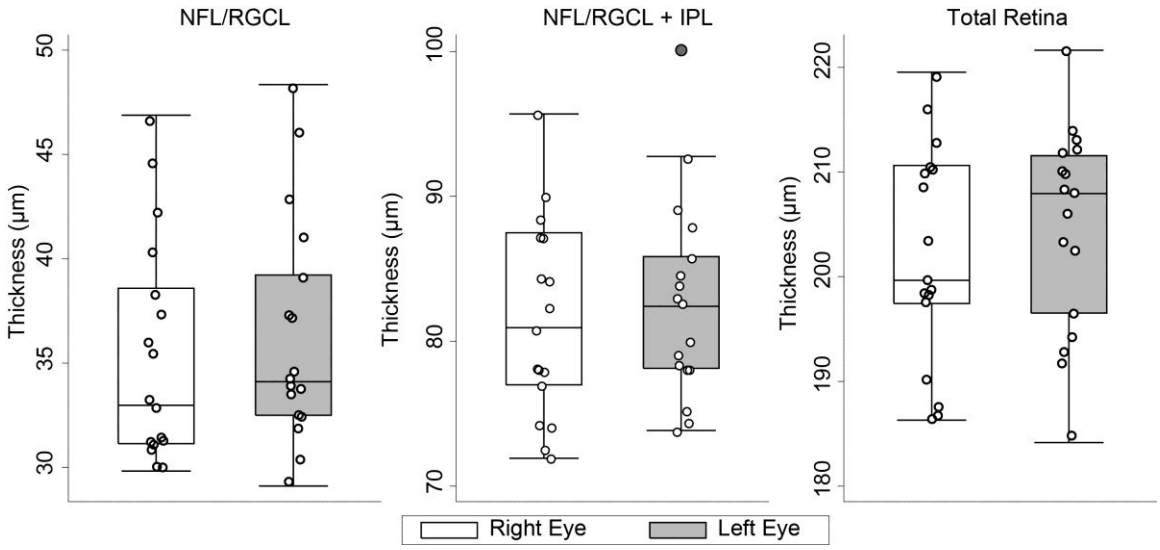

Figure 7.3: Distribution of left and right eye retinal thickness measurements in normal adult Brown Norway rats (n = 19 animals; 38 eyes).

The white and gray boxes are the interquartile range (IQR), the horizontal line in the middle of the boxes is the median, vertical lines (e.g. whiskers) are data within ±1.5 x IQR, points outside the whiskers are outliers. The raw thickness measurements acquired per animal are indicated by the open circles. Left and right eye thickness were not significantly different for nerve fiber layer and retinal ganglion cell layer (NFL/RGCL) thickness, NFL/RGCL plus inner plexiform layer (NFL/RGCL + IPL) thickness, or total retinal thickness.

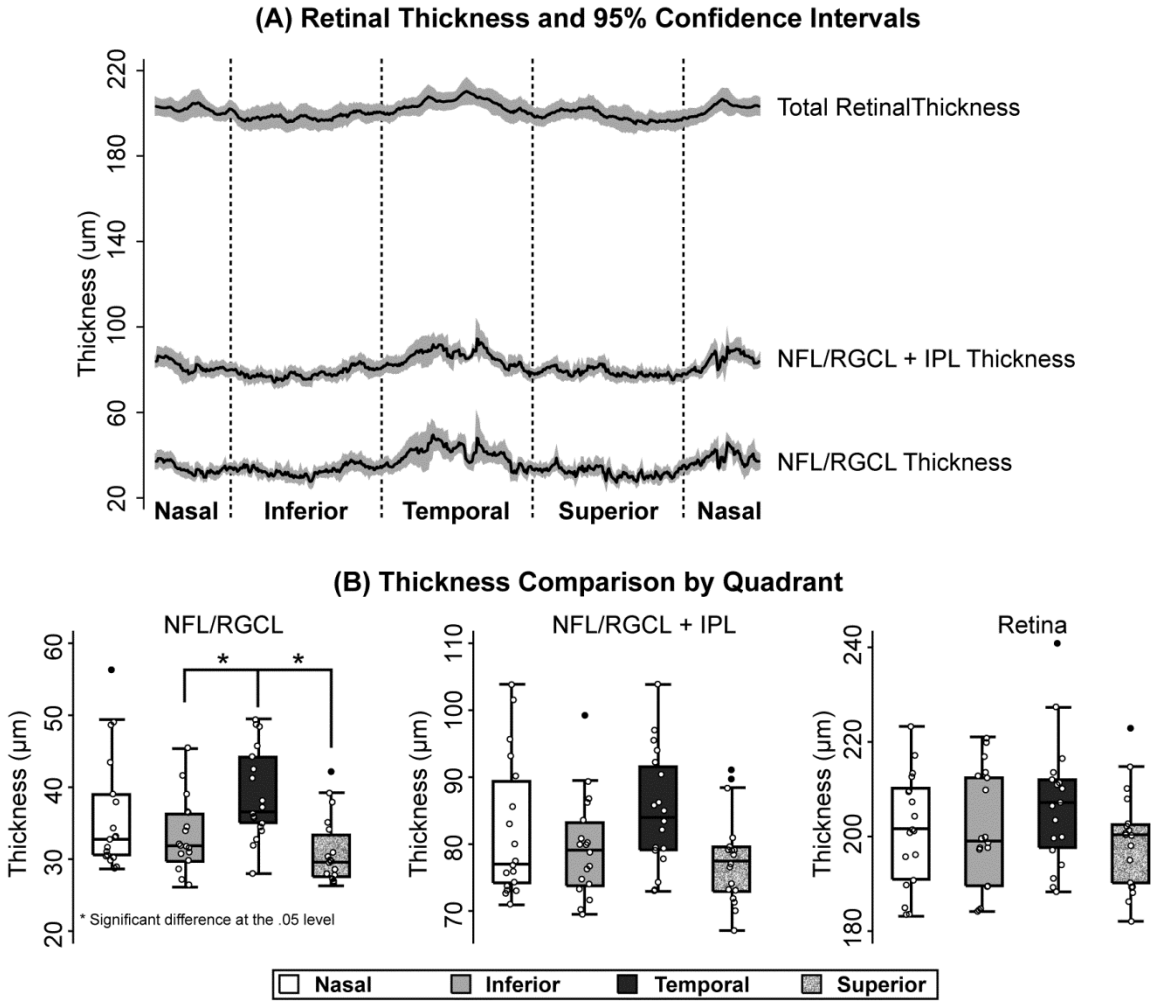

Figure 7.4: Circumpapillary thickness scans (radius = 0.5 mm) in normal aged Brown Norway rats (n = 18 eyes).

(A) Mean (black line) NFL/RGCL, NFL/RGCL + IPL and total retinal thickness (solid black line) and 95% confidence intervals (gray shaded areas) are plotted. **(B)** Distribution of thickness measurements by retinal quadrant. The open circles are the mean thickness measurements for each animal, the boxes are the interquartile range (IQR) of the data, the horizontal line inside the box is the median, the vertical lines (e.g. whiskers) are ±1.5 X IQR, filled in points are outliers. These box-plots show the comparison of thickness by retinal quadrant. Mean temporal NFL/RGCL thickness (39 ± 6 µm) was significantly thicker (Post-hoc Tukey's HSD Test at the .05 level of

significance) than inferior (33 ± 5 μm) and superior (31 ± 5 μm) NFL/RGCL thickness, but was not significantly different from the nasal quadrant (36 ± 8 μm; $P > .05$).

7.5.2 In-vivo Retinal Thickness Estimates in a Rat Model of Glaucoma

In the rat model of glaucoma, post-injection IOP was significantly higher (95% CI: 21 – 43 mm Hg) than pre-injection measurements (95% CI: 17 – 20 mm Hg; *P* = .02; Paired t-test; **Figure 7.5**). Also, the anterior chamber depth was significantly deeper in glaucoma eyes (1.18 to 2.07 mm) compared to baseline measurements (95% CI: 0.82 to 0.97 mm; *P* = .002; **Figure 7.5**). Longer eyes were also measured in experimental glaucoma eyes compared to baseline measurements (95% CI: 6.70 to 7.87 mm vs. 6.07 to 7.18 mm; *P* = .01; Paired t-test). In-vivo NFL/RGCL + IPL and total retinal thickness estimates decreased as a result of the elevation in IOP. These thickness estimates were only calculated form the circumpapillary retinal scans with the largest radii (the 0.5 mm and 0.6 mm radii) because some of the animals had severe optic nerve head cupping that made it difficult to measure thickness with the smaller radii. **Figure 7.6** shows that there no statistically significant difference in NFL/RGCL + IPL thickness between the experimental glaucoma eyes as compared to baseline values for the current sample size. For example, NFL/RGCL + IPL thickness at baseline measured with the 0.5 mm circumpapillary scan radius for these six animals was 83 ± 10 µm (95% CI: 72 – 94 µm) and at the end of the imaging session it was 69 ± 17 µm (95% CI: 51 – 86 µm; *P* = 0.09, Paired t-test ; **Figure 7.6** and **Figure 7.7**).

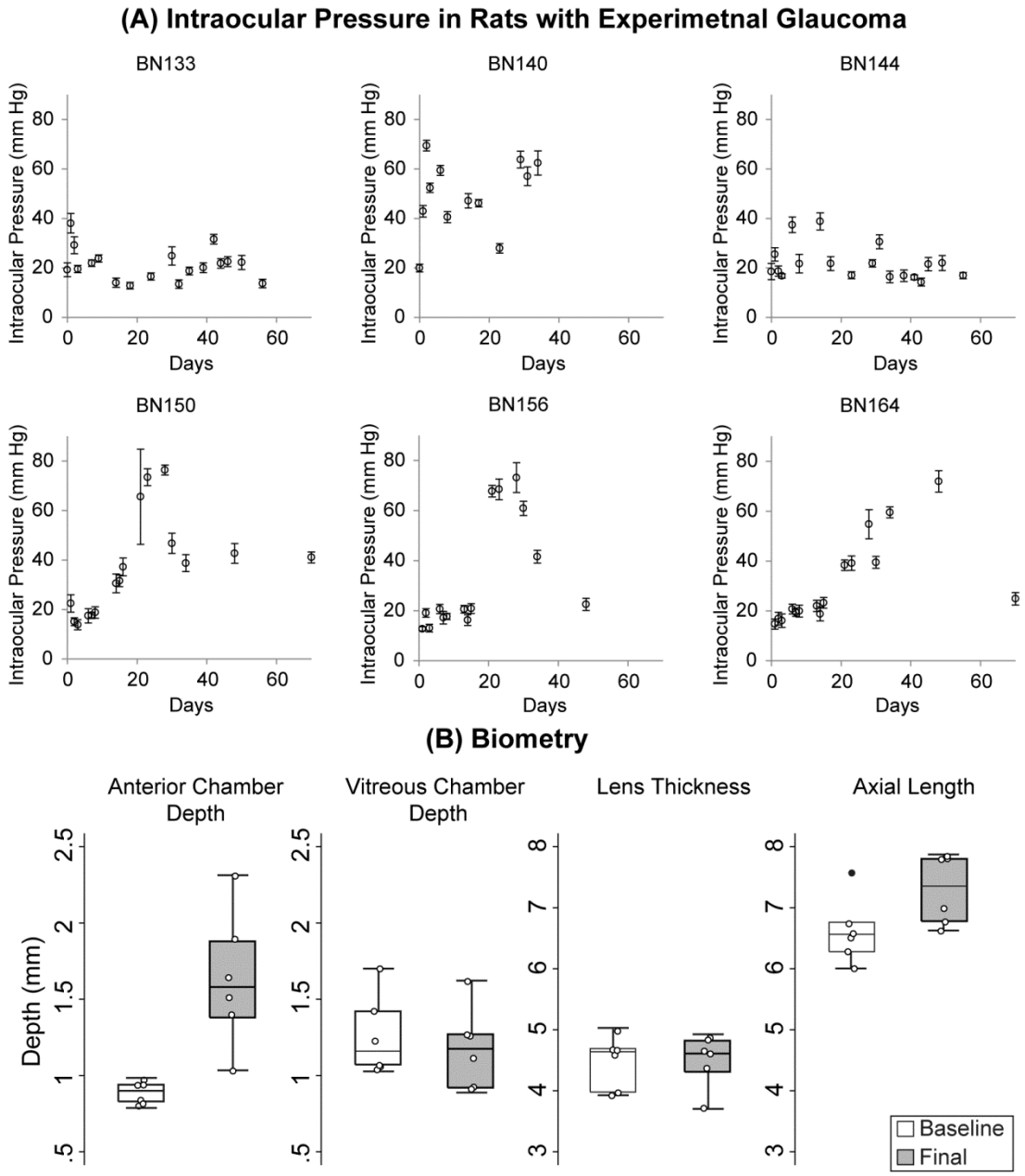

Figure 7.5: Mean intraocular pressure (IOP) and biometry changes after surgically elevated IOP in 6 animals.

(A) Mean (±SD) IOP measured after surgically elevating IOP in six Brown Norway rats. **(B)** Distribution of biometric measurements before and after surgical elevation of IOP in six Brown Norway rats. The open circles are the mean biometric measurements for each animal, boxes are the interquartile range (IQR) of the data, the horizontal line inside the

box is the median, vertical lines (e.g. whiskers) are ±1.5 X IQR, filled in points are outliers. Anterior chamber depth was significantly greater in experimental glaucoma eyes compared to baseline measurements (95% CI: 1.18 to 2.07 mm vs. 0.82 to 0.97 mm; *P* = .001). Longer eyes were measured in experimental glaucoma eyes compared to baseline measurements (95% CI: 6.70 to 7.87 mm vs. 6.07 to 7.18 mm; *P* = .01). All other biometric parameters (vitreous chamber depth [*P* = .23] and lens thickness [*P* = .91]) were not significantly different between normal eyes and eyes with experimental glaucoma.

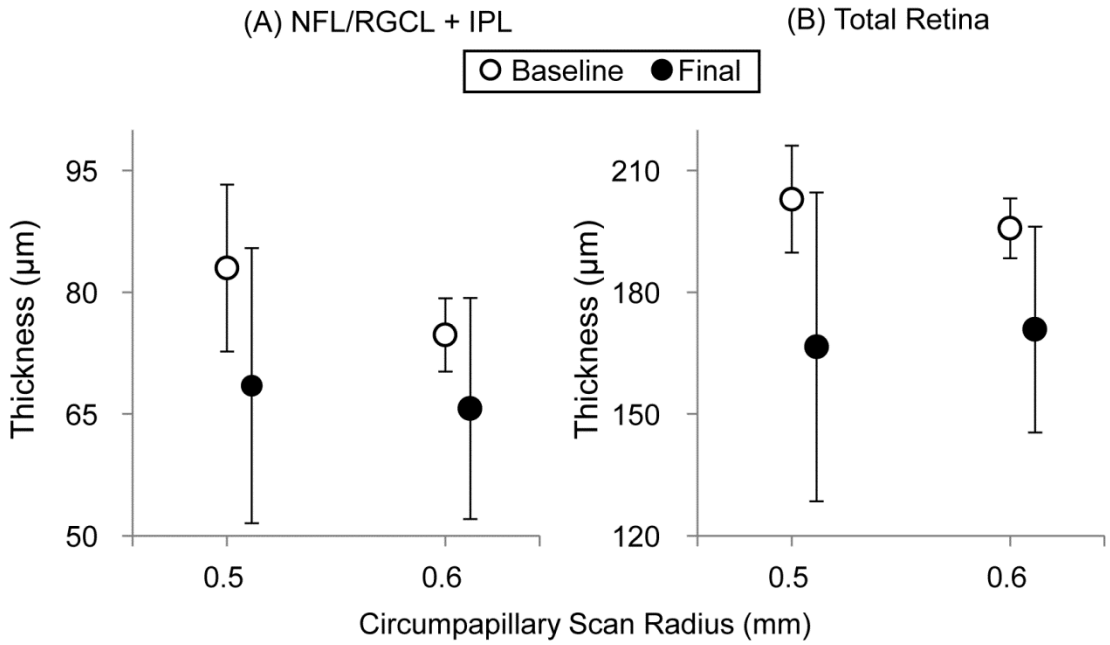

Figure 7.6: Retinal thickness in experimental glaucoma eyes for different circumpapillary scan radii.

Filled in black circles indicate the mean (±SD) thickness estimates acquired during the baseline imaging sessions; open circles indicate the mean (±SD) acquired at the final imaging session. **(A)** Nerve fiber layer/retinal ganglion cell layer and inner plexiform layer (NFL/RGCL + IPL) thickness decreased by 12% – 17% from baseline thickness estimates. **(B)** Total retinal thickness decreased from baseline thickness estimates by 12% – 18%.

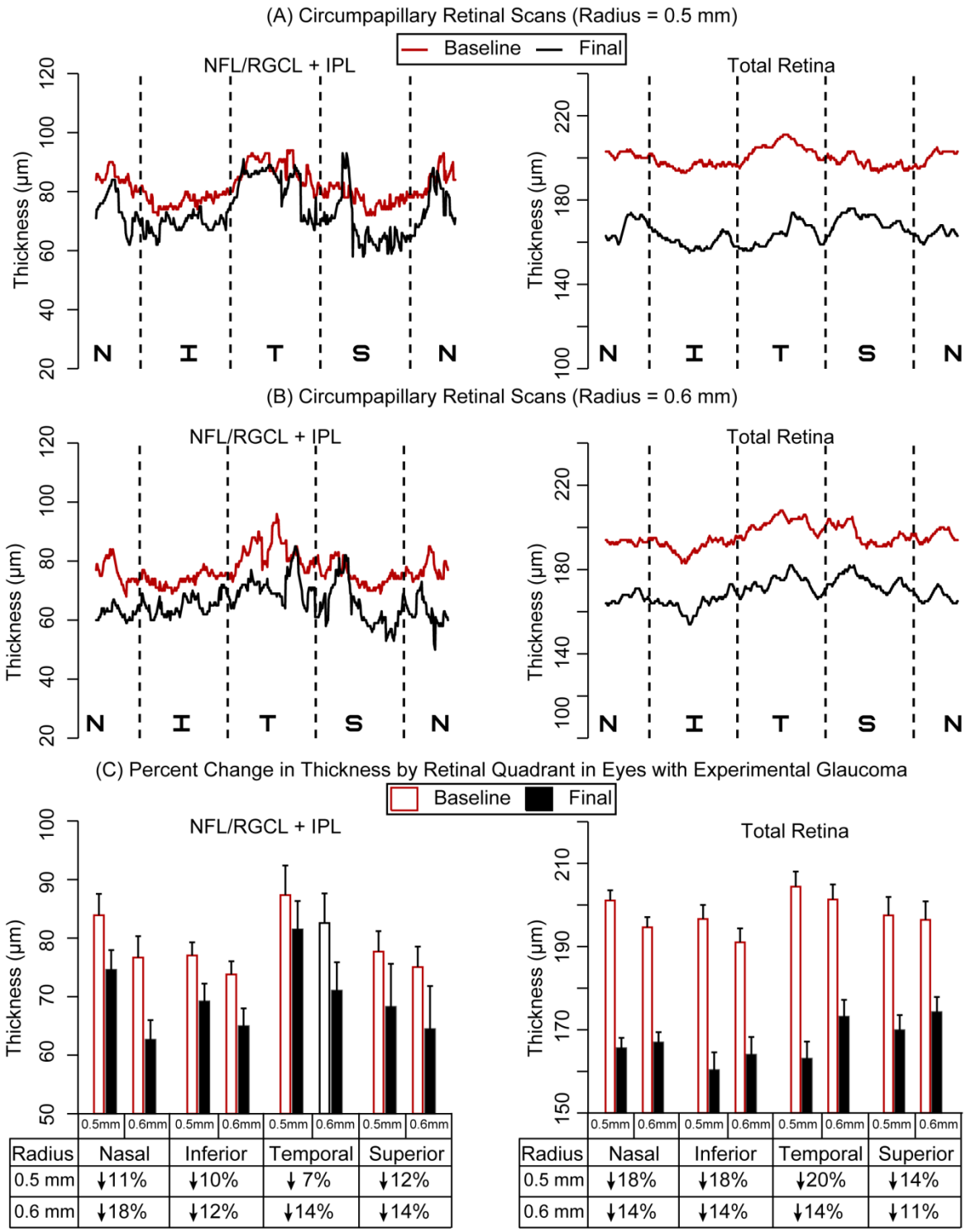

Figure 7.7: Circumpapillary retinal scans from six rats with experimental glaucoma.

(A) Plotting the baseline (red line) and final (black line) thickness measurements for circumpapillary retinal scans with a 0.5 mm radius. **(B)** Plotting the baseline (red line) and final (black line) thickness measurements for circumpapillary retinal scans with a 0.6 mm radius. **(C)** Nerve fiber layer/retinal ganglion cell layer and inner plexiform layer (NFL/RGLC + IPL) thickness and total retinal thickness decreased equally in all quadrants after elevating IOP irrespective of the size of the circumpapillary retinal scan.

The optic nerve head prior to surgically elevating IOP had a mean diameter of 335 µm (95%CI: 292 – 377 µm). There was a large variation in the size of the optic nerve head after 5 to 10 weeks of exposure to elevated IOP (95% CI: 289 – 770 µm; **Figure 7.8**). The diameter of the optic nerve head correlated better with maximum IOP measured over the course of the experiment (r^2 = 0.48; *P* = .012) than with the mean IOP (r^2 = 0.19; *P* = .15). Histological optic nerve sections from the experimental glaucoma eyes had a mean grade of 4.25 ± 1.17, indicating that there was a high degree of damage throughout the nerve (**Figure 7.8**). Lastly, greater optic nerve damage was positively correlated with larger optic nerve head diameters assessed from optical coherence tomography images (r^2 = 0.48; *P* = .013; **Figure 7.8**).

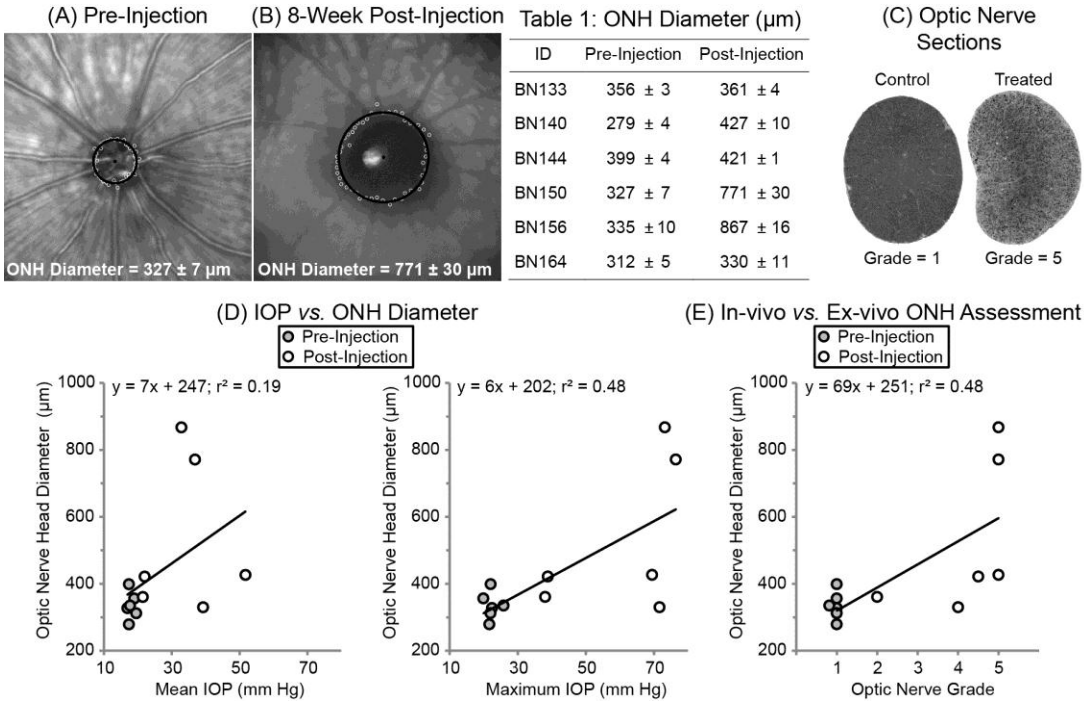

Figure 7.8: Measuring the optic nerve head (ONH) size in normal eyes and eyes with experimental glaucoma.

(A and B) Bruch's membrane opening was delineated from SD-OCT images and superimposed on the scanning laser ophthalmoscope image (white points). The size of the optic nerve head was defined as the diameter of the best-fitting circle though Bruch's membrane opening (black circle). The inserted table shows that the diameter of the optic nerve head at baseline was 335 µm (95% CI: 292 – 377 µm) and the size of the optic nerve head largely varied by the end of the experiment (95% CI: 289 – 770 µm), with a tendency towards being larger after being exposed to high intraocular pressure (IOP). **(C)** Optic nerve cross-sections in control eyes had a grade of 1 (normal) and eyes with elevations in IOP had a maximum grade of 5, indicating damage throughout the nerve (e.g. gliosis and collapse myelin sheaths). **(D)** There was a moderate linear relationship (r^2 = 0.48; *P* = .012) between the maximum IOP and the ONH diameter. **(E)** There was also a moderate linear relationship (r^2 = 0.48; *P* = .013) between histological assessment of the optic nerve and ONH diameter.

7.6 Conclusion

In normal adult Brown Norway rats, NFL/RGCL thickness estimates measured from circumpapillary scans (radius = 0.5 mm) were significantly thicker in the temporal retinal quadrant than either the superior or inferior retinal quadrants, but was not different from the nasal quadrant. In rats with experimental glaucoma, NFL/RGCL + IPL thickness and total retinal thickness decreased equally in all retinal quadrants. These results were further supported by analysis of histological optic nerve sections that showed damage throughout the nerve. Furthermore, maximum IOP and the histological assessment of the optic nerve damage were positively correlated with in-vivo estimates of optic nerve head diameter. These results suggest that the measured in-vivo structural changes correlate well with the elevation in IOP and are not simply a magnification artifact.

Retinal thickness estimates were calculated from scaled circumpapillary scans of various sizes. These circumpapillary scans were computationally generated because the built-in scan on the Spectralis HRA+OCT has a fixed size that is designed for using with a human eye. The 12° circumpapillary scan on the Spectralis HRA + OCT corresponds to a 391.5 µm scan radius in an adult normal Brown Norway rat (calculated from our previously published results that indicate there are 65 µm per degree[246]). The results shown in **Figure 7.2** indicate that blood vessels make up more than 60% of a circumpapillary scan with a 400 µm radius. This is important to keep in mind when selecting where measurements are taken because blood vessels can significantly increase thickness estimates (**Figure 7.2**). For example, NFL/RGCL was 15% thicker with blood vessels than without (41 ± 3 µm vs. 35 ± 2 µm; P <.001). The 12° circumpapillary scan is also not optimal for the rat eye because the optic nerve head diameter in some of the animals with high elevations in IOP were as large as ~700 µm.

From the circumpapillary retinal scans we found that the temporal NRL/RGCL in normal adult Brown Norway rats was significantly thicker than the inferior or superior quadrants. These results show that there is an agreement between the location of thickest NFL/RGCL and studies that have shown that the highest density of retinal ganglion cells is in the temporal retinal quadrant. For example, histological studies report that the temporal or superotemporal quadrants have the highest retinal ganglion cell densities.[45, 46, 48, 215] Work by Danias contradicts these previous studies and showed that the highest density of retinal ganglion cells was not always in the same retinal quadrants between animals.[52] Danias suggested that their results were different from previous studies because they worked with an outbred strain of rats (Wistar albino rats). However, a study by Nadal-Nicolas and colleagues showed that the number of retinal ganglion cells is not different between inbred pigmented rats or outbred albino rats.[248] They also suggested that the difference may be related to the type of staining used to identify retinal ganglion cells; Danias and colleagues used Fluorogold to retrograde label retinal ganglion cells, while some of the older studies used horseradish peroxidase whose labeling capabilities are variable. Two recent studies used Fluorogold and Brn3a to count retinal ganglion cells and these studies support the earlier findings that the temporal retina has the highest density of retinal ganglion cells.[51, 249] Another probable explanation for the differences between studies may be related to image analysis techniques employed to automatically quantify the retinal ganglion cell population. For example, Salinas-Navarro and colleagues filtered their images several times to even out background illumination and to remove small artifacts and noise, whereas Danias filtered the image once with a high-pass filter and then threshold the image to detect the edges of the cells. The additional image filtering performed by Salinas-Navarro may have enhanced the ability to detect retinal ganglion cells.

The mean optic nerve head diameter in normal adult rats was 334 µm and this measurement agrees well with previous results.[226, 246] In rats with experimental glaucoma, maximum IOP measured over the course of the experimental study correlated well with larger optic nerve heads (**Figure 7.8**). Furthermore, these larger optic nerve heads had damage (e.g. collapse myelin sheaths and gliosis) throughout optic nerve cross-sections (**Figure 7.8**), further supporting the idea that this structural damage is a result of the elevation in IOP. Lastly, in rats with experimental glaucoma, the in-vivo NFL/RGCL + IPL and total retinal thickness estimates decreased equally in all quadrants (**Figure 7.7**). A limitation of the current study is that outer retinal thickness decreased by approximately 14%, indicating retinal damage due to ischemia occurred in animals with high elevations in IOP. This high elevation in IOP resulted in damage throughout the optic nerve and retina. One of the biggest challenges with this current study is that elevating IOP by injecting hypertonic saline into an episcleral vein is a difficult task. It is especially difficult to induce mild chronic elevations in IOP using Morrison's model and this is illustrated in **Figure 7.5A** where some animals had IOP in the upper 60 mm Hg. Future studies should aim for mild to moderate elevation in IOP to determine if there are regional differences in the amount of thickness changes brought upon by the elevation in IOP. Morrison noted that "eyes with less than 100% damage showed focal axonal degeneration, and that this was primarily located in the superior temporal region of the nerve."[56] Also, WoldeMussie and colleagues showed that more retinal ganglion cells were lost in the superior-half of the retina than inferior-half of the retina in a laser photocoagulation rodent model of glaucoma.[250] Future studies should determine if this regional change brought upon by the elevation in IOP is quantifiable by in-vivo optical coherence tomography imaging.

Chapter Eight

General Conclusions

The first objective of this dissertation was to study the relationship between IOP and mean arterial pressure in Brown Norway rats. We specifically investigated if the circadian rhythm of IOP free runs in continuous dim light and the circadian phase relationship between IOP and mean arterial pressure when animals are housed in standard light-dark conditions (12 hours of light / 12 hours of darkness). The experiments and results from this first specific aim are a significant contribution because they showed, for the first time, that the circadian rhythm of IOP free-runs in continuous dim light and that blood pressure and IOP do not peak at the same time in standard light-dark conditions. These results highlight that the Brown Norway rat is a useful model for studying the role of various compartmental pressures on glaucoma and their highly rhythmic diurnal physiological patterns make this an excellent model to study the circadian biology of the eye and glaucoma.

The second objective of this dissertation was to use spectral domain optical coherence tomography (SD-OCT) to quantify spatial retinal structural changes in rats with experimental glaucoma. There are several challenges to consider when interpreting thickness measurements from SD-OCT images, including: scan placement/centration, axial length of the eye (e.g. correction of image lateral magnification), image quality, contribution of non-neuronal components (blood vessels and glial tissue), instrument and examiner factors among others. As part of this dissertation, the experimental goals were to address the following challenges: (1) to quantify the effects of ocular–instrument realignment and image quality on measurements of retinal thickness from SD-OCT imaging in the rat eye; and (2) to develop a schematic model of the rat eye from *in vivo* axial biometric measurements to compensate for image lateral magnification. Addressing these challenges enabled the quantification of the structural changes in a rat model of experimental glaucoma. The results from this second objective are a significant contribution because we showed that we can reliably scan the same retinal location

between imaging sessions and that estimates of retinal thickness and optic nerve head size are in good agreement with previously reported measurements after compensating for image lateral magnification. Also, the results from this second objective are a significant contribution because we showed that *in vivo* SD-OCT thickness measurements of the nerve fiber layer/retinal ganglion cell layer correlate well with histological studies showing that the highest density of retinal ganglion cells are located in the superior-temporal retinal quadrant. We also showed that retinal thickness measured *in vivo* by SD-OCT imaging decreased in a rat model of experimental glaucoma even when biometric changes induced by disease are taken into account to compensate for lateral magnification. Furthermore, this *in vivo* measurement correlated well with histological assessments of optic nerve damage.

Conclusion and Future Direction

Glaucoma is the second leading cause of blindness worldwide and elevated IOP is the only treatable risk factor. Animal models of glaucoma have improved our understanding of the pathophysiology of glaucomatous damage and are useful for evaluating new therapeutic drugs. There are several important challenges that need to be addressed with any of these animal models of glaucoma, including having a reliable method of measuring IOP and having methods of quantifying structural damage caused by the elevation in IOP. In this dissertation, reliable IOP measurements were acquired with the TonoLab rebound tonometer and showed that the circadian rhythm of IOP free runs in constant dim light. Future work should quantify the circadian rhythm of IOP in a rat model of glaucoma. In particular, it would be interesting to determine how the free-running IOP rhythm contributes to the amount of glaucomatous damage or if glaucoma has a direct impact on the circadian rhythm of IOP. For example, the results from our studies suggest that the circadian rhythm of IOP may be locally regulated, perhaps

within the eye. These types of studies would benefit from telemetric systems that automatically measure IOP. These telemetric systems could shed light on differences between the circadian rhythm of IOP in normal and glaucomatous eye and whether it is diagnostically beneficial to measure the circadian rhythm of IOP for detection glaucomatous damage. Also, it is important to better understand the role of compartmental pressures (e.g. blood pressure, intracranial pressure) on glaucoma. In this dissertation, we showed that in normal rats housed in standard light-dark conditions, the circadian rhythm of IOP is out of phase with the circadian rhythm of mean arterial pressure. Future studies should determine the impact of the circadian phase relationship between IOP and mean arterial pressure on the glaucomatous damage (e.g. changes in the optic nerve head and retinal thickness).

In vivo quantification of structural changes in ocular tissue may be diagnostically advantageous and may shed light on the pathogenesis of glaucomatous optic neuropathy. In this dissertation, we presented the analytical tools needed to scan the same retinal location between imaging sessions and how to compensate for image lateral magnification. These tools were used to quantify structural changes in a rat model of glaucoma and showed that retinal thickness decreased and that this *in vivo* measurement correlated well with histological assessments of optic nerve damage. Future studies should quantify changes in optic nerve head diameter and retinal thickness associated with mild to moderate elevations in IOP. Also, previous studies in humans have shown that there are age related changes in the nerve fiber layer thickness.[251] The tools presented in this dissertation can be used in the future to determine these age related changes in Brown Norway rats.

Rats are a good model for studying circadian rhythms because there is a large body of literature currently available describing the circadian rhythm of many physiological and behavioral parameters in these animals. However, a shortcoming of

using rats as an experimental model of glaucoma is that they do not have a lamina cribrosa. The next logical experiment would be to evaluate these circadian rhythms of IOP and blood pressure, as well as the *in vivo* structural changes in an animal that has a lamina cribrosa, for example in the non-human primate, guinea pig, and tree-shrews. Specifically, a testable hypothesis that arises from the work presented in this dissertation is that the circadian rhythm of IOP (i.e., amplitude and rhythmicity) changes as a function of glaucomatous disease severity. It is likely that a robust IOP rhythm is maintained during the early stages of the disease, but that this rhythm free-run as the disease progresses, and possibly, the rhythm becomes ultradian (e.g., having a period smaller than 24 hours) as the disease reaches its end stage (e.g. blindness). This hypothesis could first be tested by measuring the circadian rhythm of IOP for several weeks after transecting both optic nerves in an animal.

References

1. Comparison of glaucomatous progression between untreated patients with normal-tension glaucoma and patients with therapeutically reduced intraocular pressures. Collaborative Normal-Tension Glaucoma Study Group. *Am J Ophthalmol.* 1998;126:487-497.
2. Higginbotham EJ, Gordon MO, Beiser JA, et al. The Ocular Hypertension Treatment Study: topical medication delays or prevents primary open-angle glaucoma in African American individuals. *Arch Ophthalmol.* 2004;122:813-820.
3. Leske MC, Heijl A, Hussein M, et al. Factors for glaucoma progression and the effect of treatment: the early manifest glaucoma trial. *Arch Ophthalmol.* 2003;121:48-56.
4. Harwerth RS, Wheat JL, Fredette MJ, et al. Linking structure and function in glaucoma. *Prog Retin Eye Res.* 2010;29:249-271.
5. Fechtner RD, Weinreb RN. Mechanisms of optic nerve damage in primary open angle glaucoma. *Surv Ophthalmol.* 1994;39:23-42.
6. Flammer J. The vascular concept of glaucoma. *Surv Ophthalmol.* 1994;38 Suppl:S3-6.
7. Pillunat LE, Anderson DR, Knighton RW, et al. Autoregulation of human optic nerve head circulation in response to increased intraocular pressure. *Exp Eye Res.* 1997;64:737-744.
8. Quigley HA. Experimental glaucoma damage mechanism. *Arch Ophthalmol.* 1983;101:1301-1302.
9. Quigley HA, Addicks EM, Green WR, et al. Optic nerve damage in human glaucoma. II. The site of injury and susceptibility to damage. *Arch Ophthalmol.* 1981;99:635-649.

10. Crawford Downs J, Roberts MD, Sigal IA. Glaucomatous cupping of the lamina cribrosa: a review of the evidence for active progressive remodeling as a mechanism. *Exp Eye Res.* 2011;93:133-140.

11. Anderson DR. Ultrastructure of human and monkey lamina cribrosa and optic nerve head. *Arch Ophthalmol.* 1969;82:800-814.

12. Quigley HA, Addicks EM. Regional differences in the structure of the lamina cribrosa and their relation to glaucomatous optic nerve damage. *Arch Ophthalmol.* 1981;99:137-143.

13. Torti C, Povazay B, Hofer B, et al. Adaptive optics optical coherence tomography at 120,000 depth scans/s for non-invasive cellular phenotyping of the living human retina. *Opt Express.* 2009;17:19382-19400.

14. Sehi M, Grewal DS, Sheets CW, et al. Diagnostic ability of Fourier-domain vs time-domain optical coherence tomography for glaucoma detection. *Am J Ophthalmol.* 2009;148:597-605.

15. Wu H, de Boer JF, Chen TC. Diagnostic capability of spectral-domain optical coherence tomography for glaucoma. *Am J Ophthalmol.* 2012;153:815-826 e812.

16. Tielsch JM, Sommer A, Katz J, et al. Racial variations in the prevalence of primary open-angle glaucoma. The Baltimore Eye Survey. *JAMA.* 1991;266:369-374.

17. Rudnicka AR, Mt-Isa S, Owen CG, et al. Variations in primary open-angle glaucoma prevalence by age, gender, and race: a Bayesian meta-analysis. *Invest Ophthalmol Vis Sci.* 2006;47:4254-4261.

18. Vajaranant TS, Wu S, Torres M, et al. The changing face of primary open-angle glaucoma in the United States: demographic and geographic changes from 2011 to 2050. *Am J Ophthalmol.* 2012;154:303-314 e303.

19. Nguyen RL, Raja SC, Traboulsi EI. Screening relatives of patients with familial chronic open angle glaucoma. *Ophthalmology.* 2000;107:1294-1297.

20. World Health Organization. Vision 2020 Action Plan 2006 - 2010; 37-39.

21. Quigley HA, Broman AT. The number of people with glaucoma worldwide in 2010 and 2020. *Br J Ophthalmol.* 2006;90:262-267.

22. Brooks DE. Glaucoma in the dog and cat. *Vet Clin North Am Small Anim Pract.* 1990;20:775-797.

23. Rasmussen CA, Kaufman PL. Primate glaucoma models. *J Glaucoma.* 2005;14:311-314.

24. Pang IH, Clark AF. Rodent models for glaucoma retinopathy and optic neuropathy. *J Glaucoma.* 2007;16:483-505.

25. Roberts MD, Sigal IA, Liang Y, et al. Changes in the biomechanical response of the optic nerve head in early experimental glaucoma. *Invest Ophthalmol Vis Sci.* 2010;51:5675-5684.

26. Burgoyne CF, Downs JC, Bellezza AJ, et al. Three-dimensional reconstruction of normal and early glaucoma monkey optic nerve head connective tissues. *Invest Ophthalmol Vis Sci.* 2004;45:4388-4399.

27. Harwerth RS, Smith EL, 3rd, DeSantis L. Experimental glaucoma: perimetric field defects and intraocular pressure. *J Glaucoma.* 1997;6:390-401.

28. Ivers KM, Li C, Patel N, et al. Reproducibility of measuring lamina cribrosa pore geometry in human and nonhuman primates with in vivo adaptive optics imaging. *Invest Ophthalmol Vis Sci.* 2011;52:5473-5480.

29. Harwerth RS, Carter-Dawson L, Shen F, et al. Ganglion cell losses underlying visual field defects from experimental glaucoma. *Invest Ophthalmol Vis Sci.* 1999;40:2242-2250.

30. Quigley HA, Addicks EM, Green WR. Optic nerve damage in human glaucoma. III. Quantitative correlation of nerve fiber loss and visual field defect in glaucoma, ischemic neuropathy, papilledema, and toxic neuropathy. *Arch Ophthalmol.* 1982;100:135-146.

31. Sredar N, Ivers KM, Queener HM, et al. 3D modeling to characterize lamina cribrosa surface and pore geometries using in vivo images from normal and glaucomatous eyes. *Biomed Opt Express.* 2013;4:1153-1165.

32. Vilupuru AS, Rangaswamy NV, Frishman LJ, et al. Adaptive optics scanning laser ophthalmoscopy for in vivo imaging of lamina cribrosa. *Journal of the Optical Society of America A, Optics, image science, and vision.* 2007;24:1417-1425.

33. Harwerth RS, Crawford ML, Frishman LJ, et al. Visual field defects and neural losses from experimental glaucoma. *Prog Retin Eye Res.* 2002;21:91-125.

34. He Z, Nguyen CT, Armitage JA, et al. Blood pressure modifies retinal susceptibility to intraocular pressure elevation. *PloS one.* 2012;7:e31104.

35. Tielsch JM, Katz J, Sommer A, et al. Hypertension, perfusion pressure, and primary open-angle glaucoma. A population-based assessment. *Arch Ophthalmol.* 1995;113:216-221.

36. Jia L, Cepurna WO, Johnson EC, et al. Effect of general anesthetics on IOP in rats with experimental aqueous outflow obstruction. *Invest Ophthalmol Vis Sci.* 2000;41:3415-3419.

37. Anderson DR, Burgoyne C. Quantifying structures in the ocular fundus. *Invest Ophthalmol Vis Sci.* 2012;53:4531.

38. Lichter PR. Variability of expert observers in evaluating the optic disc. *Trans Am Ophthalmol Soc.* 1976;74:532-572.

39. Tielsch JM, Katz J, Quigley HA, et al. Intraobserver and interobserver agreement in measurement of optic disc characteristics. *Ophthalmology.* 1988;95:350-356.

40. Abrams LS, Scott IU, Spaeth GL, et al. Agreement among optometrists, ophthalmologists, and residents in evaluating the optic disc for glaucoma. *Ophthalmology.* 1994;101:1662-1667.

41. Kwon YH, Adix M, Zimmerman MB, et al. Variance owing to observer, repeat imaging, and fundus camera type on cup-to-disc ratio estimates by stereo planimetry. *J Glaucoma.* 2009;18:305-310.

42. Bowd C, Weinreb RN, Williams JM, et al. The retinal nerve fiber layer thickness in ocular hypertensive, normal, and glaucomatous eyes with optical coherence tomography. *Arch Ophthalmol.* 2000;118:22-26.

43. Cohen MJ, Kaliner E, Frenkel S, et al. Morphometric analysis of human peripapillary retinal nerve fiber layer thickness. *Invest Ophthalmol Vis Sci.* 2008;49:941-944.

44. Hood DC, Wang DL, Raza AS, et al. The locations of circumpapillary glaucomatous defects seen on frequency-domain OCT scans. *Invest Ophthalmol Vis Sci.* 2013;54:7338-7343.

45. Dreher B, Sefton AJ, Ni SY, et al. The morphology, number, distribution and central projections of Class I retinal ganglion cells in albino and hooded rats. *Brain Behav Evol.* 1985;26:10-48.

46. Fukuda Y. A three-group classification of rat retinal ganglion cells: histological and physiological studies. *Brain Res.* 1977;119:327-334.

47. Jeffery G. The relationship between cell density and the nasotemporal division in the rat retina. *Brain Res.* 1985;347:354-357.

48. McCall MJ, Robinson SR, Dreher B. Differential retinal growth appears to be the primary factor producing the ganglion cell density gradient in the rat. *Neurosci Lett.* 1987;79:78-84.

49. Perry VH. Evidence for an amacrine cell system in the ganglion cell layer of the rat retina. *Neuroscience.* 1981;6:931-944.

50. Reese BE, Cowey A. Large retinal ganglion cells in the rat: their distribution and laterality of projection. *Exp Brain Res.* 1986;61:375-385.

51. Salinas-Navarro M, Mayor-Torroglosa S, Jimenez-Lopez M, et al. A computerized analysis of the entire retinal ganglion cell population and its spatial distribution in adult rats. *Vision Res.* 2009;49:115-126.

52. Danias J, Shen F, Goldblum D, et al. Cytoarchitecture of the retinal ganglion cells in the rat. *Invest Ophthalmol Vis Sci.* 2002;43:587-594.

53. John SW, Smith RS, Savinova OV, et al. Essential iris atrophy, pigment dispersion, and glaucoma in DBA/2J mice. *Invest Ophthalmol Vis Sci.* 1998;39:951-962.

54. Garcia-Valenzuela E, Shareef S, Walsh J, et al. Programmed cell death of retinal ganglion cells during experimental glaucoma. *Exp Eye Res.* 1995;61:33-44.

55. Joos KM, Li C, Sappington RM. Morphometric changes in the rat optic nerve following short-term intermittent elevations in intraocular pressure. *Invest Ophthalmol Vis Sci.* 2010;51:6431-6440.

56. Morrison JC, Moore CG, Deppmeier LM, et al. A rat model of chronic pressure-induced optic nerve damage. *Exp Eye Res.* 1997;64:85-96.

57. Ueda J, Sawaguchi S, Hanyu T, et al. Experimental glaucoma model in the rat induced by laser trabecular photocoagulation after an intracameral injection of India ink. *Jpn J Ophthalmol.* 1998;42:337-344.

58. Morrison JC, Johnson EC, Cepurna W, et al. Understanding mechanisms of pressure-induced optic nerve damage. *Prog Retin Eye Res.* 2005;24:217-240.

59. Morrison JC, Nylander KB, Lauer AK, et al. Glaucoma drops control intraocular pressure and protect optic nerves in a rat model of glaucoma. *Invest Ophthalmol Vis Sci.* 1998;39:526-531.

60. Sun D, Lye-Barthel M, Masland RH, et al. The morphology and spatial arrangement of astrocytes in the optic nerve head of the mouse. *The Journal of comparative neurology.* 2009;516:1-19.

61. Morrison J, Farrell S, Johnson E, et al. Structure and composition of the rodent lamina cribrosa. *Exp Eye Res.* 1995;60:127-135.

62. Choi J, Jeong J, Cho HS, et al. Effect of nocturnal blood pressure reduction on circadian fluctuation of mean ocular perfusion pressure: a risk factor for normal tension glaucoma. *Invest Ophthalmol Vis Sci.* 2006;47:831-836.

63. Lin JS, Liu JH. Circadian variations in intracranial pressure and translaminar pressure difference in Sprague-Dawley rats. *Invest Ophthalmol Vis Sci.* 2010;51:5739-5743.

64. Sehi M, Flanagan JG, Zeng L, et al. The association between diurnal variation of optic nerve head topography and intraocular pressure and ocular perfusion pressure in untreated primary open-angle glaucoma. *J Glaucoma.* 2011;20:44-50.

65. Kiel JW, van Heuven WA. Ocular perfusion pressure and choroidal blood flow in the rabbit. *Invest Ophthalmol Vis Sci.* 1995;36:579-585.

66. Kyhn MV, Warfvinge K, Scherfig E, et al. Acute retinal ischemia caused by controlled low ocular perfusion pressure in a porcine model. Electrophysiological and histological characterisation. *Exp Eye Res.* 2009;88:1100-1106.

67. Choi J, Kim KH, Jeong J, et al. Circadian fluctuation of mean ocular perfusion pressure is a consistent risk factor for normal-tension glaucoma. *Invest Ophthalmol Vis Sci.* 2007;48:104-111.

68. Choi J, Lee JR, Lee Y, et al. Relationship between 24-hour mean ocular perfusion pressure fluctuation and rate of paracentral visual field progression in normal-tension glaucoma. *Invest Ophthalmol Vis Sci.* 2013;54:6150-6157.

69. Grover DS, Budenz DL. Ocular perfusion pressure and glaucoma. *Int Ophthalmol Clin.* 2011;51:19-25.

70. Cherecheanu AP, Garhofer G, Schmidl D, et al. Ocular perfusion pressure and ocular blood flow in glaucoma. *Curr Opin Pharmacol.* 2013;13:36-42.

71. Yablonski ME RR, Pokorny KS. Effect of decreased intracranial pressure on optic disc. *Invest Ophthalmol.* 1979;18 (Suppl):165.

72. Gooley JJ, Lu J, Chou TC, et al. Melanopsin in cells of origin of the retinohypothalamic tract. *Nat Neurosci.* 2001;4:1165.

73. Provencio I, Rodriguez IR, Jiang G, et al. A novel human opsin in the inner retina. *J Neurosci.* 2000;20:600-605.

74. Berson DM, Dunn FA, Takao M. Phototransduction by retinal ganglion cells that set the circadian clock. *Science.* 2002;295:1070-1073.

75. Hattar S, Liao HW, Takao M, et al. Melanopsin-containing retinal ganglion cells: architecture, projections, and intrinsic photosensitivity. *Science.* 2002;295:1065-1070.

76. Stephan FK, Zucker I. Circadian rhythms in drinking behavior and locomotor activity of rats are eliminated by hypothalamic lesions. *Proc Natl Acad Sci USA.* 1972;69:1583-1586.

77. Van den Pol AN, Powley T. A fine-grained anatomical analysis of the role of the rat suprachiasmatic nucleus in circadian rhythms of feeding and drinking. *Brain Res.* 1979;160:307-326.

78. Eastman CI, Mistlberger RE, Rechtschaffen A. Suprachiasmatic nuclei lesions eliminate circadian temperature and sleep rhythms in the rat. *Physiol Behav.* 1984;32:357-368.

79. Herzog ED, Tosini G. The mammalian circadian clock shop. *Semin Cell Dev Biol.* 2001;12:295-303.

80. Rosenwasser AM, Adler NT. Structure and function in circadian timing systems: evidence for multiple coupled circadian oscillators. *Neurosci Biobehav Rev.* 1986;10:431-448.

81. Davidson AJ, Yamazaki S, Arble DM, et al. Resetting of central and peripheral circadian oscillators in aged rats. *Neurobiol Aging.* 2008;29:471-477.

82. Yamazaki S, Numano R, Abe M, et al. Resetting central and peripheral circadian oscillators in transgenic rats. *Science.* 2000;288:682-685.

83. Zheng B, Albrecht U, Kaasik K, et al. Nonredundant roles of the mPer1 and mPer2 genes in the mammalian circadian clock. *Cell.* 2001;105:683-694.

84. David R, Zangwill L, Briscoe D, et al. Diurnal intraocular pressure variations: an analysis of 690 diurnal curves. *Br J Ophthalmol.* 1992;76:280-283.

85. Liu JH, Zhang X, Kripke DF, et al. Twenty-four-hour intraocular pressure pattern associated with early glaucomatous changes. *Invest Ophthalmol Vis Sci.* 2003;44:1586-1590.

86. Liu JH, Kripke DF, Hoffman RE, et al. Nocturnal elevation of intraocular pressure in young adults. *Invest Ophthalmol Vis Sci.* 1998;39:2707-2712.

87. Liu JH, Kripke DF, Twa MD, et al. Twenty-four-hour pattern of intraocular pressure in the aging population. *Invest Ophthalmol Vis Sci.* 1999;40:2912-2917.

88. Aihara M, Lindsey JD, Weinreb RN. Twenty-four-hour pattern of mouse intraocular pressure. *Exp Eye Res.* 2003;77:681-686.

89. Li R, Liu JH. Telemetric monitoring of 24 h intraocular pressure in conscious and freely moving C57BL/6J and CBA/CaJ mice. *Mol Vis.* 2008;14:745-749.

90. Mermoud A, Baerveldt G, Minckler DS, et al. Intraocular pressure in Lewis rats. *Invest Ophthalmol Vis Sci.* 1994;35:2455-2460.

91. Moore CG, Johnson EC, Morrison JC. Circadian rhythm of intraocular pressure in the rat. *Curr Eye Res.* 1996;15:185-191.

92. Rowland JM, Potter DE, Reiter RJ. Circadian rhythm in intraocular pressure: a rabbit model. *Curr Eye Res.* 1981;1:169-173.

93. Del Sole MJ, Sande PH, Bernades JM, et al. Circadian rhythm of intraocular pressure in cats. *Vet Ophthalmol.* 2007;10:155-161.

94. Piccione G, Giannetto C, Fazio F, et al. Influence of different artificial lighting regimes on intraocular pressure circadian profile in the dog (Canis familiaris). *Exp Anim.* 2010;59:215-223.

95. Caprioli J, Coleman AL. Intraocular pressure fluctuation a risk factor for visual field progression at low intraocular pressures in the advanced glaucoma intervention study. *Ophthalmology.* 2008;115:1123-1129 e1123.

96. Musch DC, Gillespie BW, Niziol LM, et al. Intraocular pressure control and long-term visual field loss in the Collaborative Initial Glaucoma Treatment Study. *Ophthalmology.* 2011;118:1766-1773.

97. Depres-Brummer P, Levi F, Metzger G, et al. Light-induced suppression of the rat circadian system. *Am J Physiol.* 1995;268:R1111-1116.

98. Eastman C, Rechtschaffen A. Circadian temperature and wake rhythms of rats exposed to prolonged continuous illumination. *Physiol Behav.* 1983;31:417-427.

99. Honma KI, Hiroshige T. Internal synchronization among several circadian rhythms in rats under constant light. *Am J Physiol.* 1978;235:R243-249.

100. Honma KI, Hiroshige T. Endogenous ultradian rhythms in rats exposed to prolonged continuous light. *Am J Physiol.* 1978;235:R250-256.

101. Bellezza AJ, Rintalan CJ, Thompson HW, et al. Deformation of the lamina cribrosa and anterior scleral canal wall in early experimental glaucoma. *Invest Ophthalmol Vis Sci.* 2003;44:623-637.

102. Roberts MD, Grau V, Grimm J, et al. Remodeling of the connective tissue microarchitecture of the lamina cribrosa in early experimental glaucoma. *Invest Ophthalmol Vis Sci.* 2009;50:681-690.

103. Chidlow G, Ebneter A, Wood JP, et al. The optic nerve head is the site of axonal transport disruption, axonal cytoskeleton damage and putative axonal regeneration failure in a rat model of glaucoma. *Acta neuropathologica.* 2011;121:737-751.

104. Howell GR, Libby RT, Jakobs TC, et al. Axons of retinal ganglion cells are insulted in the optic nerve early in DBA/2J glaucoma. *J Cell Biol.* 2007;179:1523-1537.

105. Baumann M, Gentile RC, Liebmann JM, et al. Reproducibility of retinal thickness measurements in normal eyes using optical coherence tomography. *Ophthalmic Surg Lasers.* 1998;29:280-285.

106. Blumenthal EZ, Williams JM, Weinreb RN, et al. Reproducibility of nerve fiber layer thickness measurements by use of optical coherence tomography. *Ophthalmology.* 2000;107:2278-2282.

107. Budenz DL, Chang RT, Huang X, et al. Reproducibility of retinal nerve fiber thickness measurements using the stratus OCT in normal and glaucomatous eyes. *Invest Ophthalmol Vis Sci.* 2005;46:2440-2443.

108. González-García AO, Vizzeri G, Bowd C, et al. Reproducibility of RTVue retinal nerve fiber layer thickness and optic disc measurements and agreement with Stratus optical coherence tomography measurements. *Am J Ophthalmol.* 2009;147:1067-1074, 1074.e1061-1067-1074, 1074.e1061.

109. Gürses-Ozden R, Teng C, Vessani R, et al. Macular and retinal nerve fiber layer thickness measurement reproducibility using optical coherence tomography (OCT-3). *J Glaucoma.* 2004;13:238-244.

110. Kim JS, Ishikawa H, Sung KR, et al. Retinal Nerve Fibre Layer Thickness Measurement Reproducibility Improved with Spectral Domain Optical Coherence Tomography. *Br J Ophthalmol.* 2009;93:1057-1063.

111. Langenegger SJ, Funk J, Töteberg-Harms M. Reproducibility of retinal nerve fiber layer thickness measurements using the eye tracker and the retest function of Spectralis SD-OCT in glaucomatous and healthy control eyes. *Invest Ophthalmol Vis Sci.* 2011;52:3338-3344.

112. Massin P, Vicaut E, Haouchine B, et al. Reproducibility of Retinal Mapping Using Optical Coherence Tomography. *Arch Ophthalmol.* 2001;119:1135-1142.

113. Paunescu LA, Schuman JS, Price LL, et al. Reproducibility of nerve fiber thickness, macular thickness, and optic nerve head measurements using StratusOCT. *Invest Ophthalmol Vis Sci.* 2004;45:1716-1724.

114. Wolf-Schnurrbusch UEK, Ceklic L, Brinkmann CK, et al. Macular Thickness Measurements in Healthy Eyes Using Six Different Optical Coherence Tomography Instruments. *Invest Ophthalmol Vis Sci.* 2009;50:3432-3437.

115. Wu H, de Boer JF, Chen TC. Reproducibility of retinal nerve fiber layer thickness measurements using spectral domain optical coherence tomography. *J Glaucoma.* 2011;20:470-476.

116. Guo L, Normando EM, Nizari S, et al. Tracking longitudinal retinal changes in experimental ocular hypertension using the cSLO and spectral domain-OCT. *Invest Ophthalmol Vis Sci.* 2010;51:6504-6513.

117. Block MT. A note on the refraction and image formation of the rat's eye. *Vision Res.* 1969;9:705-711.

118. Chaudhuri A, Hallett PE, Parker JA. Aspheric curvatures, refractive indices and chromatic aberration for the rat eye. *Vision Res.* 1983;23:1351-1363.

119. Hughes A. A schematic eye for the rat. *Vision Res.* 1979;19:569-588.

120. Konstas AG, Maltezos AC, Gandi S, et al. Comparison of 24-hour intraocular pressure reduction with two dosing regimens of latanoprost and timolol maleate in patients with primary open-angle glaucoma. *Am J Ophthalmol.* 1999;128:15-20.

121. Konstas AG, Nakos E, Tersis I, et al. A comparison of once-daily morning vs evening dosing of concomitant latanoprost/timolol. *Am J Ophthalmol.* 2002;133:753-757.

122. The Advanced Glaucoma Intervention Study (AGIS): 7. The relationship between control of intraocular pressure and visual field deterioration.The AGIS Investigators. *Am J Ophthalmol.* 2000;130:429-440.

123. Bengtsson B, Leske MC, Hyman L, et al. Fluctuation of intraocular pressure and glaucoma progression in the early manifest glaucoma trial. *Ophthalmology.* 2007;114:205-209.

124. Asrani S, Zeimer R, Wilensky J, et al. Large diurnal fluctuations in intraocular pressure are an independent risk factor in patients with glaucoma. *J Glaucoma.* 2000;9:134-142.

125. Gaasterland D, Kupfer C. Experimental glaucoma in the rhesus monkey. *Invest Ophthalmol.* 1974;13:455-457.

126. Pederson JE, Gaasterland DE. Laser-induced primate glaucoma. I. Progression of cupping. *Arch Ophthalmol.* 1984;102:1689-1692.

127. Quigley HA, Hohman RM. Laser energy levels for trabecular meshwork damage in the primate eye. *Invest Ophthalmol Vis Sci.* 1983;24:1305-1307.

128. Sappington RM, Carlson BJ, Crish SD, et al. The microbead occlusion model: a paradigm for induced ocular hypertension in rats and mice. *Invest Ophthalmol Vis Sci.* 2010;51:207-216.

129. Samsel PA, Kisiswa L, Erichsen JT, et al. A novel method for the induction of experimental glaucoma using magnetic microspheres. *Invest Ophthalmol Vis Sci.* 2011;52:1671-1675.

130. Shareef SR, Garcia-Valenzuela E, Salierno A, et al. Chronic ocular hypertension following episcleral venous occlusion in rats. *Exp Eye Res.* 1995;61:379-382.

131. Yu S, Tanabe T, Yoshimura N. A rat model of glaucoma induced by episcleral vein ligation. *Exp Eye Res.* 2006;83:758-770.

132. Dalke C, Pleyer U, Graw J. On the use of Tono-Pen XL for the measurement of intraocular pressure in mice. *Exp Eye Res.* 2005;80:295-296.

133. Moore CG, Milne ST, Morrison JC. Noninvasive measurement of rat intraocular pressure with the Tono-Pen. *Invest Ophthalmol Vis Sci.* 1993;34:363-369.

134. Pang IH, Wang WH, Millar JC, et al. Measurement of mouse intraocular pressure with the Tono-Pen. *Exp Eye Res.* 2005;81:359-360.

135. Reitsamer HA, Kiel JW, Harrison JM, et al. Tonopen measurement of intraocular pressure in mice. *Exp Eye Res.* 2004;78:799-804.

136. Ding C, Wang P, Tian N. Effect of general anesthetics on IOP in elevated IOP mouse model. *Exp Eye Res.* 2011;92:512-520.

137. Kontiola AI, Goldblum D, Mittag T, et al. The induction/impact tonometer: a new instrument to measure intraocular pressure in the rat. *Exp Eye Res.* 2001;73:781-785.

138. Morris CA, Crowston JG, Lindsey JD, et al. Comparison of invasive and non-invasive tonometry in the mouse. *Exp Eye Res.* 2006;82:1094-1099.

139. Wang WH, Millar JC, Pang IH, et al. Noninvasive measurement of rodent intraocular pressure with a rebound tonometer. *Invest Ophthalmol Vis Sci.* 2005;46:4617-4621.

140. Mermoud A, Baerveldt G, Minckler DS, et al. Intraocular pressure in Lewis rats. *Invest Ophthalmol Vis Sci.* 1994;35:2455-2460.

141. Cohan BE, Bohr DF. Goldmann applanation tonometry in the conscious rat. *Invest Ophthalmol Vis Sci.* 2001;42:340-342.

142. Cohan BE, Bohr DF. Measurement of intraocular pressure in awake mice. *Invest Ophthalmol Vis Sci.* 2001;42:2560-2562.

143. Weinreb RN, Aung T, Medeiros FA. The pathophysiology and treatment of glaucoma: a review. *JAMA.* 2014;311:1901-1911.

144. Nickells RW, Howell GR, Soto I, et al. Under pressure: cellular and molecular responses during glaucoma, a common neurodegeneration with axonopathy. *Annu Rev Neurosci.* 2012;35:153-179.

145. Kass MA, Heuer DK, Higginbotham EJ, et al. The Ocular Hypertension Treatment Study: a randomized trial determines that topical ocular hypotensive medication delays or prevents the onset of primary open-angle glaucoma. *Arch Ophthalmol.* 2002;120:701-713; discussion 829-730.

146. Heijl A, Leske MC, Bengtsson B, et al. Reduction of intraocular pressure and glaucoma progression: results from the Early Manifest Glaucoma Trial. *Arch Ophthalmol.* 2002;120:1268-1279.

147. AGIS. The Advanced Glaucoma Intervention Study (AGIS): 7. The relationship between control of intraocular pressure and visual field deterioration.The AGIS Investigators. *Am J Ophthalmol.* 2000;130:429-440.

148. Sommer A, Tielsch JM, Katz J, et al. Relationship between intraocular pressure and primary open angle glaucoma among white and black Americans. The Baltimore Eye Survey. *Arch Ophthalmol.* 1991;109:1090-1095.

149. Francis BA, Varma R, Chopra V, et al. Intraocular pressure, central corneal thickness, and prevalence of open-angle glaucoma: the Los Angeles Latino Eye Study. *Am J Ophthalmol.* 2008;146:741-746.

150. Luo X, Patel NB, Rajagopalan LP, et al. Relation between macular retinal ganglion cell/inner plexiform layer thickness and multifocal electroretinogram measures in experimental glaucoma. *Invest Ophthalmol Vis Sci.* 2014;55:4512-4524.

151. Vidal-Sanz M, Salinas-Navarro M, Nadal-Nicolas FM, et al. Understanding glaucomatous damage: anatomical and functional data from ocular hypertensive rodent retinas. *Prog Retin Eye Res.* 2012;31:1-27.

152. Halberg F, Tong YL, Johnson EA. Circadian system phase, an aspect of temporal morphology: procedures and illustrative examples. In: von Mayersbach H (ed), *The Cellular Aspects of Biorhythms.* Berlin: Springer; 1967:20-48.

153. Refinetti R, Lissen GC, Halberg F. Procedures for numerical analysis of circadian rhythms. *Biol Rhythm Res.* 2007;38:275-325.

154. Cornelissen G. Cosinor-based rhythmometry. *Theor Biol Med Model.* 2014;11:16.

155. Danias J, Kontiola AI, Filippopoulos T, et al. Method for the noninvasive measurement of intraocular pressure in mice. *Invest Ophthalmol Vis Sci.* 2003;44:1138-1141.

156. Carpenter GA, Grossberg S. A neural theory of circadian rhythms: Aschoff's rule in diurnal and nocturnal mammals. *Am J Physiol.* 1984;247:R1067-1082.

157. Rosenwasser AM. Circadian drinking rhythms in SHR and WKY rats: effects of increasing light intensity. *Physiol Behav.* 1993;53:1035-1041.

158. Morrison JC, Jia L, Cepurna W, et al. Reliability and sensitivity of the TonoLab rebound tonometer in awake Brown Norway rats. *Invest Ophthalmol Vis Sci.* 2009;50:2802-2808.

159. Aschoff J. Exogenous and endogenous components in circadian rhythms. *Cold Spring Harb Symp Quant Biol.* 1960;25:11-28.

160. De Smedt S, Mermoud A, Schnyder C. 24-hour intraocular pressure fluctuation monitoring using an ocular telemetry Sensor: tolerability and functionality in healthy subjects. *J Glaucoma.* 2012;21:539-544.

161. Lorenz K, Korb C, Herzog N, et al. Tolerability of 24-hour intraocular pressure monitoring of a pressure-sensitive contact lens. *J Glaucoma.* 2013;22:311-316.

162. Mansouri K, Medeiros FA, Tafreshi A, et al. Continuous 24-hour monitoring of intraocular pressure patterns with a contact lens sensor: safety, tolerability, and reproducibility in patients with glaucoma. *Arch Ophthalmol.* 2012;130:1534-1539.

163. Twa MD, Roberts CJ, Karol HJ, et al. Evaluation of a contact lens-embedded sensor for intraocular pressure measurement. *J Glaucoma.* 2010;19:382-390.

164. Melki SA, Todani A, Cherfan DG. An implantable intraocular pressure transducer: Initial safety outcomes. *JAMA Ophthalmol.* 2014;Ahead of print.

165. Downs JC, Burgoyne CF, Seigfreid WP, et al. 24-hour IOP telemetry in the nonhuman primate: implant system performance and initial characterization of IOP at multiple timescales. *Invest Ophthalmol Vis Sci.* 2011;52:7365-7375.

166. McLaren JW, Brubaker RF, FitzSimon JS. Continuous measurement of intraocular pressure in rabbits by telemetry. *Invest Ophthalmol Vis Sci.* 1996;37:966-975.

167. Schnell CR, Debon C, Percicot CL. Measurement of intraocular pressure by telemetry in conscious, unrestrained rabbits. *Invest Ophthalmol Vis Sci.* 1996;37:958-965.

168. Todani A, Behlau I, Fava MA, et al. Intraocular pressure measurement by radio wave telemetry. *Invest Ophthalmol Vis Sci.* 2011;52:9573-9580.

169. Ahmed F, Brown KM, Stephan DA, et al. Microarray analysis of changes in mRNA levels in the rat retina after experimental elevation of intraocular pressure. *Invest Ophthalmol Vis Sci.* 2004;45:1247-1258.

170. Hartwick AT, Zhang X, Chauhan BC, et al. Functional assessment of glutamate clearance mechanisms in a chronic rat glaucoma model using retinal ganglion cell calcium imaging. *J Neurochem.* 2005;94:794-807.

171. Jia L, Cepurna WO, Johnson EC, et al. Effect of general anesthetics on IOP in rats with experimental aqueous outflow obstruction. *Invest Ophthalmol Vis Sci.* 2000;41:3415-3419.

172. Nissirios N, Chanis R, Johnson E, et al. Comparison of anterior segment structures in two rat glaucoma models: an ultrasound biomicroscopic study. *Invest Ophthalmol Vis Sci.* 2008;49:2478-2482.

173. Pang IH, Wang WH, Clark AF. Acute effects of glaucoma medications on rat intraocular pressure. *Exp Eye Res.* 2005;80:207-214.

174. Sposato V, Parisi V, Manni L, et al. Glaucoma alters the expression of NGF and NGF receptors in visual cortex and geniculate nucleus of rats: effect of eye NGF application. *Vision Res.* 2009;49:54-63.

175. Sehi M, Flanagan JG, Zeng L, et al. The association between diurnal variation of optic nerve head topography and intraocular pressure and ocular perfusion pressure in untreated primary open-angle glaucoma. *J Glaucoma.* 2011;20:44-50.

176. Choi J, Jeong J, Cho HS, et al. Effect of nocturnal blood pressure reduction on circadian fluctuation of mean ocular perfusion pressure: a risk factor for normal tension glaucoma. *Invest Ophthalmol Vis Sci.* 2006;47:831-836.

177. Lin JS, Liu JH. Circadian variations in intracranial pressure and translaminar pressure difference in Sprague-Dawley rats. *Invest Ophthalmol Vis Sci.* 2010;51:5739-5743.

178. Shimamura T, Nakajima M, Iwasaki T, et al. Analysis of circadian blood pressure rhythm and target-organ damage in stroke-prone spontaneously hypertensive rats. *J Hypertens.* 1999;17:211-220.

179. Basset A, Laude D, Laurent S, et al. Contrasting circadian rhythms of blood pressure among inbred rat strains: recognition of dipper and non-dipper patterns. *J Hypertens.* 2004;22:727-737.

180. Gordon CJ. Cardiac and thermal homeostasis in the aging Brown Norway rat. *J Gerontol A Biol Sci Med Sci.* 2008;63:1307-1313.

181. Kramer K, Voss HP, Grimbergen JA, et al. Telemetric monitoring of blood pressure in freely moving mice: a preliminary study. *Lab Anim.* 2000;34:272-280.

182. Irvine RJ, White J, Chan R. The influence of restraint on blood pressure in the rat. *J Pharmacol Toxicol Methods.* 1997;38:157-162.

183. Kubota Y, Umegaki K, Kagota S, et al. Evaluation of blood pressure measured by tail-cuff methods (without heating) in spontaneously hypertensive rats. *Biol Pharm Bull.* 2006;29:1756-1758.

184. Huang D, Swanson EA, Lin CP, et al. Optical Coherence Tomography. *Science.* 1991;254:1178-1181.

185. Huber G, Beck SC, Grimm C, et al. Spectral domain optical coherence tomography in mouse models of retinal degeneration. *Invest Ophthalmol Vis Sci.* 2009;50:5888-5895.

186. Kim KH, Puoris'haag M, Maguluri GN, et al. Monitoring Mouse Retinal Degeneration with High-Resolution Spectral-Domain Optical Coherence Tomography. *J Vision.* 2008;8.

187. Baumann M, Gentile RC, Liebmann JM, et al. Reproducibility of retinal thickness measurements in normal eyes using optical coherence tomography. *Ophthalmic Surg Las.* 1998;29:280-285.

188. Campbell MC, Hughes A. An analytic, gradient index schematic lens and eye for the rat which predicts aberrations for finite pupils. *Vision Res.* 1981;21:1129-1148.

189. Kocaoglu OP, Uhlhorn SR, Hernandez E, et al. Simultaneous fundus imaging and optical coherence tomography of the mouse retina. *Invest Ophthalmol Vis Sci.* 2007;48:1283-1289.

190. Evangelidis GD, Psarakis EZ. Parametric image alignment using enhanced correlation coefficient maximization. *IEEE Trans Pattern Anal Mach Intell.* 2008;30:1858-1865.

191. Ruggeri M, Wehbe H, Jiao S, et al. In vivo three-dimensional high-resolution imaging of rodent retina with spectral-domain optical coherence tomography. *Invest Ophthalmol Vis Sci.* 2007;48:1808-1814.

192. Huang J, Savini G, Feng Y, et al. Retinal nerve fiber layer thickness measurements in rats with spectral domain-optical coherence tomography. *Invest Ophthalmol Vis Sci.* 2012;53:749-750.

193. Shrout PE, Fleiss JL. Intraclass correlations: uses in assessing rater reliability. *Psychol Bull.* 1979;86:420-428.

194. Fortune B, Choe TE, Reynaud J, et al. Deformation of the rodent optic nerve head and peripapillary structures during acute intraocular pressure elevation. *Invest Ophthalmol Vis Sci.* 2011;52:6651-6661.

195. Nagata A, Higashide T, Ohkubo S, et al. In vivo quantitative evaluation of the rat retinal nerve fiber layer with optical coherence tomography. *Invest Ophthalmol Vis Sci.* 2009;50:2809-2815.

196. Srinivasan VJ, Ko TH, Wojtkowski M, et al. Noninvasive volumetric imaging and morphometry of the rodent retina with high-speed, ultrahigh-resolution optical coherence tomography. *Invest Ophthalmol Vis Sci.* 2006;47:5522-5528.

197. Abbott CJ, McBrien NA, Grunert U, et al. Relationship of the optical coherence tomography signal to underlying retinal histology in the tree shrew (Tupaia belangeri). *Invest Ophthalmol Vis Sci.* 2009;50:414-423.

198. Gloesmann M, Hermann B, Schubert C, et al. Histologic correlation of pig retina radial stratification with ultrahigh-resolution optical coherence tomography. *Invest Ophthalmol Vis Sci.* 2003;44:1696-1703.

199. Huang Y, Cideciyan AV, Papastergiou GI, et al. Relation of optical coherence tomography to microanatomy in normal and rd chickens. *Invest Ophthalmol Vis Sci.* 1998;39:2405-2416.

200. Gabriele ML, Ishikawa H, Schuman JS, et al. Reproducibility of spectral-domain optical coherence tomography total retinal thickness measurements in mice. *Invest Ophthalmol Vis Sci.* 2010;51:6519-6523.

201. Balasubramanian M, Bowd C, Vizzeri G, et al. Effect of image quality on tissue thickness measurements obtained with spectral domain-optical coherence tomography. *Opt Express.* 2009;17:4019-4036.

202. Cheung CY, Leung CK, Lin D, et al. Relationship between retinal nerve fiber layer measurement and signal strength in optical coherence tomography. *Ophthalmology.* 2008;115:1347-1351, 1351 e1341-1342.

203. Huang J, Liu X, Wu Z, et al. Image quality affects macular and retinal nerve fiber layer thickness measurements on fourier-domain optical coherence tomography. *Ophthalmic Surg Lasers Imaging.* 2011;42:216-221.

204. Stein DM, Ishikawa H, Hariprasad R, et al. A new quality assessment parameter for optical coherence tomography. *Br J Ophthalmol.* 2006;90:186-190.

205. Wu Z, Vazeen M, Varma R, et al. Factors associated with variability in retinal nerve fiber layer thickness measurements obtained by optical coherence tomography. *Ophthalmology.* 2007;114:1505-1512.

206. Patel NB, Wheat JL, Rodriguez A, et al. Agreement between Retinal Nerve Fiber Layer Measures from Spectralis and Cirrus Spectral Domain OCT. *Optometry & Vision Science.* 2012;89:652-666.

207. Geng Y, Greenberg KP, Wolfe R, et al. In vivo imaging of microscopic structures in the rat retina. *Invest Ophthalmol Vis Sci.* 2009;50:5872-5879.

208. Higashide T, Kawaguchi I, Ohkubo S, et al. In vivo imaging and counting of rat retinal ganglion cells using a scanning laser ophthalmoscope. *Invest Ophthalmol Vis Sci.* 2006;47:2943-2950.

209. Seeliger MW, Beck SC, Pereyra-Munoz N, et al. In vivo confocal imaging of the retina in animal models using scanning laser ophthalmoscopy. *Vision Res.* 2005;45:3512-3519.

210. Walsh MK, Quigley HA. In vivo time-lapse fluorescence imaging of individual retinal ganglion cells in mice. *J Neurosci Methods.* 2008;169:214-221.

211. Hwang YH, Kim YY. Correlation between optic nerve head parameters and retinal nerve fibre layer thickness measured by spectral-domain optical

coherence tomography in myopic eyes. *Clin Experiment Ophthalmol.* 2012;40:713-720.

212. Patel NB, Garcia B, Harwerth RS. Influence of anterior segment power on the scan path and RNFL thickness using SD-OCT. *Invest Ophthalmol Vis Sci.* 2012;53:5788-5798.

213. Sanchez-Cano A, Baraibar B, Pablo LE, et al. Magnification characteristics of the Optical Coherence Tomograph STRATUS OCT 3000. *Ophthalmic Physiol Opt.* 2008;28:21-28.

214. Savini G, Barboni P, Parisi V, et al. The influence of axial length on retinal nerve fibre layer thickness and optic-disc size measurements by spectral-domain OCT. *Br J Ophthalmol.* 2012;96:57-61.

215. Lashley KS. The Mechanism of Vision. V. The Structure and Image-Forming Power of the Rat's Eye. *J Comp Psychol.* 1932;13:173-200.

216. Massof RW, Chang FW. A revision of the rat schematic eye. *Vision Res.* 1972;12:793-796.

217. Chui TY, Bissig D, Berkowitz BA, et al. Refractive Development in the "ROP Rat". *J Ophthalmol.* 2012;2012:956705.

218. Guggenheim JA, Creer RC, Qin XJ. Postnatal refractive development in the Brown Norway rat: limitations of standard refractive and ocular component dimension measurement techniques. *Curr Eye Res.* 2004;29:369-376.

219. Nissirios N, Chanis R, Johnson E, et al. Comparison of anterior segment structures in two rat glaucoma models: an ultrasound biomicroscopic study. *Invest Ophthalmol Vis Sci.* 2008;49:2478-2482.

220. Lozano DC, Twa MD. Quantitative evaluation of factors influencing the repeatability of SD-OCT thickness measurements in the rat. *Invest Ophthalmol Vis Sci.* 2012;53:8378-8385.

221. Lozano DC, Twa MD. The Effects of RGP Contact Lens use on SD-OCT Retinal Image Quality in the Brown Norway Rat. *Am Acad Optom: Meeting Abstracts.* 2010;87(10): 105359.

222. van Oterendorp C, Diaz-Santana L, Bull N, et al. Light scattering and wavefront aberrations in in vivo imaging of the rat eye: a comparison study. *Invest Ophthalmol Vis Sci.* 2011;52:4551-4559.

223. Mutti DO, Zadnik K, Murphy CJ. The effect of continuous light on refractive error and the ocular components of the rat. *Exp Eye Res.* 1998;67:631-636.

224. Buttery RG, Hinrichsen CF, Weller WL, et al. How thick should a retina be? A comparative study of mammalian species with and without intraretinal vasculature. *Vision Res.* 1991;31:169-187.

225. Cavallotti C, Artico M, Pescosolido N, et al. Age-related changes in rat retina. *Jpn J Ophthalmol.* 2001;45:68-75.

226. Cohan BE, Pearch AC, Jokelainen PT, et al. Optic disc imaging in conscious rats and mice. *Invest Ophthalmol Vis Sci.* 2003;44:160-163.

227. Chou TH, Kocaoglu OP, Borja D, et al. Postnatal elongation of eye size in DBA/2J mice compared with C57BL/6J mice: in vivo analysis with whole-eye OCT. *Invest Ophthalmol Vis Sci.* 2011;52:3604-3612.

228. Jiang M, Wu PC, Fini ME, et al. Single-shot dimension measurements of the mouse eye using SD-OCT. *Ophthalmic Surg Lasers Imaging.* 2012;43:252-256.

229. Zhou X, Xie J, Shen M, et al. Biometric measurement of the mouse eye using optical coherence tomography with focal plane advancement. *Vision Res.* 2008;48:1137-1143.

230. Segupta P. A Scientific Review of Age Determination for a Laboratory Rat: How Old is it in Comparison with Human Age? *Biomedicine International.* 2011;2:81-89.

231. Bathija R, Zangwill L, Berry CC, et al. Detection of early glaucomatous structural damage with confocal scanning laser tomography. *J Glaucoma.* 1998;7:121-127.

232. Chauhan BC, Hutchison DM, Artes PH, et al. Optic disc progression in glaucoma: comparison of confocal scanning laser tomography to optic disc photographs in a prospective study. *Invest Ophthalmol Vis Sci.* 2009;50:1682-1691.

233. Da Pozzo S, Marchesan R, Ravalico G. Scanning laser polarimetry - a review. *Clin Exp Ophthalmol.* 2009;37:68-80.

234. He L, Yang H, Gardiner SK, et al. Longitudinal detection of optic nerve head changes by spectral domain optical coherence tomography in early experimental glaucoma. *Invest Ophthalmol Vis Sci.* 2014;55:574-586.

235. Jaffe GJ, Caprioli J. Optical coherence tomography to detect and manage retinal disease and glaucoma. *Am J Ophthalmol.* 2004;137:156-169.

236. Medeiros FA, Vizzeri G, Zangwill LM, et al. Comparison of retinal nerve fiber layer and optic disc imaging for diagnosing glaucoma in patients suspected of having the disease. *Ophthalmology.* 2008;115:1340-1346.

237. Morgan JE, Waldock A. Scanning laser polarimetry of the normal human retinal nerve fiber layer: a quantitative analysis. *Am J Ophthalmol.* 2000;129:76-82.

238. Strouthidis NG, Fortune B, Yang H, et al. Longitudinal change detected by spectral domain optical coherence tomography in the optic nerve head and peripapillary retina in experimental glaucoma. *Invest Ophthalmol Vis Sci.* 2011;52:1206-1219.

239. Wang X, Li S, Fu J, et al. Comparative study of retinal nerve fibre layer measurement by RTVue OCT and GDx VCC. *Br J Ophthalmol.* 2011;95:509-513.

240. Fortune B, Reynaud J, Wang L, et al. Does optic nerve head surface topography change prior to loss of retinal nerve fiber layer thickness: a test of the site of injury hypothesis in experimental glaucoma. *PloS one.* 2013;8:e77831.

241. Xu G, Weinreb RN, Leung CK. Optic Nerve Head Deformation in Glaucoma: The Temporal Relationship between Optic Nerve Head Surface Depression and Retinal Nerve Fiber Layer Thinning. *Ophthalmology.* 2014.

242. Arvanitaki V, Tsilimbaris MK, Pallikaris A, et al. Macular retinal and nerve fiber layer thickness in early glaucoma: clinical correlations. *Middle East African journal of ophthalmology.* 2012;19:204-210.

243. Desatnik H, Quigley HA, Glovinsky Y. Study of central retinal ganglion cell loss in experimental glaucoma in monkey eyes. *J Glaucoma.* 1996;5:46-53.

244. Nakatani Y, Higashide T, Ohkubo S, et al. Evaluation of macular thickness and peripapillary retinal nerve fiber layer thickness for detection of early glaucoma using spectral domain optical coherence tomography. *J Glaucoma.* 2011;20:252-259.

245. Schuman JS, Pedut-Kloizman T, Hertzmark E, et al. Reproducibility of nerve fiber layer thickness measurements using optical coherence tomography. *Ophthalmology.* 1996;103:1889-1898.

246. Lozano DC, Twa MD. Development of a rat schematic eye from in vivo biometry and the correction of lateral magnification in SD-OCT imaging. *Invest Ophthalmol Vis Sci.* 2013;54:6446-6455.

247. Jia L, Cepurna WO, Johnson EC, et al. Patterns of intraocular pressure elevation after aqueous humor outflow obstruction in rats. *Invest Ophthalmol Vis Sci.* 2000;41:1380-1385.

248. Nadal-Nicolas FM, Jimenez-Lopez M, Salinas-Navarro M, et al. Whole number, distribution and co-expression of brn3 transcription factors in retinal ganglion cells of adult albino and pigmented rats. *PloS one.* 2012;7:e49830.

249. Nadal-Nicolas FM, Jimenez-Lopez M, Sobrado-Calvo P, et al. Brn3a as a marker of retinal ganglion cells: qualitative and quantitative time course studies in naive and optic nerve-injured retinas. *Invest Ophthalmol Vis Sci.* 2009;50:3860-3868.

250. WoldeMussie E, Ruiz G, Wijono M, et al. Neuroprotection of retinal ganglion cells by brimonidine in rats with laser-induced chronic ocular hypertension. *Invest Ophthalmol Vis Sci.* 2001;42:2849-2855.

251. Patel NB, Lim M, Gajjar A, et al. Age-associated changes in the retinal nerve fiber layer and optic nerve head. *Invest Ophthalmol Vis Sci.* 2014;55:5134-5143.